ABSTRACT

Title of Document:	ISOTOPE EFFECTS IN THE STATE-RESOLVED COLLISION DYNAMICS OF HIGHLY EXCITED MOLECULES.
	Geraldine Onyinyechi Echebiri, Doctor of Philosophy, 2014
Directed By:	Professor Amy S. Mullin, Department of Chemistry and Biochemistry

The importance of highly excited molecules in the fields of combustion and atmospheric chemistry makes it essential to study pathways by which energy is lost from the excited molecule. One such pathway is by inelastic collisions with a bath molecule. In this dissertation, the collisional relaxation of highly excited pyrazine-h_4 (E_{vib} = 37900 cm^{-1}) and pyrazine-d_4 (E_{vib} = 37900 cm^{-1}) with HCl (300 K) is studied. The outcomes of the inelastic collision studies reveal quantum state-energy gaps of molecules and their intermolecular interactions affect the mechanism and dynamics of collisional energy transfer.

The results from collisional relaxation of pyrazine-h_4 (E_{vib} = 37900 cm^{-1}) with HCl were compared to those from collisional relaxation of pyrazine-h_4 (E_{vib}) with DCl in order to deduce the effects of quantum state-energy gaps on the dynamics of collisional energy transfer. The comparison shows the dynamics for collisional

deactivation of pyrazine-h_4 (E_{vib}) with HCl and DCl are different, and are possibly due to their intermolecular interactions with pyrazine-h_4 (E_{vib}).

The data for collisional relaxation of pyrazine-d_4 (E_{vib} = 37900 cm^{-1}) with HCl were compared to those for pyrazine-h_4 (E_{vib}) + HCl collisions in order to determine the contributions of near-resonant vibrational energies of the collision partners on the collision dynamics. The comparison shows the energy transfer dynamics for collisional quenching of pyrazine-h_4 (E_{vib}) and pyrazine-d_4 (E_{vib}) with HCl are similar. The similarity in their energy transfer dynamics suggests near-resonance effects are not contributing significantly to the collision dynamics.

ISOTOPE EFFECTS IN THE STATE-RESOLVED COLLISION DYNAMICS OF HIGHLY EXCITED MOLECULES.

By

Geraldine Onyinyechi Echebiri.

Dissertation submitted to the Faculty of the Graduate School of the
University of Maryland, College Park, in partial fulfillment
of the requirements for the degree of
Doctor of Philosophy
2014

Advisory Committee:
Professor Amy S. Mullin, Chair
Professor Daniel Falvey
Professor Janice Reutt-Robey
Professor YuHuang Wang
Professor Christopher Monroe

Acknowledgements

I will like to thank Professor Amy S. Mullin for giving me the opportunity, tools and guidance needed to complete the research projects in this dissertation. I am grateful to Matthew Smarte, Wendell W. Walters, Jill Cleveland, Christine McCarl, Alice Kunin, Carlos Toro, Grace Benson, Chris Bognar and Matthew Murray for their assistance with the projects covered in this dissertation. I also want to thank my family and friends for their encouragement and support throughout these research studies. The research projects presented in this dissertation were funded by the Department of Energy Basic Energy Sciences (DOE BES) and I am grateful for their support.

Table of Contents

Chapter 1: Introduction

1.1 Importance of Collisional Energy Transfer

The research projects presented in this dissertation are motivated by the goal to develop a microscopic understanding of molecular energy transfer and the means by which quantum state-energy gaps in molecules affect the dynamics of collisional relaxation of highly excited molecules. Studying collisional quenching of highly excited molecules in the gas phase is important since it directly competes with their unimolecular reactions [1, 2]. Knowing how inelastic collisions of high energy molecules impact unimolecular reactions is crucial to identifying molecular factors that affect collisional energy transfer in combustion and atmospheric processes [1, 2].

The Lindemann-Hinshelwood model describes the competition between collisional deactivation and unimolecular reaction [1, 3, 4]. In this model, molecule A undergoes collisions with molecule B and gains enough energy to dissociate, as shown in Eq. 1.1.

$$A + B \rightarrow A^* + B \qquad \text{(Eq. 1.1)}$$

The highly excited molecule A* can decompose to form product C or it can lose its internal energy through collisions with B, as described by Eq. 1.2.

$$A^* \rightarrow C$$
$$\text{or} \qquad \text{(Eq. 1.2)}$$
$$A^* + B \rightarrow A + B$$

Dissociation lifetimes of A* generally increase with increasing complexity of the molecule. Polyatomic molecules with more internal degrees of freedom have more

phase space to hold the internal energy and it generally takes longer for the energy to find its way into the dissociative modes. Longer lifetimes of A* correspond to a greater probability of collisional deactivation. In the experiments presented in this dissertation, the collisional relaxation of highly excited molecules is investigated under conditions where the lifetime of A* is approximately 2 orders of magnitude longer than the measurement time for collisional energy transfer.

The collisional relaxation studies presented in Chapter 3 of this dissertation test for the effect of quantum state density of the energy acceptor on the collision dynamics. Previous studies on the collisional relaxation of pyrazine-h_4 (E_{vib}) with DCl [5] and CO_2 [6] show that CO_2 molecules are scattered in the collisions with larger changes in its rotational and translational energies compared to DCl. The smaller rotational constant for CO_2 ($B = 0.39\ cm^{-1}$) compared to DCl ($B = 5.4\ cm^{-1}$) could have contributed to the larger energy changes seen for scattered CO_2. Comparing the results for DCl to the outcome of collisional quenching of pyrazine-h_4 (E_{vib}) with HCl will reveal the effects of quantum state-energy gaps on collisional energy transfer. With this goal in mind, collisional relaxation studies of pyrazine-h_4 (E_{vib}) with HCl were carried out and the results are compared to DCl scattering.

Two general pathways exist for vibrational energy transfer from high energy molecules [1, 2, 7]. In one mechanism, the vibrational energy transferred from the energy donor goes into the vibrational degree(s) of freedom of the energy acceptor. This pathway is referred to in this thesis as vibration-to-vibration ($V \rightarrow V$) energy transfer. In the other mechanism, vibrational energy of the donor goes into the rotational and translational degrees of freedom in the acceptor molecule. This

pathway is referred to here as vibration-rotation and translation (V→RT) energy transfer. A number of inelastic collision studies have shown the probability for V→V energy transfer increased as the vibrational frequencies of the collision partners come into resonance [8, 9]. Near-resonance of the vibrational transitions of the collision partners is important for V→V energy transfer since the energy accepting molecules have quantized energy gaps and therefore, can only accept a specific amount of energy.

The quantum constraints for V→V energy transfer limit its probability relative to that for V→RT energy transfer [10, 11], where the strong coupling of the rotational and translational motions is likely to satisfy the quantum restrictions of molecular energy. Self-relaxation collisions of highly excited molecules are reported to be dominated by V→V energy transfer [12, 13]. The predominance of the V→V channel in such self-quenching stems from the frequency and energy gap matching in the donor and acceptor molecules.

The mechanism for energy transfer is affected by intermolecular interactions of the molecules [2, 14, 15]. Collisions wherein molecules exchange energy at long intermolecular distances are likely to result in V→V energy transfer since they are mediated by long range attractive forces. On the other hand, collisional energy transfer that takes place at short intermolecular distances are likely to be dominated by V→RT energy transfer since this type of energy transfer is mediated by repulsive interactions between the collision partners. The extent to which collisional energy transfer mechanism is affected by intermolecular forces and near-resonance effects is

addressed in this dissertation through collisional relaxation studies of pyrazine-h_4 (E_{vib}) and pyrazine-h_4 (E_{vib}) with HCl.

1.2 Probing techniques for collisional quenching studies

High resolution transient IR absorption spectroscopy is used for the experiments in this dissertation in order to investigate the dynamics of collisional energy transfer. This approach focuses on the quantum state-resolved outcome of collisions by measuring energy gain in energy-accepting bath molecules. The energy transfer pathways are characterized in terms of the vibrational, rotational and translational energies of the product molecules. The detailed information provided by these studies complement other experimental approaches that measure energy loss from highly excited molecules. Among these methods are time-resolved UV absorption [16, 17], IR fluorescence [18-20] and kinetically controlled selective ionization [21, 22].

High-resolution transient mid-IR absorption spectroscopy is a powerful technique for studying the dynamics of collisional energy transfer [2, 23-30]. The ideal IR light for such measurements is stable, high-resolution, broadly tunable and sufficiently powerful to access molecular transitions that have a broad range of oscillator strengths. Transient IR absorption yields detailed quantum state-resolved information for nascent species, thereby revealing the microscopic mechanisms for the collisional energy transfer.

In the recent past, lead-salt diode lasers and color-center lasers have been the IR sources of choice for high-resolution transient IR absorption spectroscopy because they meet many of the requirements for transient detection.[2, 23-29, 31, 32]. These

light sources provide high-resolution output (<10 MHz) that is often narrow enough for measuring Doppler-broadened line profiles for individual ro-vibrational transitions, their output wavelengths are tunable to individual molecular transitions, and they are amenable to active feedback stabilization schemes to control the output frequency. However, diode lasers and color-center lasers have a number of disadvantages that impact their effectiveness.

Lead-salt diode lasers have relatively low output powers (~ 200 μW or less), have reduced performance at wavelengths shorter than $\lambda = 4$ μm and are tunable over limited ranges (~ 200 cm^{-1} or less) with non-continuous tuning. Color-center lasers have larger output powers (~5 mW) and more continuous tuning capability, but require complex optical set-ups for single-mode tuning and it has become difficult lately to obtain functioning crystals. Recent developments in IR light sources such as continuous-wave (CW) mid-IR optical parametric oscillators (OPOs) are providing new opportunities for precise and sensitive measurements of transient molecular processes [30]. As part of this thesis work, an OPO-based high-resolution transient IR absorption spectroscopy was constructed in order to investigate collisional energy transfer.

Continuous-wave mid-IR OPOs based on quasi-phase-matching of nonlinear crystals are especially useful for molecular spectroscopy based on their high spectral resolution (~ 1 MHz), broad tunability [33, 34], and stable, high-power output (>1 W). The use of OPOs as a source of IR light has existed for some time, but recent advances in the development of quasi-phase-matched crystals such as periodically-poled lithium niobate (PPLN) crystals and high pump power sources such as fiber

lasers [35-37] have led to commercially available OPO devices. A number of other groups have taken advantage of these features of mid-IR OPOs for studies in the areas of frequency combs [38], laser-cooled atoms [39] and gas-surface chemistry [40].

1.2 Molecules used for collisional energy transfer studies

The molecules used for the inelastic collision studies presented in this dissertation are hydrogen chloride (HCl), pyrazine-h_4 ($C_4H_4N_2$) and pyrazine-d_4 ($C_4D_4N_2$). The structures of all three molecules are shown in Figure 1.1. HCl is used

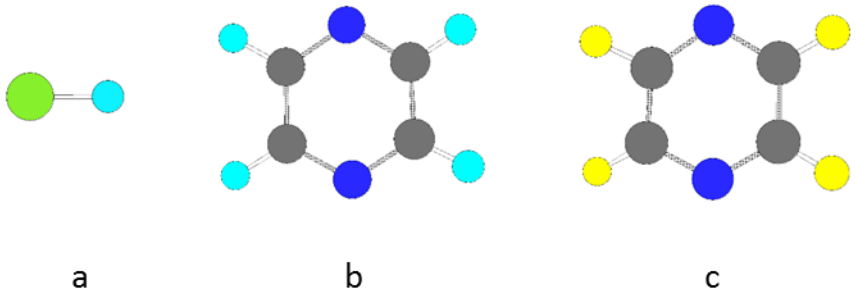

Figure 1.1. Structures of a) HCl, b) pyrazine-h_4 and c) pyrazine-d_4 molecules

as the energy acceptor while pyrazine-h_4 and pyrazine-d_4 are used as energy donors. The individual *J* states of HCl are probed in these studies. Using HCl makes it easier to probe the quantum states of the bath molecule since its ro-vibrational spectrum is less dense than that of a triatomic or polyatomic [7]. Also, the effects of attractive intermolecular interactions on collisional relaxation dynamics of highly excited molecules are deduced by using a polar molecule such as HCl as the energy acceptor.

Large molecules such as pyrazine-h_4 and pyrazine-d_4 are used as energy donors [5, 6, 14, 41-45] because they can be excited to high vibrational levels, yet remain undissociated in the time scale of the collisional energy transfer measurements [1, 46]. The clean photophysics of highly excited pyrazine-h_4 and pyrazine-d_4

molecules make them favorable for use as energy donors. UV absorption by the mentioned isotopes excites them to high vibrational levels with close to unity quantum yield [47] and the radiationless decay physics is well characterized.

1.3 Dissertation overview

The Chapters of this dissertation present quantum state-resolved data for the collisional relaxation of highly excited pyrazine-h_4 and pyrazine-d_4 molecules with HCl molecules. The experiments were performed with an OPO-based high-resolution transient IR absorption spectrometer. Chapter 2 describes the components of the high-resolution transient IR absorption spectrometer. The performance of the new spectrometer is characterized by comparing with measurements using a lead salt diode laser.

The dynamics for the V→RT pathway of highly excited pyrazine-h_4 (E_{vib} = 37900 cm^{-1}) and HCl are presented in Chapter 3. The study is motivated primarily by interest in knowing the influence of rotational state density of the energy acceptor on collision dynamics. In Chapter 4, the vibration-to-vibration (V→V) energy transfer collisions of pyrazine-h_4 (E_{vib} = 37900 cm^{-1}) and HCl are discussed. This study is motivated by the isotope effects seen in the studies described in Chapter 3. The vibrational frequencies of HCl (ν_{HCl} = 2886 cm^{-1}) [48] and pyrazine (ν_{7b} = 3041 cm^{-1}) [49] are close and previous studies have shown that in some cases V→V energy transfer is enhanced when the vibrational transitions of the collision partners are close in energy [7, 8].

In Chapter 5, further tests of near-resonance effects on collisions dynamics are carried out by studying collisions of pyrazine-d_4 (E_{vib} = 37900 cm^{-1}) with HCl. Any

near-resonance effects of the vibrational motions of the collision partners on the dynamics will be revealed by comparing the results for HCl + pyrazine-d_4 (E_{vib}) collisions to those for HCl + pyrazine-d_4 (E_{vib}) collisions. Lastly, the conclusions reached for each project in this dissertation are presented in Chapter 6 along with future directions for the projects. Following Chapter 6 is the Appendix, where the calculations used in data analysis are discussed.

Chapter 2: Experimental Methods

2.1 An OPO-based Transient IR Absorption Spectrometer

The scheme for measuring collisional energy transfer with high-resolution transient IR absorption spectroscopy in the gas phase involves three steps. In the first step, the energy-donors, in this case pyrazine molecules, are excited with pulsed λ = 266 nm light. Radiationless decay converts the photon energy into vibrational energy of the donor molecules [50]. The second step involves excited donor molecules colliding under low pressure conditions with the energy-acceptors, in this case HCl molecules; the collisions induce population changes in individual rotational states of HCl identified by the quantum number J. The time between collisions is much longer than the instrument response time so that nascent populations are measured at early times following optical excitation of donors. In the third step, the population changes in individual J-states of scattered HCl molecules are measured by transient IR absorption at μ = 3.4 μm using R-branch transitions (ΔJ = 1) of the vibrational fundamental (Δv = 1).

Two types of measurements are made with transient IR absorption. In the first, time-resolved Doppler-broadened line shapes are measured by locking the IR light to a fringe of a scanning Fabry-Perot etalon and collecting transient signal stepwise at a series of IR wavelengths over the line shape. Translational energy distributions are determined from the Doppler-broadened line widths. In the second type of measurement, population changes at line center ν_0 of an HCl IR transition are monitored by locking the IR light to the peak of the absorption line and collecting

transient absorption at a single IR wavelength. Population distributions and rate constants are determined by combining line-center and line width measurements for a number of rotational states.

A lead salt diode laser was initially used to probe the scattered HCl molecules, but the transient IR signals collected have low signal-to-noise ratios (SNRs). The nascent Doppler-broadened line profile measurements made with the diode laser have wavelength-dependent noise, and it was difficult to detect small changes in population in the wings of low-*J* line profiles for scattered HCl. These limitations are seen in the transient IR data collected with the diode laser because it does not operate optimally at wavelengths where HCl absorption lines are located (λ = 3.4 μm).

The measurement difficulties experienced with the diode laser necessitated using a different IR source such as a mid-IR OPO to probe scattered HCl molecules in the inelastic collisions. The integration of a mid-IR OPO into a high-resolution transient IR absorption spectrometer is discussed in this Chapter. Samples of transient IR measurements made with the OPO are presented and are compared to those collected with the diode laser to show improvements in the quality of data collected with the OPO.

2.1.1 Continuous-Wave (CW) mid-IR OPO

Optical parametric oscillators (OPOs) consists of nonlinear crystals that convert a single photon of the pump light into two other photons of lower energy known as signal and idler. The use of OPOs as a source of IR light has existed for some time, but recent advances in the development of quasi-phase-matched crystals such as periodically-poled lithium niobate (PPLN) crystals and high pump power

sources such as fiber lasers [51, 52] have led to commercially available devices that provide high resolution (~1 MHz) and high power (>1W) IR light with wide spectral coverage [34, 53]. The state-resolved outcome of molecular collisions that are presented in this dissertation were carried out using a mid-IR OPO.

The OPO used in the studies that are reported in this thesis is the Aculight Argos, module C. Its PPLN crystal is doped with magnesium oxide (MgO). The crystal is pumped using 1064 nm light from a Ytterbium-doped fiber laser and amplifier (IPG Photonics). The pump beam is split by the OPO to generate signal ($\lambda \approx$ 1.46 to 1.60 μm) and idler ($\lambda \approx$ 3.2 to 3.9 μm) beams. The output of the OPO is linearly polarized. The IR probe transitions of interest for HCl involve excitation of one vibrational quantum ($\Delta v = 1$) and one rotational angular momentum quantum ($\Delta J = +1$) at wavelengths between $\lambda = 3.2$ to 3.4 μm. For this wavelength region, we use the OPO idler beam.

2.1.2 Pump Laser

The source of UV light that pumps the energy-donor molecules is a neodymium-doped (Nd) yttrium aluminum garnet (YAG) laser. The Nd:YAG rod is pumped by high power flashlamps to generate 1064 nm light with an energy of ~500 mJ/pulse. Lasing action is achieved in the Nd:YAG laser system (Powerlite 8000 Series) by Q-switching the laser after firing the flashlamps. Q-switching enables multiple oscillations of the fundamental output wavelength of the Nd:YAG rod in the laser cavity. The 1064 nm light emitted by the Nd:YAG crystal is sent through a second harmonic generation (SHG) crystal to give 532 nm light with an energy of ~300 mJ/pulse. The 532 nm light is subsequently sent through a fourth harmonic

generation (FHG) crystal to give 266 nm light with energy of ~40 mJ/pulse. The Nd:YAG laser is operated at a frequency of 10 Hz and has a 5 ns pulse width.

2.1.3 Integration of Probe and Pump Laser into Spectrometer

The high-resolution transient IR absorption spectrometer utilized for the energy transfer studies is described here [30]. Using a CW mid-IR OPO for high-resolution transient IR absorption spectroscopy entails setting up active feedback to control the output wavelength and synchronizing that control with the pulse that initiates the transient event, in our case a UV laser pulse. An overview of the feedback scheme is shown in Figure 2.1. To achieve precise wavelength control, the IR optical frequency is dithered by modulating the wavelength of the fiber laser that pumps the OPO. The modulated IR light passes through a reference gas cell or a tunable Fabry-Perot etalon and is collected with phase-sensitive detection. An error signal from a lock-in amplifier is fed back into the pump laser to lock the IR frequency to the peak of a molecular transition or an etalon fringe. The frequency and phase of the IR modulation are synchronized to the firing of the pulsed laser so that transient absorption is measured at a well-defined IR frequency within the modulation cycle.

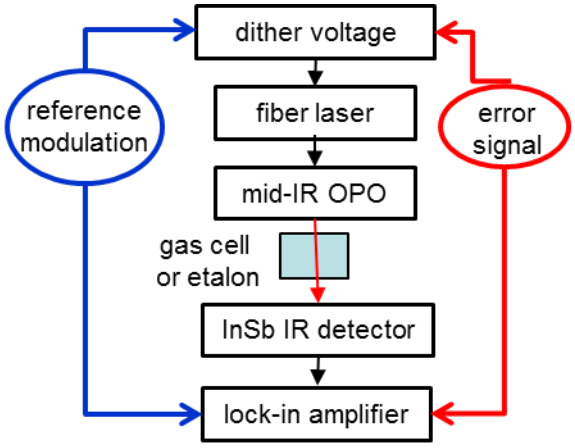

Figure 2.1. Overview of OPO control

The frequency-stabilized OPO output is used in a transient IR absorption spectrometer as shown in Figure 2.2. The OPO frequency modulation is realized by applying a dither voltage to a piezoelectric transducer (PZT) in the pump laser. Depending on the type of measurement, the range of OPO frequencies covered in a single modulation cycle is selected to scan over either the peak of a single fringe of a scanning Fabry-Perot etalon (FSR = 0.01 cm^{-1}) or the peak of a molecular transition of interest. The modulated reference beam is collected with an InSb detector, the output of which goes into a lock-in amplifier (Stanford Research Systems). The error signal from the lock-in amplifier is added to the dither voltage for the pump laser PZT. The error signal continuously adjusts the idler-wavelength to maintain a lock on the etalon fringe or a molecular absorption line, thus completing the feedback loop and stabilizing the OPO output frequency. For line profile measurements, the scanning etalon fringe is tuned in steps by computer-controlled rotation of a CaF_2 plate in the etalon using a digital-to-analog converter.

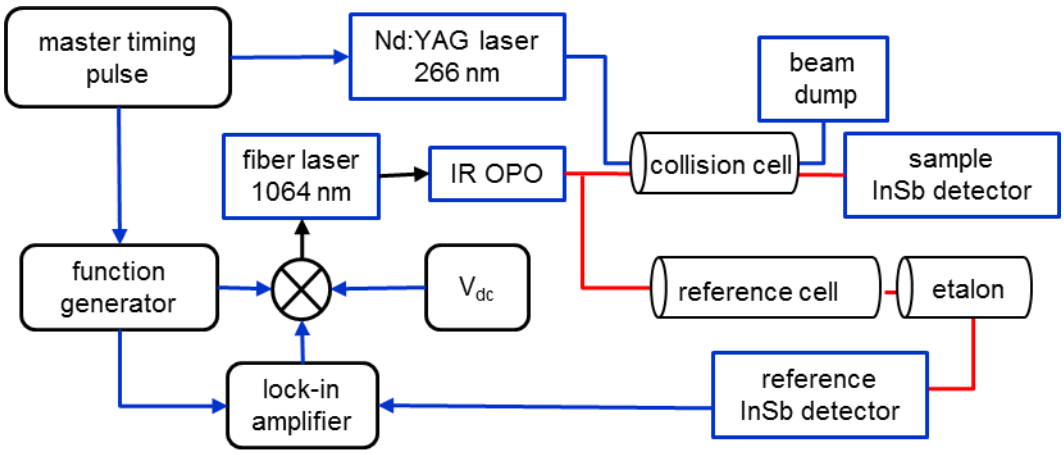

Figure 2.2. Schematic diagram of OPO-based transient absorption spectrometer

The IR sample beam passes through a 3-m cell containing a low pressure 1:1 mixture of pyrazine-h_4 and HCl vapor. The transmitted intensity passes through a monochromator (Laser Photonics) and is collected on a second InSb detector (Judson) with a 300 ns risetime. A digital oscilloscope (LeCroy 9304A) records and averages transient signals from the sample detector following the UV pulse.

For coarse tuning of the OPO idler-wavelength, the crystal position is manually translated and the angle of an intracavity etalon is adjusted to locate the spectral region of interest. The finest tuning of the OPO is achieved by applying a voltage to the fiber laser PZT with a tuning ratio of 95.2 V/cm^{-1}. The pump laser PZT is controlled by the summed output of the modulation voltage from a digital function generator, a tunable DC voltage (0-150 V) (Thorlabs) and the error signal from the lock-in amplifier. The amplitude of the dither voltage is varied depending on the type of scan required. For tuning over multiple absorption lines, voltages up to 20 V are used, corresponding to an IR scan of 0.21 cm^{-1}. For transient measurements of a

single absorption line, the modulation voltage is reduced to 0.200 V for a modulation amplitude of 0.0021 cm^{-1}. The HCl R7 transition at 300 K has a full width half maximum line width of 0.006 cm^{-1}. The PZT of the OPO pump laser can be modulated up to 10 kHz. Higher modulation frequency reduces noise in the transient signals, but limits the effective wavelength tuning range of the PZT. We choose a modulation frequency of 100 Hz which provides adequate signal-to-noise levels for our measurements and simultaneously allows for a broad modulation that is used for identifying spectral features. For comparison, the diode laser measurements were collected using current modulation at 1 kHz. A pulse generator serves as the master clock for the spectrometer that coordinates the firing of the Nd:YAG laser with the IR modulation cycle.

2.2 Improved Quality of Transient IR data collected with OPO

2.2.1 Comparison of transient IR signals collected with OPO and Diode Laser

Transient measurements of pyrazine-h_4/HCl energy transfer were collected on the same spectrometer using two different IR sources: the mid-IR OPO and the lead salt diode laser. Here, we characterize their performance by comparing data measured with the two instruments. Transient signals for HCl (v = 0, *J* = 7) are shown in Figure 2.3a for the OPO and in Figure 2.3b for the diode laser. Both transient signals show similar rates for the appearance of HCl in J = 7 when normalized to UV power and sample pressure. The transients are fit to a flat pre-trigger and an exponential rise for t > 0. The residuals are shown in the lower plots. The root-mean-square (rms) noise (based on the residuals) is a factor of 5 smaller for OPO-based data, corresponding to signal levels with SNRs that are 5 times larger for the

OPO data. At 15 mtorr total pressure, the average time between collisions is 5 μs and data at t = 1 μs corresponds to the single-collision regime. The signals at t = 1 μs have a SNR = 17.5 for the OPO compared to a SNR = 3.5 for the diode laser.

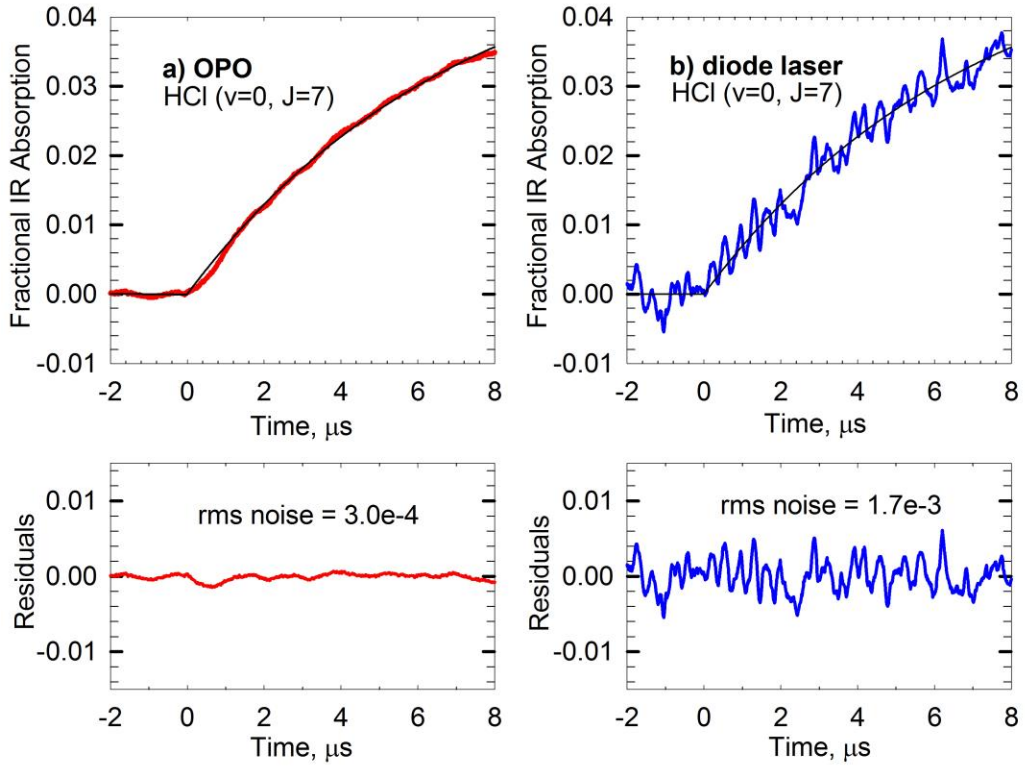

Figure 2.3. Transient absorption and kinetic fitting for the HCl R7 transition following collisions with vibrationally hot pyrazine-h_4 collected with a) the OPO-based spectrometer and b) the diode laser spectrometer. The rms noise is determined from the fitting residuals (shown in lower plots).

The improved SNR for the OPO-based data has direct impact on detection sensitivity for molecules involved in transient events. Based on a minimum SNR = 2 at t = 5 μs or earlier, the OPO-based spectrometer (with a 300 cm path length) can detect as few as 2×10^{9} HCl molecules cm^{-3} per quantum state, compared to 1×10^{10} HCl molecules cm^{-3} per quantum state for the diode-based spectrometer. The

minimum number density that can be detected depends on the IR oscillator strength as well as the spectrometer characteristics. For comparison, the oscillator strength for the strong IR absorption for CO_2 at 2349 cm^{-1} is a factor of 13 larger than that for HCl. Correspondingly, we estimate the CO_2 detection limit for this band is on the order of 1×10^8 molecules cm^{-3} per quantum state for a 300 cm path length [54].

The enhanced detection sensitivity of the OPO-based instrument allows for higher quality measurements of transient line profiles since there is better SNR in the Doppler-broadened wings near baseline. Figure 2.4 shows two Doppler-broadened transient absorption line profiles for HCl (v = 0, J = 7) based on transient absorption at t = 1 μs, one using the OPO (Figure 2.4a) and the other using the diode laser (Figure 2.4b). The fractional absorption intensity at each IR wavelength is determined from a fit of transient signal (as in Figure 2.3) and the wavelength-dependent intensity data are fit with a Gaussian function, with residuals shown in the lower plots. The full width at half maximum line width Δν of the Gaussian fit yields the translational temperature for appearance T_{app} of the scattered molecules. Both measurements result in similar translational temperatures, but the rms residuals are a factor of two smaller for the OPO data. Based on the r^2 values of the Gaussian fits, the line width uncertainty is approximately 10 times less for the OPO data.

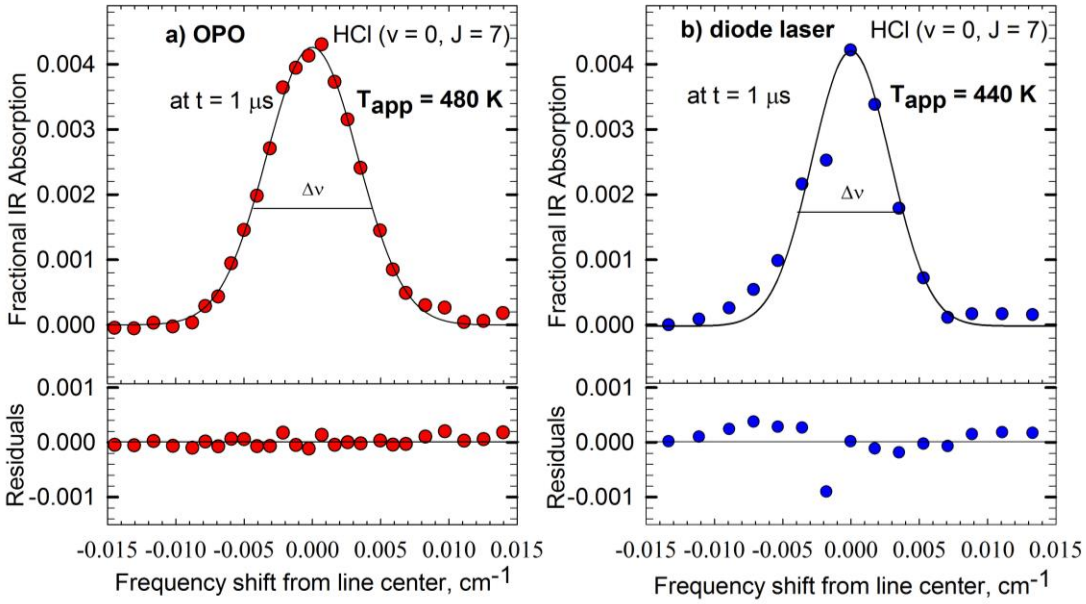

Figure 2.4. Doppler-broadened transient absorption line profiles collected at t = 1 μs for the HCl R7 transition measured with the a) OPO and b) diode laser spectrometers. Each data set is fit with Gaussian function. The OPO data have smaller residuals.

2.2.2 Comparison of Noise in Signals Measured with OPO and Diode Laser

The overall noise in an absorption spectrometer results from noise in the IR source, detectors and electronics.[55] The same liquid-nitrogen cooled detectors and electronics were used for both spectrometers but differences in the IR sources and in their operation affect the overall noise. Here we consider how the overall noise of both spectrometers is affected by IR intensity, IR wavelength and the quality of the frequency lock. For these measurements, the OPO intensity is a factor of 10 greater than for the diode, which reduces shot noise for the OPO. The diode laser is modulated at 1 kHz compared to 100 Hz for the OPO, which reduces the 1/f noise.[56] The spectral resolution of the OPO ($\Delta\nu_{opo}$ <1 MHz or 3×10^{-5} cm^{-1}) is a factor of ten higher than that of the diode laser ($\Delta\nu_{diode}$~10 MHz or 3×10^{-4} cm^{-1}), but

resolution of both light sources is more than sufficient to measure HCl line profiles at 298 K ($\Delta\nu_{298}=6\times10^{-3}$ cm^{-1}).

The power-dependent rms noise for fractional absorption of R7 is shown in Figure 2.5 for two IR wavelengths: at line center and at baseline in the wings of the absorption line profile. With the OPO wavelength tuned to baseline, the rms noise (blue circles) decreases linearly with incident IR intensity. A measurement with the OPO at line center (blue triangle) fits extremely well with the detuned data. The diode laser power was insufficient for an extensive power-dependent measurement but a pair of wavelength-dependent measurements shows several informative results. The rms noise with the diode laser detuned from line center (red circle) is much greater (by a factor of 2.8) than for the detuned OPO and for the diode laser tuned to line center (red triangle), the rms noise increases by an additional factor of 1.9. This result shows that the diode data has additional noise beyond detector noise and that this additional noise source is frequency dependent.

A more detailed comparison of the wavelength-dependent noise for the two spectrometers is reported here, based on transient absorption measurements across the R7 spectral line. The upper plots of Figure 2.6 show the transient noise at two wavelengths for each IR source: Figure 2.6a is at baseline and Figure 2.6b is at line center. In both cases, the rms noise (in brackets) for the diode-based data is larger than for the OPO data. At baseline, the diode-based noise is greater by more than a factor of 5 and at line center, the diode:OPO noise ratio increases to almost 8.

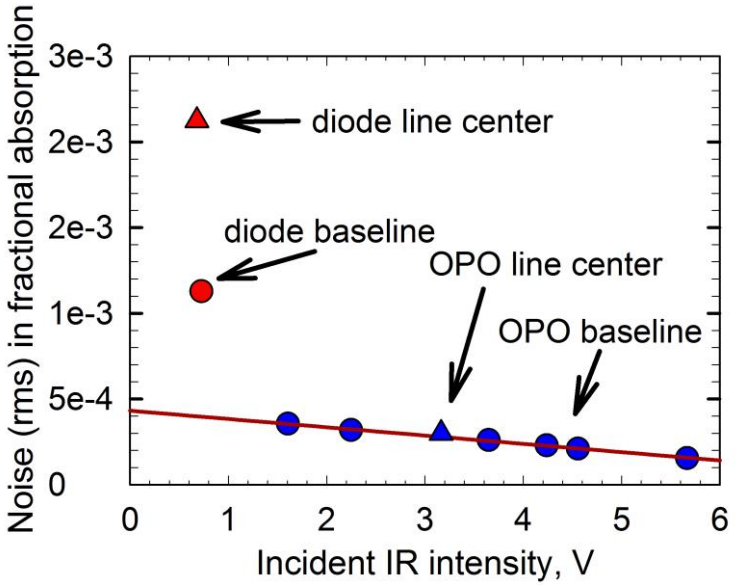

Figure 2.5. IR power dependence of rms noise for transient absorption of HCl R7. Data with the OPO wavelength detuned from transition center (blue circles) have noise that decreases linearly with increasing IR power. A measurement at line center (blue triangle) is consistent with the noise for the detuned light, showing a high degree of wavelength stability. In contrast, the noise for the diode laser is a factor of 3 larger for detuned IR and a factor of 5 larger at line center than for comparable OPO power.

The wavelength dependence of the rms noise across the line shape is shown in Figure 2.6c. The Gaussian fit to the transient line shape (from Figure 2.4) is included as a wavelength reference but its intensity is not to scale. The rms noise for the OPO data is approximately constant over the wavelength range shown, and has an average value of 3.5×10^{-4}. The rms noise for the diode data is larger at all wavelengths: the average rms noise is 1.5×10^{-3} at baseline and as large as of 3.4×10^{-3} at line center. These results indicate that the frequency stabilization of the diode laser is less than ideal, with increased noise occurring near line center caused by excursions away from the central locking frequency. It is likely that the reduced quality of lock arises from intensity fluctuations of the diode laser, as seen in Figure 2.6a.

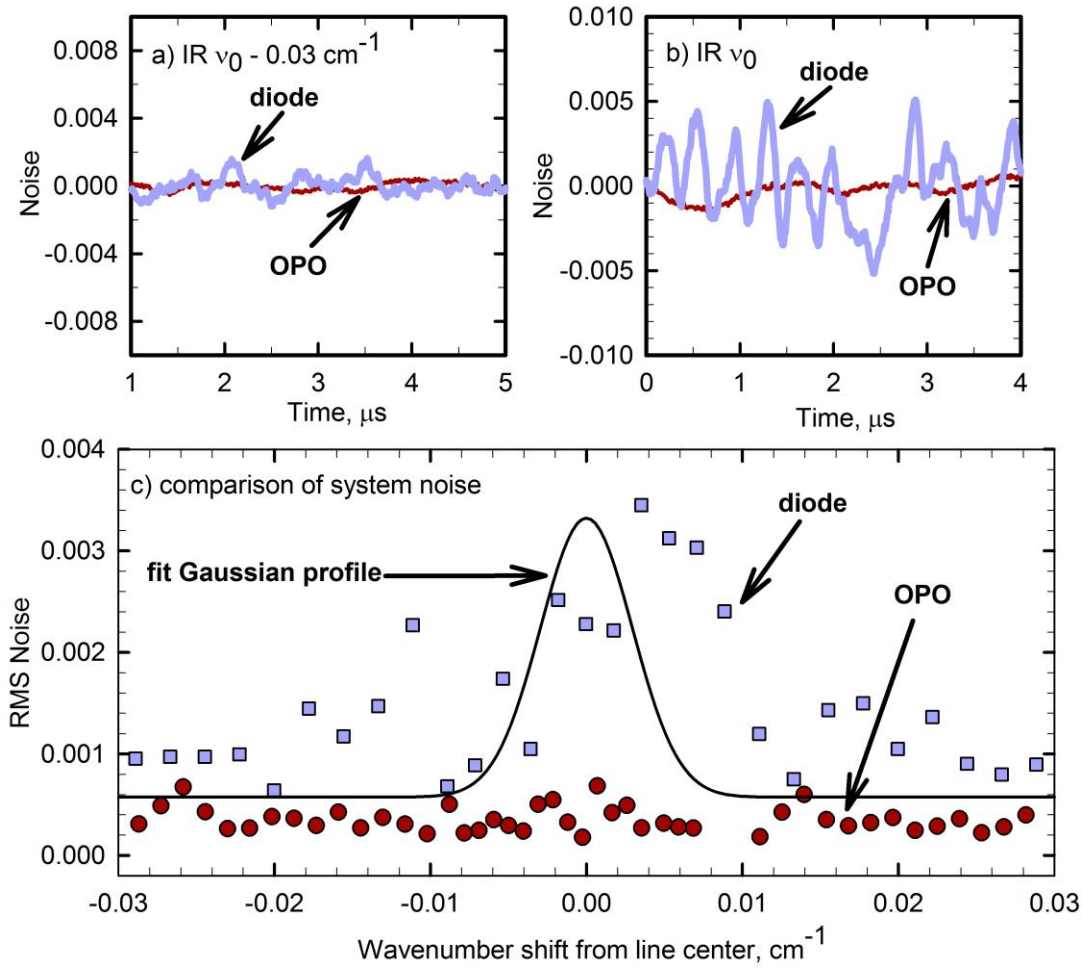

Figure 2.6. Noise collected at a) baseline and b) line center of HCl R7 with the OPO and diode laser. Values for rms noise are listed in parentheses. (c) The wavelength dependence of the rms noise for the R7 line profile measured with the OPO (red circles) and the diode laser (grey squares). The Gaussian profile from Fig. 3 is shown for reference (intensity is not to scale). The noise amplitude for the diode is larger than that of the OPO and shows much more scatter across the line profile.

We have characterized the spectrometer noise for both instruments using fast Fourier transform analysis. The results are consistent with the data in Fig. 5. The power spectra of the transient noise for HCl R7 are shown in Fig. 6. for both IR sources at a) IR baseline and b) line center. The FFT plots show that 1) the noise amplitude for both spectrometers decreases with increasing frequency; 2) at base line

and line center, the diode data has larger amplitude noise than the OPO; 3) the noise amplitude for the OPO data is nearly the same at baseline and line center and 4) the noise for the diode data is larger at line center than at base line.

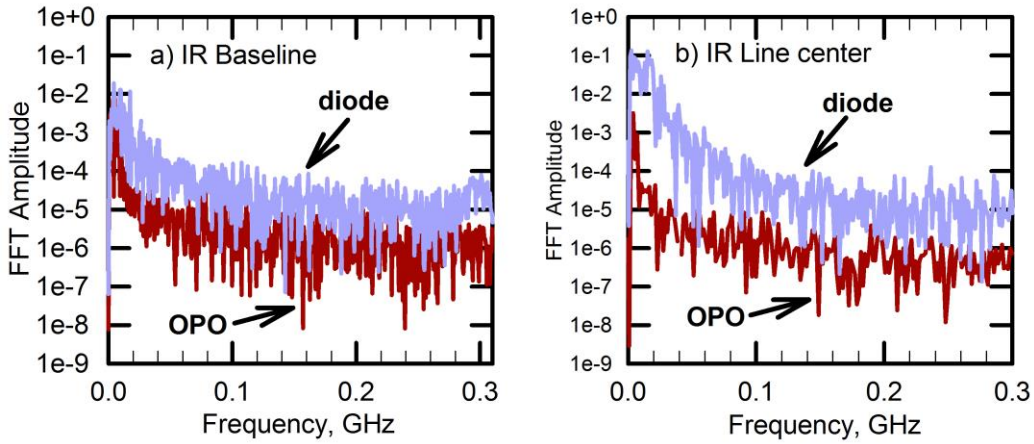

Figure 2.7. The power spectrum of the transient noise collected at a) baseline and b) line center of the HCl R7 transition for the OPO and diode laser spectrometers. The noise amplitude decreases with increasing frequency for both IR sources. The diode-based noise has greater amplitude than the OPO and increases at line center.

2.3 Measurements of double-Gaussian transient IR line profiles

The improved sensitivity and spectral characteristics of the OPO-based spectrometer allow detection of fine details of transient Doppler-broadened line profiles. Double Gaussian structure is present in transient absorption line profiles of low-J rotational states that have initial thermal population. Concurrent energy transfer collisions induce negative-going population depletion at line center and positive-going population appearance in the Doppler-broadened wings of the line profile. Sufficient stability and resolution is required to distinguish these features. Doppler-broadened transient line profiles for the HCl R4 transition (measured at t = 1 μs) are shown in Figure 2.8. The double Gaussian line shape is clearly seen with the

OPO spectrometer (Figure 2.8a), whereas noise obscures that data for diode-based data (Figure 2.8b). The OPO data are fit with an unconstrained double Gaussian, yielding nascent translational temperatures for appearance T_{app} and depletion T_{dep}, along with time-dependent intensities for each Gaussian. Attempts to fit an unconstrained double Gaussian function to the diode-based data were unsuccessful. Instead, the line width fitting results for the OPO-based data are used in a constrained fit for the diode-based data. The result is shown in Figure 2.8b, highlighting the capabilities of the OPO-based spectrometer in measuring details of molecular dynamics.

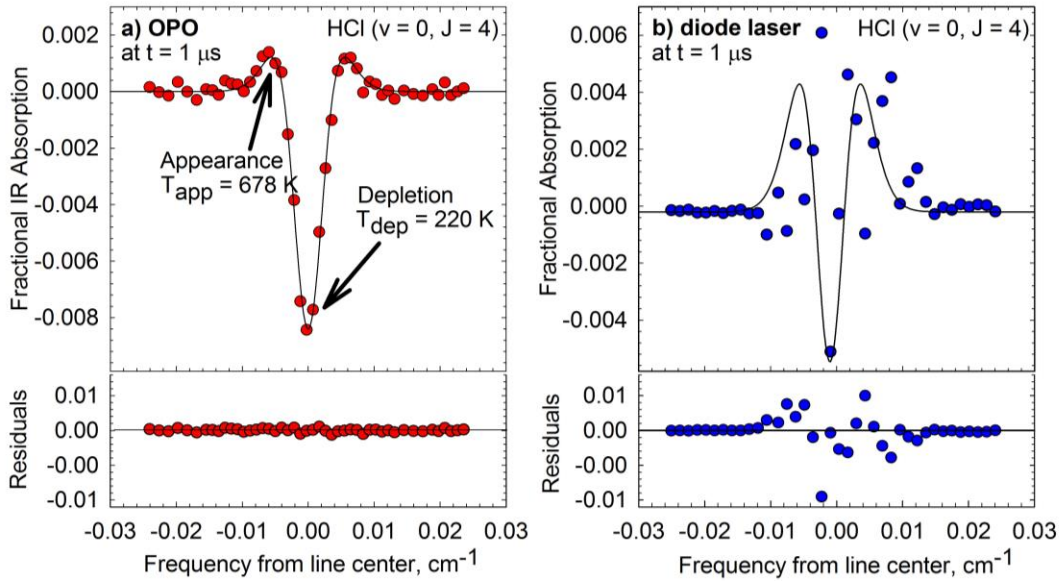

Figure 2.8. Doppler-broadened transient absorption line profiles for the HCl R4 transition collected with the (a) OPO and (b) diode laser spectrometers. The OPO-based instrument has sufficient stability and frequency resolution to reveal the double Gaussian nature of the line profile. These features are obscured by noise in the diode-based instrument.

The enhanced SNR for the OPO-based instrument has important benefits for transient absorption measurements: measurement of smaller population changes,

shorter averaging times and reduced pressure conditions that are beneficial in minimizing secondary collisions that interfere with nascent measurements. These features combine to enable more sensitive and detailed measurements of transient processes in molecules and chemical reactions.

Chapter 3: Quantum State-Resolved Isotope Effects in Collisional Quenching of Highly Excited Pyrazine-h_4 with HCl and DCl

3.1 Introduction

High energy molecules are important species in unimolecular reactions, combustion processes and atmospheric chemistry [1, 3, 57, 58]. Inelastic collisions deactivate energized molecules and compete with chemical reactions [1, 3, 57, 58]. Studies of collisional relaxation of hot molecules give insight into molecular energy flow and the effectiveness of collisional cooling. A number of collisional energy transfer studies have used highly excited pyrazine-h_4 molecules as the energy donor [5, 6, 43, 59-64]. The photophysics and chemical properties of pyrazine-h_4 make it attractive as an energy donor in inelastic scattering experiments. By absorption of a single UV photon, pyrazine-h_4 is prepared in very high vibrational states with a quantum yield of almost unity [47]. Utilization of pyrazine-h_4 molecules in chemical studies enable simultaneous investigations of inelastic and reactive collisions when the photon energy exceeds the dissociation energy [46].

State-resolved inelastic scattering studies shed light on the dependence of the collision dynamics on the energy gap law or angular momentum gap law [65]. An energy gap law favors small energy transfer values in inelastic collisions, which result in smaller changes in the rotational quanta for a hydrogenated energy acceptor compared to the deuterated one. HCl has a smaller moment of inertia than DCl, and hence a larger B constant (B_{HCl} = 10.4 cm^{-1} and B_{DCl} = 5.4 cm^{-1}). The changes in

rotational quanta for HCl are expected to be smaller than that for DCl if the energy transfer is governed by the energy gap law.

An angular momentum gap law favors small changes in rotational quanta of the energy acceptor. Small ΔJ values correspond to larger energy changes for a hydrogenated energy acceptor compared to the deuterated one. Inelastic collisions of excited pyrazine-h_4 are expected to involve larger energy changes ΔE for scattered HCl compared to scattered DCl if their collision dynamics are governed strictly by the angular momentum. In addition, angular momentum changes in impulsive collisions correlate with changes in recoil velocity, so differences in translational energy distributions of scattered molecules will provide additional information about the mechanism. The reality is that both small ΔE and small ΔJ are favored in collisions. By increasing the energy spacing in the acceptor, you are making a sparcer "accepting field." The extent to which the two gap laws are sensitive to the rotational state density will be revealed by measuring the dynamics.

The nature of the intermolecular interactions of the collision partners can affect their inelastic collision dynamics. In the limiting cases, the interactions can be isotropic or anisotropic. In the case of isotropic interactions, there is no favored orientation for the energy donor and acceptor, which allows the acceptor in essence to have equal probability of interacting with all the excited degrees of freedom in the excited donor. In the case of strongly anisotropic interactions, there is a favored orientation for the interaction between the collision partners, which can limit access to the excited degrees of freedom of the energy donor. The results for inelastic

scattering of HCl and DCl will shed light on the nature of their intermolecular interactions with pyrazine-h_4 (E_{vib}).

For pyrazine-h_4 (E_{vib}) + HCl (DCl) collisions, anisotropic interactions can be in form of hydrogen bonding interactions between the collision partners. Theoretical studies have shown that azabenzenes such as pyrazine-h_4 and pyridine can form hydrogen-bonded complexes with hydrides such as HCl [66, 67]. The complex can form through σ-type interaction, where the H of HCl interacts with the lone pair electrons on N of the azabenzene (Figure 3.1a). The complex can also form through π-type interaction, where the H of HCl interacts with the π electron cloud of the azabenzene (Figure 3.1b). Only the σ-type interaction is seen in the complexes formed by HCl although both the σ- and π-type interactions are observed in the

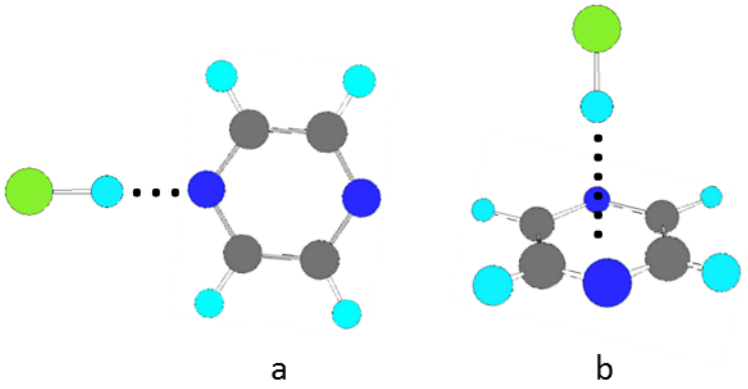

Figure 3.1. Cartoon of the hydrogen-bonded complexes formed by azabenzenes such as pyrazine-h_4 with hydrides such as HCl through a) σ-type interactions and b) π-type interactions. Complexes due to both types of interactions are seen for several hydrides; only the σ-type interaction is seen for HCl complexes.

complexes formed by several hydrides. The stabilizing energy E_{int} for these complexes can be substantial. The interaction energy is E_{int} = 2800 cm^{-1} for the pyridine-HCl complex [67]. Investigations done on hydrogen-bonded molecular

complexes have shown isotope effects in the lifetimes of their vibrational predissociations and electronic excitations [48, 68, 69]. Studies of hydrogen-bonded molecular complexes have revealed isotopic differences in the quantum state distribution of their dissociated products [68, 70] and in their reaction rates [71].

Miller and co-workers reported a decrease in the vibrational predissociation lifetime of C_2H_2-HCl complex compared to that of C_2H_2-DCl complex [48]. They attributed the faster decay time to a near-resonance of the HCl stretch and C-H stretch of acetylene. Syage concluded from the lifetimes of excited phenol-ammonia complexes that proton tunneling enhances the relaxation of the hydrogenated complex compared to the deuterated one [69]. The work of Bernstein and co-workers shows a higher rate for proton transfer in the 1-naphthol-$h_1(NH_3)_3$ complex compared to that of 1-naphthol-$d_1(NH_3)_3$ [71]. This behavior was attributed to a difference in activation barrier based on differences in zero point energy of the isotopes. In the case of strongly inelastic collisions, it is possible that isotope effects may be present due to vibrational resonance, proton tunneling and/or zero point energy differences.

Some collisional relaxation studies have looked at isotope effects in energy acceptors. IR fluorescence studies by Toselli and Barker measured collisional energy transfer from vibrationally excited toluene-d_8 to a number of bath gases such as H_2, D_2, H_2O and D_2O [72]. The average energy transferred is $\langle \Delta E \rangle = 82 \pm 3$ cm^{-1} for H_2 collisions, $\langle \Delta E \rangle = 81 \pm 3$ cm^{-1} for D_2 collisions, $\langle \Delta E \rangle = 387 \pm 14$ cm^{-1} for H_2O collisions and 378 ± 25 cm^{-1} for D_2O collisions. These results suggest the role of the angular momentum gap law since small changes in *J* correspond to larger energy changes in *E* for the hydrogenated energy acceptor.

In the collisional energy transfer studies reported in this Chapter, highly vibrationally excited pyrazine-h_4 molecules (E_{vib} = 37900 cm^{-1}) are collided with HCl molecules at 300 K. The nascent outcome of collisions is probed by transient IR absorption spectroscopy to monitor population changes in individual rotational states *J* of scattered HCl molecules in the ground vibrational state (v = 0). The data from present work are compared to earlier data obtained with DCl as the energy acceptor [5]. The purpose of the current work is to investigate if and how the collision dynamics differ between the HCl and DCl isotopes.

3.2 Experimental Methods

The details of the experimental set-up have been described in Chapter 2. The specifics of the set-up pertaining to this work are presented here. Highly vibrationally excited pyrazine-h_4 molecules in the gas phase are prepared with the fourth harmonic of a pulsed Nd:YAG laser at λ = 266 nm. Pyrazine-h_4 is electronically excited to the S_1 and S_2 states after absorbing a UV photon and then relaxes in ~50 ns into high vibrational states in the ground electronic state (S_0) through nonradiative decay [46, 47]. Pyrazine-h_4 at λ = 266 nm excitation is just above its dissociation threshold, but the lifetime for dissociation is t = 70 μs, which is much longer than the collision data reported here. The vibrational energy of the excited pyrazine molecules is 37900 cm^{-1}. Individual rotational states of HCl (v = 0) with rotational quantum number *J* are probed with high-resolution transient IR absorption spectroscopy after single collisions with pyrazine-h_4 (E_{vib}). The R-branch probe transitions for HCl (v = 0) fall

within the wavelength range $\lambda = 3.2$ to 3.4 μm. The transition frequencies, rotational energies and absorption line strengths S_J are listed in Table 3.1. The IR probe light is the idler output of a continuous-wave (CW) optical parametric oscillator (OPO) (Aculight Argos, module C), which covers the wavelength range $\lambda \approx 3.2$ to 3.9 μm. The spectral resolution of the OPO is $\Delta\nu_{IR}$ <1 MHz (3×10^{-5} cm^{-1}).

TABLE 3.1: IR Probe Transitions for Rotational States of HCl[a]

$H^{35}Cl$ (v = 0, J) + $h\nu$ ($\lambda \sim 3.3$ μm) → $H^{35}Cl$ (v = 1, J + 1)			
J	ν_0 (cm^{-1})[b]	E_{rot} (cm^{-1})[c]	S_J (cm $molecule^{-1}$)[d]
0	2906.2468	0	2.367×10^{-19}
1	2925.8967	20.8782	4.194×10^{-19}
2	2944.9138	62.6219	5.034×10^{-19}
3	2963.2861	125.2057	4.852×10^{-19}
4	2981.0017	208.5917	3.960×10^{-19}
5	2998.0490	312.7294	2.804×10^{-19}
6	3014.4166	437.5556	1.745×10^{-19}
7	3030.0934	582.9947	9.616×10^{-20}
8	3045.0686	748.9588	4.719×10^{-20}
9	3059.3314	935.3474	2.070×10^{-20}
10	3072.8716	1142.0480	8.140×10^{-21}
11	3085.6791	1368.9358	2.876×10^{-21}
12	3097.7442	1615.8741	9.146×10^{-22}
13	3109.0575	1882.7142	2.623×10^{-22}

[a] Values are from the HITRAN database [73]. [b] IR frequency at line center for HCl R-branch transitions. [c] Rotational energy for J state of HCl (v = 0). [d] The absorption line strength for individual rotational states of HCl.

For these experiments, a 1:1 mixture of HCl and pyrazine-h_4 gases is flowed in a 3-m cell with a total pressure of ≤ 20 mTorr. The time between collision is t_{col} ~ 4 μs, which is much longer than the time of the pyrazine-h_4 radiationless decay. Transient IR absorption signals for individual *J* states of HCl are collected after the UV pulse and nascent populations are determined at t = 1 μs. An InSb detector (Judson) with a 300 ns rise time collects the transient IR signals. The transient IR signals are averaged by a digital oscilloscope (LeCroy 9304A) for ~ 60 UV laser pulses. A pulse generator synchronizes the firing of the UV pulse with the IR modulation cycle. *J*-specific population changes at line center ν_0 and nascent Doppler-broadened line profiles of HCl are measured using the active feedback control scheme described in Chapter 2.

3.3 Results and Discussion

The following data are obtained using high-resolution transient IR absorption spectroscopy to probe scattered HCl (v = 0) molecules after single collisions with pyrazine-h_4 (E_{vib}). The measurements are made at t = 1 μs after UV excitation of pyrazine-h_4. The data are quantum state-resolved rotational and translational energy gain profiles for recoiling HCl molecules and the *J*-specific rate constants for appearance and depletion of HCl populations. The data from the HCl studies are compared with the data from previous DCl studies [5] in order to investigate isotope effects in the energy transfer dynamics.

3.3.1 Transient IR Absorption Signals for Scattered HCl (v = 0, *J*) Molecules

Figure 3.2a shows a transient IR absorption signal measured at line center ν_0 for the HCl R5 transition. The negative-going signal at line center represents net depletion of population in this rotational state caused by collisions with pyrazine-h_4 (E_{vib}). Positive-going data in Figure 3.2b shows net appearance of molecules that scatter into the $J = 5$ state when the IR light is tuned to the Doppler-broadened wings of the line profile. These types of signals are observed for HCl rotational states with $J \leq 5$. HCl rotational states with $J \leq 5$ have appreciable population at 300 K and net depletion of molecules is observed at ν_0 because of collisions. The initial thermal population for states with $J \geq 6$ are minimal and these states show only positive-going transient signals corresponding to appearance of population.

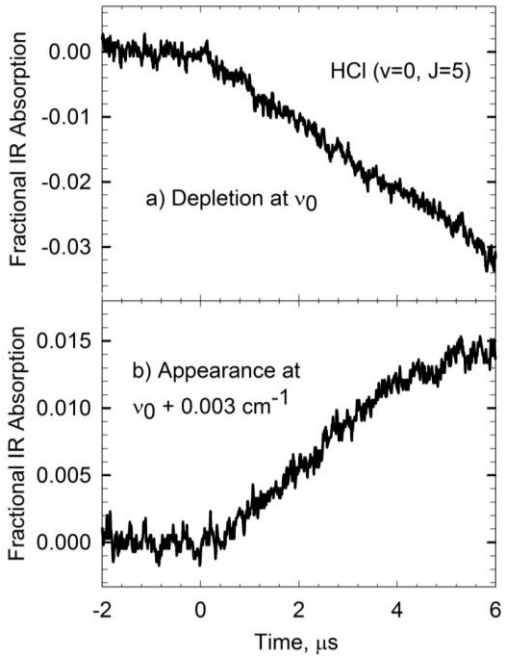

Figure 3.2. Transient IR absorption signals for scattered HCl in (v = 0, $J = 5$) state showing a) depletion of molecules at line center and b) appearance of molecules 0.003 cm^{-1} away from line center.

Figure 3.3 shows the nascent Doppler-broadened absorption line profile measured for HCl (J = 5) at t = 1 μs following the UV pulse. Net depletion is seen at IR frequencies near ν_0 and net appearance is seen in the wings. The data are fit with a double Gaussian function, Eq. 3.1.

$$F(\nu) = F_0 + I_{app} \exp\left(-4\ln 2\left(\frac{\nu-\nu_0}{\Delta\nu_{app}}\right)^2\right) - I_{dep} \exp\left(-4\ln 2\left(\frac{\nu-\nu_0}{\Delta\nu_{dep}}\right)^2\right) \quad \text{(Eq. 3.1)}$$

In Eq. 3.1, F_0 is a small offset, I_{app} and I_{dep} are the IR intensity for appearance and depletion of population at line center respectively, ν is the IR frequency, $\Delta\nu_{app}$ and $\Delta\nu_{dep}$ are the full width at half maximum (FWHM) of the appearance and depletion components of the line width respectively. The fit results are shown as the solid line in Figure 3.3. The residuals of the fit are shown in the lower panel. The double Gaussian function $F(\nu)$ in Eq. 3.1 is a sum of two Gaussian functions that account for the appearance and depletion components of the line profile.

The appearance and depletion profiles from the line profile fit for HCl (J = 5) state are plotted in Figure 3.4. Integration of the area under the appearance (or depletion) curve yields the HCl population that is appearing (or leaving) the J = 5 state as a result of collisions with pyrazine-h_4 (E_{vib}). The nascent FWHM for appearance in J = 5 state is $\Delta\nu_{app}$ = 0.0086 cm^{-1}, corresponding to a lab-frame translational temperature of T_{app} = 580 ± 200 K. The FWHM for depletion of initial population in J = 5 state is $\Delta\nu_{dep}$ = 0.0055 cm^{-1}, corresponding to a lab-frame temperature of T_{dep} = 240 ± 40 K. The observation that T_{app} for appearance is larger

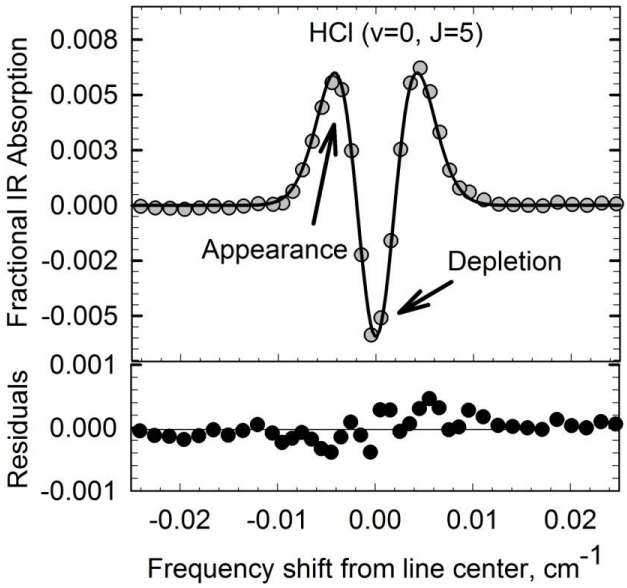

Figure 3.3. Nascent Doppler-broadened line shape (top data points) for recoiling HCl (v = 0) population in $J = 5$ state. The line profile shows net population depletion near ν_0 and net appearance away from line center. The data are fit with a double Gaussian function (solid line) to account for depletion and appearance components. Below the line profile are the residuals of the fit.

than 300 K means that molecules gain translational energy from the inelastic collisions. In contrast, T_{dep} is lower than 300 K, indicating that the slower subset of HCl molecules are the initial collision partners of pyrazine-h_4 (E_{vib}).

Presented in Figure 3.5 are the measured nascent Doppler-broadened line widths for scattered HCl states with $J \leq 5$. The double-Gaussian fits to the line profiles are also included in Figure 3.5. The negative-going signals near line center show depletion of initial population dominates over appearance of scattered population at ν_0 for low-J states. The positive-going signals in the Doppler-broadened wings show net appearance of scattered population dominates over depletion of initial population in the line profile-wings of low-J states.

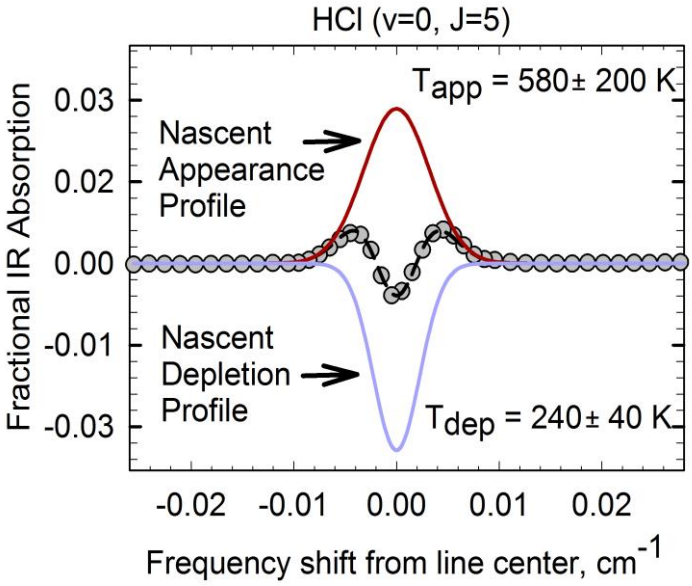

Figure 3.4. The appearance (top curve) and depletion (bottom curve) components of the Doppler-broadened HCl (v = 0, J = 5) line shape. Scattered HCl molecules appear in J = 5 state with high translational temperature while the initial population leave with T <300 K.

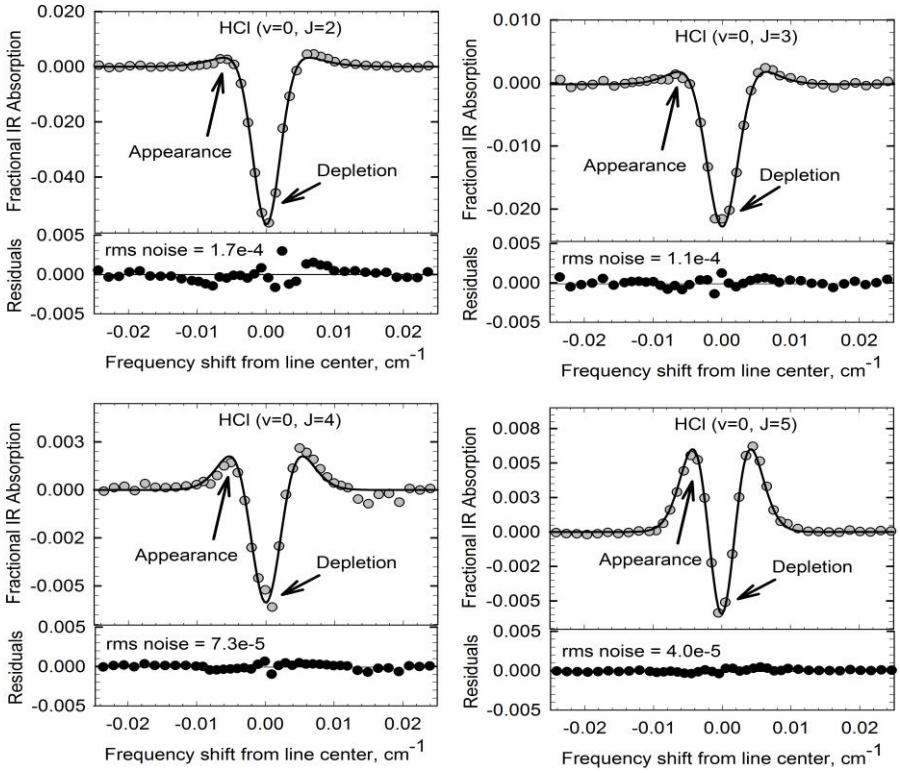

Figure 3.5. Transient Doppler-broadened line profiles for low-J states of HCl. The appearance component of the line profile increases with J state.

The line profiles measurements for scattered HCl in $J \geq 6$ states are presented in Figure 3.6. Scattered HCl states with $J \geq 6$ have transient line profiles that are fit

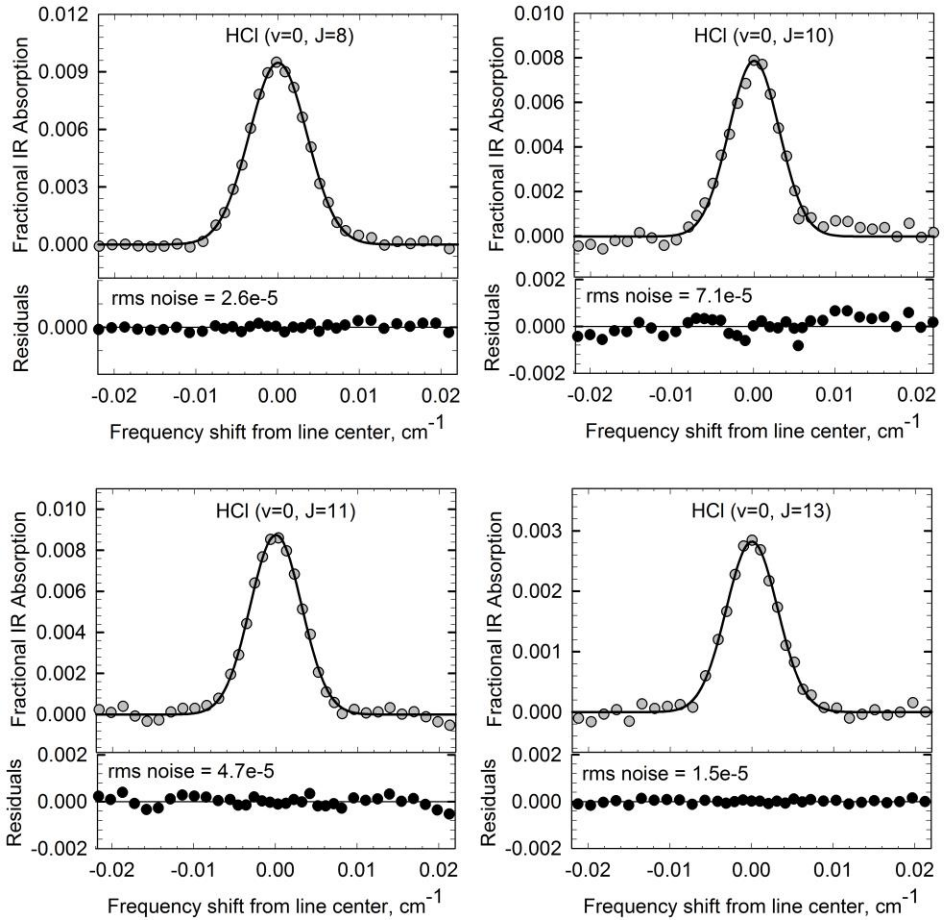

Figure 3.6. The nascent Doppler-broadened line profiles scattered HCl (v = 0) molecules in $J \geq 6$ states. HCl molecules are scattered in these J states with an increase in translational energy

with single Gaussian functions. The data show HCl molecules are scattered in high-J states with net appearance of population. The initial population for the high-J states is small enough to lead to net appearance of scattered population across their line profiles.

3.3.2 Translational Energy Gains of Recoiling HCl

The transient IR absorption Doppler-broadened line profiles for a number of rotational states (J = 2-13) of scattered HCl (v = 0) have been measured at t = 1 μs following UV excitation of pyrazine-h_4. The T_{dep} and T_{app} values from the line profiles are listed in Table 3.2. The depletion temperatures are 200-260 K. The low depletion temperatures (T_{dep} < 300 K) reveal that HCl molecules moving slower than initial average speed are involved in collisions with pyrazine-h_4 (E_{vib}). The appearance temperatures range from T_{app} = 1180 K for J = 2 state to 400 K for J = 13 state. The high T_{app} values show that HCl gains translational energy in collisions with pyrazine-h_4 (E_{vib}). The data in Table 3.2 show that the T_{app} values are inversely correlated with J for the scattered HCl molecules.

Center-of-mass (COM) frame translational temperatures T_{rel} for the collision products are plotted in Figure 3.7. T_{rel} is a measure, in the COM frame, of the translational energy distribution of the two scattered molecules, HCl and pyrazine-h_4 (E_{vib}). The data in Figure 3.7 show that T_{rel} values for collision products decrease exponentially with HCl J values. The quantum state-partitioning of the energy gain by HCl suggests a mechanism that involves collisions of excited pyrazine-h_4 with either the H of HCl or the Cl of HCl as shown in Figure 3.8. Collisions with the light H atom impart torque that leads to low gains in translational energy but high gains in rotational energy. In contrast, collisions with the heavy Cl atom lead to large translational energy gains and small changes in J for HCl.

TABLE 3.2: *J*-specific nascent Doppler-broadened FWHM and translational temperatures of scattered HCl molecules

	depletion of initial HCl (v = 0, *J*)		appearance of scattered HCl (v = 0, *J*)	
J state	$\Delta\nu_{dep}$ (cm^{-1})[a]	T_{dep} (K)[b]	$\Delta\nu_{app}$ (cm^{-1})[a]	T_{app} (K)[b]
2	0.0050	200 ± 40	0.012	1180 ± 350
3	0.0054	240 ± 40	0.011	980 ± 290
4	0.0057	260 ± 40	0.0098	770 ± 230
5	0.0055	240 ± 40	0.0086	580 ± 170
7	-	-	0.0084	550 ± 170
8	-	-	0.0080	490 ± 150
10	-	-	0.0075	420 ± 130
11	-	-	0.0074	410 ± 120
13	-	-	0.0074	400 ± 120

[a] The full width at half maximum (FWHM) for depletion $\Delta\nu_{dep}$ and appearance $\Delta\nu_{app}$ components of a HCl IR line profile. [b] The lab-frame translational temperatures for depletion T_{dep} and appearance T_{app} of HCl molecules. The details of T_{dep} and T_{app} calculations are presented in the Appendix.

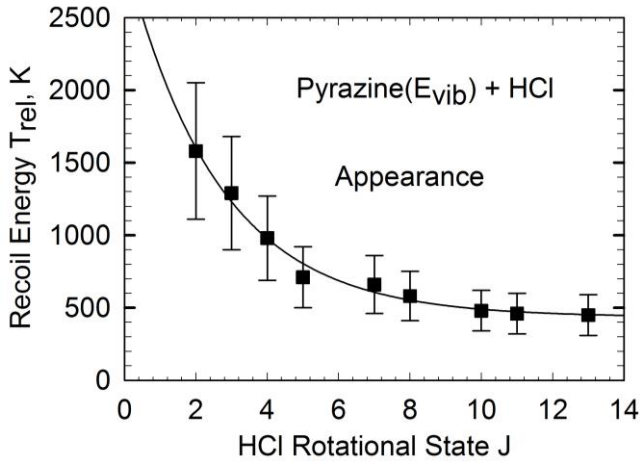

Figure 3.7. Center-of-mass frame translational temperatures T_{rel} (square datapoints) for appearance of scattered HCl population in individual *J* states. The solid line is an exponential fit to the data. An inverse correlation is seen between T_{rel} and *J* states for HCl.

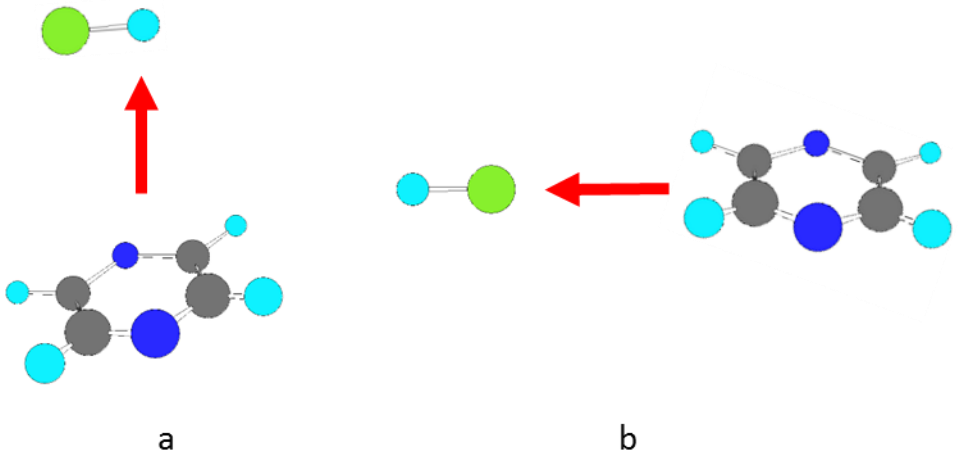

Figure 3.8. Possible mechanism for collisional relaxation of excited pyrazine-h_4 with HCl. The energy transfer data suggest pyrazine-h_4 collides with either a) the H of HCl or b) the Cl of HCl.

A comparison with data on pyrazine-h_4 (E_{vib}) + DCl collisions shows substantial differences. The COM translational energies for HCl and DCl are shown in Figure 3.9. The data for DCl indicates that collisional energy transfer between pyrazine-h_4 (E_{vib}) and DCl occur impulsively and with non-orienting interactions. In pyrazine-h_4 (E_{vib}) + DCl collisions, small gains in rotational and translational energies arise from weak collisions while high gains in rotational and translational energies result from strong collisions. The opposite correlation between T_{rel} and *J* state for the HCl and DCl isotopes highlights differences in interactions of HCl and DCl with excited pyrazine-h_4. The interaction involving HCl appears to preferentially interact with H or Cl of HCl while for DCl this preference is not seen.

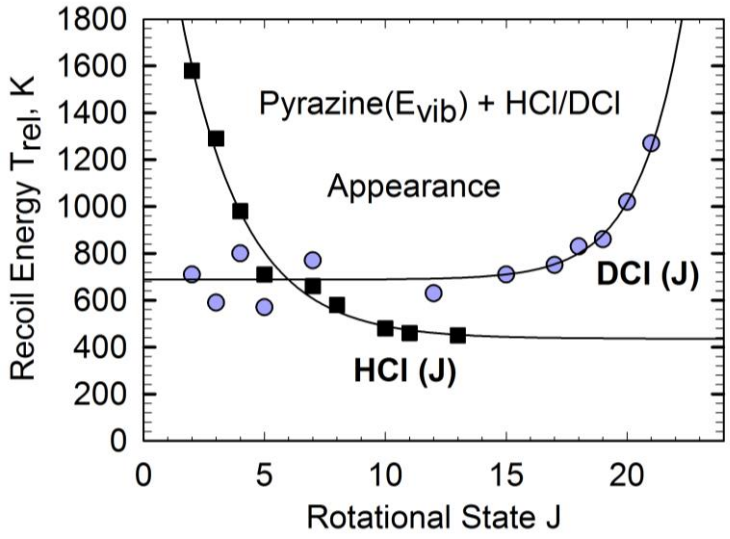

Figure 3.9. T_{rel} for recoiling HCl and DCl molecules in v = 0 state after single collisions with pyrazine-h_4 (E_{vib}). The solid lines are exponential fits to both data. The COM translational temperatures for the isotopes have opposite dependence on rotational quantum number *J*.

3.3.3 Changes in Angular Momentum and Recoil Velocities of Scattered HCl

Angular momentum is conserved in collisions and its conservation requires that the vector sum of the changes in the rotational angular momentum of the bath molecule $\Delta\mathbf{J}_{bath}$, the excited molecule $\Delta\mathbf{J}_{donor}$ and their orbital angular momentum $\Delta\mathbf{L}$ equal zero [74]. Waclawik and co-workers proposed from collisional relaxation of excited benzene that $\Delta\mathbf{J}_{bath}$ and $\Delta\mathbf{J}_{donor}$ must have the same sign to balance out the opposite sign of $\Delta\mathbf{L}$ [75]. This reasonable assumption leads to $\Delta\mathbf{J}_{bath} + \Delta\mathbf{J}_{donor} = \Delta\mathbf{J} = -\Delta\mathbf{L}$. The change in orbital angular momentum is $\Delta\mathbf{L} = \mathbf{b}\mu\Delta\mathbf{v}_{rel}$, where $\mathbf{b}$ is the impact parameter, μ is the reduced mass of HCl and excited pyrazine-h_4 and $\Delta\mathbf{v}_{rel}$ is the change in COM frame velocity. Large values for $\Delta\mathbf{v}_{rel}$ imply large values for $\Delta\mathbf{J}$.

Correlation between changes in the average rotational angular momentum $\langle\Delta\mathbf{J}_{bath}\rangle$ of scattered HCl and COM frame recoil velocity $\Delta\mathbf{v}_{rel}$ are recorded in Table 3.3, and can offer insight into the nature of the collisions. The average absolute changes in rotational angular momenta of scattered HCl are obtained by $\langle\Delta\mathbf{J}_{bath}\rangle = |(\mathbf{J'}_{bath})^2 - \langle\mathbf{J}_{bath}\rangle^2|$ with $\mathbf{J'}_{bath}$ representing the individual final rotational angular momentum of scattered HCl and $\langle\mathbf{J}_{bath}\rangle$ representing its average initial rotational angular momentum. $\langle\mathbf{J}_{bath}\rangle = 3.4$ for HCl at T = 300 K. Table 3.3 shows an inverse correlation between $\Delta\mathbf{J}_{bath}$ and $\Delta\mathbf{v}_{rel}$. The scattered population in the $J = 2$ state have $\Delta\mathbf{J}_{bath} = 2.8$ and $\Delta\mathbf{v}_{rel} = 712$ m/s while those in the $J = 13$ state have $\Delta\mathbf{J}_{bath} = 12.5$ and $\Delta\mathbf{v}_{rel} = 125$ m/s.

TABLE 3.3: Changes in rotational angular momentum and recoil velocities for individual *J* states of scattered HCl (v = 0) molecules

final *J* state	$\langle \Delta \mathbf{J}_{bath} \rangle^a$	$\Delta v_{app}{}^b$	$\langle \mathbf{v}_{lab} \rangle^c$ (m/s)	$\langle \mathbf{v}_{rel} \rangle^d$ (m/s)	$\langle \Delta \mathbf{v}_{rel} \rangle^e$ (m/s)
2	2.8	0.0120	898	1255	712
3	1.7	0.0110	819	1134	591
4	2.1	0.0098	726	991	448
5	3.6	0.0086	630	840	297
7	6.1	0.0084	613	814	271
8	7.2	0.0080	579	759	216
10	9.4	0.0075	536	689	146
11	10.5	0.0074	530	678	135
13	12.5	0.0074	523	667	125

[a] The average change in rotational angular momentum for scattered HCl species. [b] The *J*-dependent FWHM for appearance of HCl population. [c] The lab-frame recoil velocity of HCl. [d] The COM recoil velocity of scattered HCl and excited pyrazine-h_4. [e] The average change in COM recoil velocity of the scattered collision partners.

The correlation between $\langle \Delta \mathbf{J}_{bath} \rangle$ and $\langle \Delta \mathbf{v}_{rel} \rangle$ for HCl is opposite that observed for scattered DCl, where the two quantities are positively correlated as shown in Figure 3.10. The data for scattered DCl are indicative of impulsive, unconstrained collisions where large changes in rotational angular momenta correspond to large changes in orbital angular momenta. In contrast, the data for scattered HCl suggest that the collisions occur with orienting forces present.

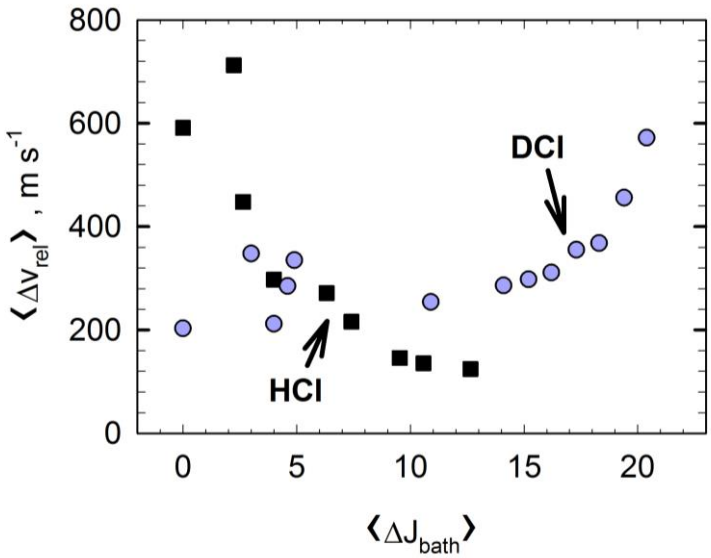

Figure 3.10. The changes in COM recoil velocities of scattered HCl and DCl have opposite correlations with the changes in their rotational angular momenta.

It is likely that the differences in the correlation of $\langle \Delta \mathbf{J}_{bath} \rangle$ and $\langle \Delta \mathbf{v}_{rel} \rangle$ for HCl and DCl are due to differences in their intermolecular interactions with pyrazine-h_4 (E_{vib}). The interaction between the energy donor and HCl appears to be strong, σ-type hydrogen-bonding interactions (Figure 3.1a) that leads to oriented collisions between them. The collisions of pyrazine-h_4 (E_{vib}) and DCl do not seem to be affected by such interactions. The differences in intermolecular interactions that appears to be present in collisional relaxation of pyrazine-h_4 (E_{vib}) with HCl and DCl could be due to a number of differences in the chemical properties of the isotopes.

The σ-type interaction (Figure 3.1a) looks like an acid-base reaction coordinate. Acid-base chemistry is possible between pyrazine-h_4 (E_{vib}) and HCl (or DCl) since pyrazine-h_4 is an aromatic Lewis base [76, 77], and HCl (or DCl) is an acid. The pKa for HCl is lower than that for DCl [78], which could be a significant factor if their interactions with pyrazine-h_4 (E_{vib}) are chemical to an extent.

The strong attractive interactions that is likely present in pyrazine-h_4 (E_{vib}) + HCl collisions could be from near-resonance effects since the vibrational frequency for pyrazine-h_4 (ν_{7b} = 3041 cm^{-1}) [49] is closer to that for HCl (ν_{HCl} = 2886 cm^{-1}) [48] than that for DCl (ν_{DCl} = 2088 cm^{-1}) [48]. The impact of near-resonance effects on molecular dynamics is demonstrated by the studies on isotopic molecular complexes, where the dissociation lifetimes and product distributions of the dissociated complexes differed between isotopes [48, 68, 70]. The dynamic differences seen in such studies were ascribed to near-resonance interactions of the molecules in the complex.

Strong interactions between pyrazine-h_4 (E_{vib}) and HCl can mediate proton tunneling, and the tunneling can affect the dynamics of the collisional energy transfer to HCl. Proton tunneling is more likely for HCl than for DCl. Proton tunneling has been shown to lead to isotope effects in the rates for proton-transfer [69], and its presence in the interactions of pyrazine-h_4 (E_{vib}) and HCl is likely to contribute to the dynamic differences in the collisional relaxation of pyrazine-h_4 (E_{vib}) with HCl and DCl.

3.3.4 Nascent Rotational Distribution of HCl Products and Energy Transfer Rate Constants

The semi-log plot for the nascent rotational distribution of HCl products after single collisions with pyrazine-h_4 (E_{vib}) is shown in Figure 3.11. The distribution is based on a Boltzmann analysis and is obtained by measuring nascent appearance populations at line center for individual *J* states of HCl and combining these measurements with Doppler-broadened line widths. Populations for each state are

measured in pairs with a common reference state to account for any experimental fluctuations. The reference state in this case is the $J = 8$ state. For a Boltzmann distribution, the population in a specific J state, pop (J), is related to the rotational temperature T_{rot} as given by Eq. 3.2.

$$\ln \frac{\text{pop}(J)}{g(J)} \propto \frac{-E_{rot}}{k_B T_{rot}} \qquad \text{Eq. 3.2}$$

Here g (J) is degeneracy of the J state, E_{rot} is the rotational energy and k_B is the Boltzmann constant. The steps for transforming IR signals into population measurements are presented in the Appendix.

The rotational distribution in Figure 3.11 shows that HCl molecules are scattered with a rotational temperature $T_{rot} = 890 \pm 90$ K. The T_{rot} value shows that HCl molecules are scattered with rotational energy gains in inelastic collisions with pyrazine-h_4 (E_{vib}). In comparison, the T_{rot} for pyrazine-h_4 (E_{vib}) + DCl collisions is

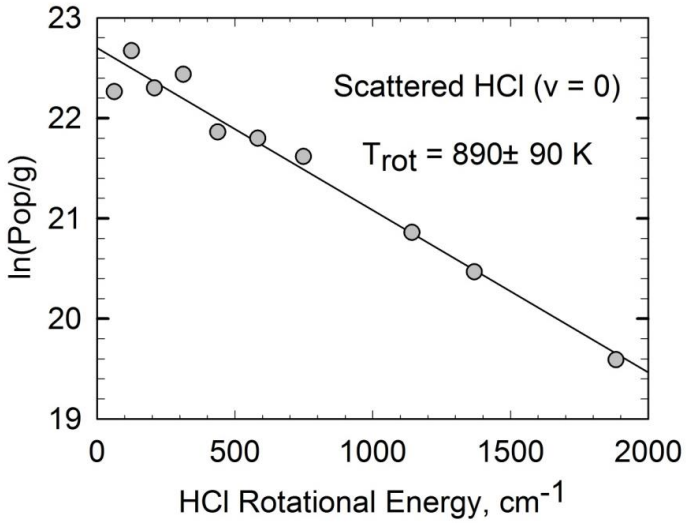

Figure 3.11. Boltzmann rotational distribution of nascent HCl (v = 0) products after collisions with pyrazine-h_4 (E_{vib}). The rotational temperature T_{rot} shows that HCl gains rotational energy from the inelastic collisions.

T_{rot} = 880 ± 100 K [5], which shows that DCl molecules are scattered on average with similar rotational energy gains as scattered HCl.

3.3.5 State-specific Energy Transfer Rate Constants

The rate constants for appearance of HCl molecules in individual *J* states after collisions with pyrazine-h_4 (E_{vib}) have been measured. The equation for this process is shown in Eq. 3.3

$$\text{pyz}\,(E_{vib}) + \text{HCl}\,(300\,\text{K}) \xrightarrow{k^{J}_{app}} \text{pyz}\,(E'_{vib}) + \text{HCl}\,(v = 0, J, \text{Vel}) \qquad \text{(Eq. 3.3)}$$

where k^J_{app} is the rate constant for appearance of HCl population in a specific *J* state and Vel is the recoil velocity of the scattered HCl molecules. The rate equation is shown in Eq. 3.4.

$$\frac{d[\text{HCl}(J)]}{dt} = k^{J}_{app}\,[\text{pyz}\,(E_{vib})][\text{HCl}\,(300\,\text{K})] \qquad \text{(Eq. 3.4)}$$

To determine the *J*-specific energy transfer rate constants, Eq. 3.4 is integrated to give Eq. 3.5 using the short-time approximation. The assumption is appropriate under single collision conditions where the concentrations of the collision partners do not change much from their initial values over the time of the measurement.

$$k^{J}_{app} = \frac{\Delta[\text{HCl}(J)]}{\Delta t}\,\frac{1}{[\text{pyz}(E_{vib})]_0[\text{HCl}(300\,\text{K})]_0} \qquad \text{(Eq. 3.5)}$$

Here $[\text{pyz}\,(E_{vib})]_0$ and $[\text{HCl}\,(300\text{ K})]_0$ are the initial concentrations of excited pyrazine-h_4 and bulk HCl, respectively. The concentration of excited pyrazine-h_4 is determined by UV absorption measurements and the experimental interaction volume. The details of the calculation are presented in the Appendix. The rate

constant for appearance of HCl in $J = 8$ state is measured directly and serves as a reference state. The k^J_{app} values for other J states are determined from the reference state rate measurements and the rotational temperature of the scattered bath species using Eq. 3.6.

$$k^J_{app} = k^{J=8}_{app} \frac{f_J(T_{rot})}{f_{J=8}(T_{rot})} \quad \text{(Eq. 3.6)}$$

Here, f_J is the fractional population in a distribution with T_{rot} measurement. The k^J_{app} values for individual J states of HCl (v = 0) are listed in Table 3.4. The k^J_{app} values are summed to give the total appearance rate constant k_{app} for collisional energy transfer.

$$k_{app} = \sum_J k^J_{app} = (6.4 \pm 1.9) \times 10^{-10} \text{ cm}^3\text{molecule}^{-1}\text{s}^{-1} \quad \text{(Eq. 3.7)}$$

Here, k_{app} is the energy transfer rate constant for pyrazine-h_4 (E_{vib}) + HCl collisions that result in HCl (v = 0) products. The average k_{app} for pyrazine-h_4 (E_{vib}) + HCl collisions is larger than that for pyrazine-h_4 (E_{vib}) + DCl collisions, where k_{app} for DCl = $(4.6 \pm 1.4) \times 10^{-10}$ cm^3 molecule^{-1} s^{-1} [5]. The larger k_{app} for HCl means that more energy transfer collisions occur between HCl and excited pyrazine-h_4 than between DCl and pyrazine-h_4 (E_{vib}). The increased rate for HCl could stem from the strong intermolecular interactions of HCl and excited pyrazine-h_4. The rate constant

TABLE 3.4: Rate Constants for Nascent Appearance of HCl (v = 0, *J*) after Collisions with Pyrazine-h_4 (E_{vib} = 37900 cm^{-1})

J	E_{rot} (cm^{-1})	k^J_{app} (10^{-12} cm^3 $molecule^{-1}$ s^{-1})
2	62.6219	48 ± 15
3	125.2057	61 ± 18
4	208.5917	69 ± 21
5	312.7294	71 ± 21
7	582.9947	62 ± 19
8	748.9588	54 ± 16
10	1142.0480	35 ± 11
11	1368.9358	27 ± 8
13	1882.7142	14 ± 4
$k_{app} = \sum k^J_{app}$		$(6.4 \pm 1.9) \times 10^{-10}$ cm^3 $molecule^{-1}$ s^{-1} *a*
$k_{L\text{-}J}$		4.9×10^{-10} cm^3 $molecule^{-1}$ s^{-1} *b*

The *J*-specific rate constant for appearance of HCl due to collisional quenching of excited pyrazine-h_4. The measured rate constant for appearance of HCl population in *J* = 8 state is the reference data that is used with T_{rot} to determine the appearance rate constants for other *J* states. *a* The sum of the appearance rate constant for all *J* states of HCl (v = 0) molecules. *b* The Lennard-Jones rate constant calculated for HCl + pyrazine-h_4 (E_{vib}) collisions. The definitions and values of all Lennard-Jones' parameters used are included in the Appendix. The Lennard-Jones rate constant falls within the uncertainty range for k_{app} for both HCl and DCl collisions with pyrazine-h_4 (E_{vib}), which shows the Lennard-Jones model potential can be used to describe the average long-range intermolecular interactions of HCl and excited pyrazine-h_4.

calculated using the Lennard-Jones collision model is $k_{L\text{-}J} = 4.9 \times 10^{-10}$ cm^3 $molecule^{-1}$ s^{-1} at 300 K. The $k_{L\text{-}J}$ value is within the uncertainty in the k_{app} for HCl and DCl, which shows that Lennard-Jones model potential is a valid description of the average long-range intermolecular potential. The similarity also suggests the branching ratio for Vibration-to-Rotation and Translation (V→RT) energy transfer is close to 100 %.

Transient IR signals for a specific *J* state is due to the change in population of HCl in that *J* state correspond to changes in population of HCl in that *J* state or changes in the velocity component along the IR probe, or both. In this way, transient IR measurements account for essentially all elastic and inelastic collisions, and can be compared directly to collision rates. A collision rate constant can also be determined from depletion measurements of bath population at 300 K. The depletion rate constant is determined by integrating the area under the depletion curves of the double Gaussian fits to the low-*J* line profiles. The equation for removal of HCl molecules from thermally populated *J* states is given in Eq. 3.8.

$$\mathrm{pyz}\,(\mathrm{E_{vib}}) + \mathrm{HCl}\,(\mathrm{J}, 300\,\mathrm{K}) \xrightarrow{k_{\mathrm{dep}}} \mathrm{pyz}\,(\mathrm{E'_{vib}}) + \mathrm{HCl}\,(\mathrm{v} = 0, J', \mathrm{Vel}) \qquad \text{(Eq. 3.8)}$$

Here *J* is the initial rotational state of HCl molecules, k_{dep} is the depletion rate constant and *J*′ is the final rotational state of the bath molecules after the inelastic collisions. The depletion rate constant is assumed to be independent of *J*. The rate for removal of *J*-specific population is shown in Eq. 3.9.

$$-\frac{\mathrm{d[HCl}(J)]}{\mathrm{d}t} = k_{\mathrm{dep}}\,[\mathrm{HCl}\,(J, 300\,\mathrm{K})][\mathrm{pyz}\,(\mathrm{E_{vib}})] \qquad \text{(Eq. 3.9)}$$

Here [HCl(*J*)] is the concentration of the population lost from state *J* and [HCl(*J*, 300 K)] is the initial concentration of that *J* state. The total depletion rate constant k_{dep} is listed in Table 3.5 for low-*J* states of HCl. The population-weighted average depletion rate constant $\langle k_{\mathrm{dep}} \rangle$ is $(8.4 \pm 3.4) \times 10^{-10}$ cm^3 molecule^{-1} s^{-1}.

TABLE 3.5: Rate constants for depletion of HCl (v = 0, J) population in collisions with Pyrazine-d_4 (E = 37900 cm^{-1})

J	E_{rot} (cm^{-1})	k^J_{dep} (10^{-10} cm^3 $molecule^{-1}$ s^{-1})
2	62.6219	9.3
3	125.2057	9.4
4	208.5917	7.3
5	312.2602	6.8
$\langle k_{dep} \rangle$ =		$(8.4 \pm 3.4) \times 10^{-10}$ cm^3 $molecule^{-1}$ s^{-1} [a]
k_{app}		$(6.4 \pm 1.9) \times 10^{-10}$ cm^3 $molecule^{-1}$ s^{-1}

The rate constant for depletion of initial HCl population in low-J states due to collisions with vibrationally hot pyrazine-h_4. [a] The weighted average depletion rate constant.

The average depletion rate constant is comparable to k_{app}, which confirms the collision rate constant determined with k^J_{app} measurements. The uncertainty in the total depletion rate constant is slightly larger than that for the total appearance rate constant due to a wider spread in the uncertainty in the parameters from the double Gaussian fitting. Figure 3.5 shows the nascent Doppler-broadened line profiles for low-J states of HCl with the residuals from the double Gaussian fits plotted below each line profile. Overall, the relative appearance component of the line profile is larger for the higher J states and leads to smaller residuals in the fitting.

The root-mean-square (rms) noise for the residuals in Figure 3.5 shows a decrease with increasing J state, with the J = 2 rms noise being larger than that for the J = 5 state. Additionally, the line profiles measured for pyrazine-h_4 (E_{vib}) + HCl collisions show some degree of asymmetry (Figure 3.5), which introduces error in the intensity and width of the depletion component. The extent of the asymmetry was minimized by being careful with the IR mode quality and the frequency lock.

3.3.6 Full Energy Transfer Distribution Function $P(\Delta E)$

The *J*-specific energy gain data presented so far has been described in terms of the amount of energy loss ΔE by the excited pyrazine-h_4 in the collisions [60, 65]. ΔE is the sum of the changes in rotational energy ΔE_{rot} for HCl and center-of-mass frame translational energy ΔE_{rel} of scattered molecules. The *J*-specific energy transfer probability distribution function $P_J(\Delta E)$ gives the translational energy distribution for a specific HCl *J*-state.

$$P_J(\Delta E)d(\Delta E) = \frac{4\pi}{\mu}\frac{k_{app}^J}{k_{col}} v_{rel,f}\left(\frac{\mu}{2\pi k_B T_{rel}}\right)^{\frac{3}{2}} \exp\left(\frac{-\mu v_{rel,f}^2}{2k_B T_{rel}}\right) d(\Delta E) \quad \text{(Eq. 3.10)}$$

Here $v_{rel,f}$ is the final COM frame velocity of the scattered molecules and k_{col} is the collision rate constant. The collision rate constant is used to normalize the distribution and can be either the total appearance rate constant k_{app} or the Lennard-Jones rate constant $k_{L\text{-}J}$. The collision rate constant k_{app} is used to normalize the energy transfer distribution function presented in this Chapter. Definitions for other quantities in Eq. 3.10 are in the preceding sections of this Chapter or the Appendix. The quantity $v_{rel,f}$ is related to ΔE as shown in Eq. 3.11.

$$v_{rel,f}^2 = \frac{2}{\mu}\left(\Delta E - \Delta E_{rot}\right) + \left\langle v_{rel,i}\right\rangle^2 \quad \text{(Eq. 3.11)}$$

Here $\langle v_{rel,i}\rangle$ is the average initial COM frame velocity of HCl and excited pyrazine-h_4. The minimum ΔE gained by the bath molecule in each *J* state is ΔE_{rot} in order to obtain real $v_{rel,f}$ values. The quantity $\langle \Delta v_{rel,i}\rangle$ is determined from the initial COM translational temperature of HCl and excited pyrazine-h_4, $T_{rel,i}$, as described by Eq. 3.12

$$\left\langle v_{rel,i} \right\rangle^2 = \frac{8k_B T_{rel,i}}{\pi\mu} \qquad \text{(Eq. 3.12)}$$

The change in rotational energy ΔE_{rot} for individual J states of scattered HCl is

$$\Delta E_{rot} = BJ_f\left(J_f + 1\right) - B\langle J_i\rangle\left(\langle J_i\rangle + 1\right) \qquad \text{(Eq. 3.13)}$$

where J_f is the rotational state of the bath molecule after collisions and $\langle J_i\rangle$ is the average rotational state of HCl before the collisions. The $P_J(\Delta E)$ for all J states are summed as shown in Eq. 3.14 to give the total energy transfer probability distribution $P(\Delta E)$ plot in Figure 3.12:

$$P(\Delta E) = \sum_{\Delta E} P_J \Delta E \qquad \text{(Eq. 3.14)}$$

The $P(\Delta E)$ function is a sum of all energy transfer events that occur via the V→RT pathway to produce HCl (v = 0) molecules. Positive ΔE values represent energy losses by pyrazine-h_4 (E_{vib}) in the inelastic collisions while negative ΔE values represent its energy gains. The bumps in $P(\Delta E)$ curve are due to the different ΔE_{rot} values for J states of scattered HCl. Data in Figure 3.12 show excited pyrazine-h_4 is more likely to lose than gain energy in collisions with thermal HCl.

In Figure 3.13 is a comparison plot of $P(\Delta E)$ for scattered HCl and DCl. The two plots are normalized to the total appearance rate constant k_{app} measured for each isotope. Both plots show that excited pyrazine-h_4 loses energy in most collisions with HCl and DCl. The peak of the $P(\Delta E)$ curve obtained with HCl is higher than that obtained with DCl due to the larger collision rate for pyrazine-h_4 (E_{vib}) + HCl collisions compared to pyrazine-h_4 (E_{vib}) + DCl collisions.

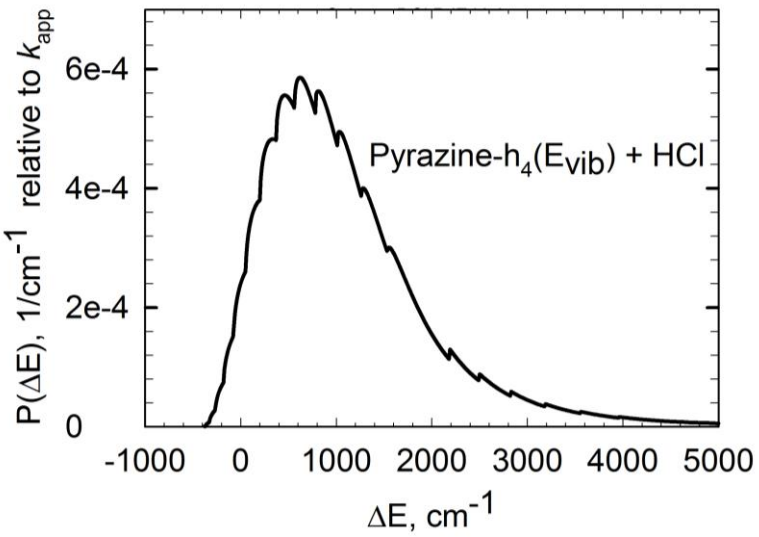

Figure 3.12. The energy transfer probability distribution for single collisions between HCl and excited pyrazine-h_4. The distribution shows that HCl is more likely to gain than loose energy from the inelastic collisions.

On average, the energy donor loses $\langle \Delta E \rangle = 1140$ cm^{-1} of energy when it collides with HCl and $\langle \Delta E \rangle = 900$ cm^{-1} when it collides with DCl. The larger $\langle \Delta E \rangle$ lost with HCl is due to the broader velocity distribution for low-*J* states of HCl, where most of the scattered bath population are found. Although pyrazine-h_4 (E_{vib}) has lots of energy, approximately 95% of HCl and DCl populations are scattered with $\Delta E \leq$ 3000 cm^{-1}, which highlights the preference for small energy changes in collisional energy transfer. In addition, a large portion of the vibrational energy $\langle E_{vib} \rangle$ in excited pyrazine-h_4 is found in the vibrational modes with frequencies ≤ 3000 cm^{-1} as shown in Figure 3.14. This means that most of the energy transferred to HCl or DCl in the inelastic collisions are likely from these modes.

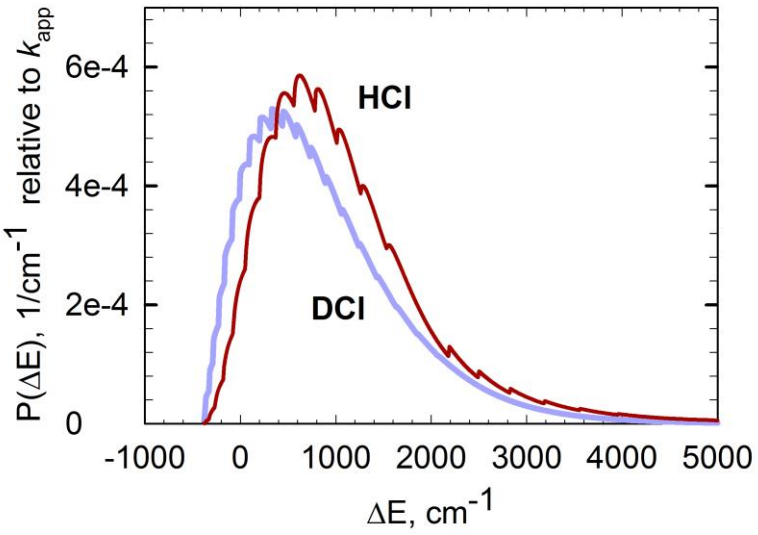

Figure 3.13. The energy transfer probability distribution for inelastic scattering of HCl and DCl molecules with pyrazine-h_4 (E_{vib}). The average energy gained by HCl in the collisions is higher than that gained by DCl.

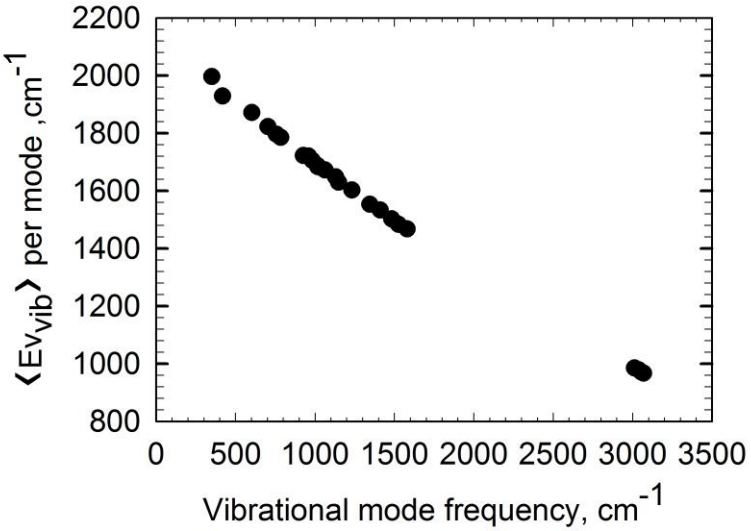

Figure 3.14. The distribution of the energy in pyrazine-h_4 (E_{vib}) among its vibrational modes. A large portion of the energy is found in the low-frequency vibrational modes.

It is interesting to compare the $\langle \Delta E \rangle$ values for scattered HCl and DCl with the vibrational modes of pyrazine-h_4. The $\langle \Delta E \rangle_{HCl}$ = 1140 cm^{-1} is close to the ν_{18a} vibrational frequency for pyrazine-h_4 (ν_{18a} = 1144 cm^{-1}) while $\langle \Delta E \rangle_{DCl}$ = 900 cm^{-1} is close to the ν_5 vibrational frequency for pyrazine-h_4 (ν_5 = 918.6 cm^{-1}) [49]. One might conclude from the similarities between the $\langle \Delta E \rangle$ values and these vibrational frequencies that the energy transfer to HCl and DCl are solely from ν_{18a} and ν_5 modes respectively. But, the $P(\Delta E)$ curves show the molecules are scattered with different ΔE, which should not be the case if the energy transfer is from a single mode of the energy donor. This point highlights the benefits of using state-resolved methods for collisional energy transfer studies.

3.4 Conclusion

Thermal HCl and DCl molecules gain rotational and translational energies from collisional relaxation of highly excited pyrazine-h_4 molecules. Although, the HCl and DCl isotopes are scattered with similar rotational distributions, the average collision rate for pyrazine-h_4 (E_{vib}) and HCl is larger than that for pyrazine-h_4 (E_{vib}) and DCl. The data show opposite correlations between scattered HCl and DCl for changes in rotational angular momenta and COM recoil velocities, which suggests substantial differences in their intermolecular interactions with excited pyrazine-h_4. The larger $\langle \Delta E \rangle$ value for scattered HCl compared to that for scattered DCl is a result of the broader translational energy distribution for low-J states of scattered HCl, and most of the scattered bath populations are in the these J states.

Chapter 4: Vibration-Vibration Energy Transfer in Collisional Relaxation of Pyrazine-h_4 (E_{vib} = 37900 cm^{-1}) with 300 K HCl

4.1 Introduction

Vibration-to-vibration (V→V) energy transfer is a potential pathway for collisional deactivation of excited molecules [2, 5, 10, 11, 79-81]. A number of studies show that relaxation of excited molecules by V→V pathway occurs with small changes to the rotational and translational energies of the energy acceptor [10, 14, 15, 81]. An increase in the V→V energy transfer probability ($P_{v\text{-}v}$) decreases the vibration-to-rotation and translation (V→RT) probability relative to the overall energy transfer probability. The V→V energy transfer dynamics for collisions of highly excited pyrazine-h_4 (E_{vib} = 37900 cm^{-1}) with 300 K HCl are presented in this Chapter. The results are compared to the data for V→RT energy transfer in Chapter 3. The V→V energy transfer studies offer insight into the presence of a possible resonance between the vibrational motion of HCl and excited pyrazine-h_4 that leads to the observed isotope effects for HCl and DCl collisions discussed in Chapter 3.

The probability for V→V energy transfer is dependent on the energy difference $\Delta E_{v\text{-}v}$ between the vibrational transitions of the donor and acceptor molecules. $P_{v\text{-}v}$ increases with decreasing $\Delta E_{v\text{-}v}$ and is highest when the vibrational transitions are in resonance ($\Delta E_{v\text{-}v}$ = 0) [7]. Other factors that affect $P_{v\text{-}v}$ include

intermolecular interactions of the collision pair, the amount of vibrational energy available for transfer and the reduced mass of the molecules involved in the collision.

The probability for V→V energy transfer in the inelastic collisions can be described using Born approximation that the energy of the intermolecular potential is much smaller than the relative translational energy of the collision partners. Based on this approximation, the probability for vibrational transition from initial state i to final state f is given in Eq. 4.1:

$$P_{if} = \left(\frac{2\pi}{h}\right)^2 \left| \int_{-\infty}^{\infty} V_{if}(t) \exp(i\Delta\omega t) dt \right|^2, V_{if}(t) = \langle i | V(t) | f \rangle \qquad \text{(Eq. 4.1)}$$

with V(t) representing the time-dependent interaction potential of the molecules involved in the energy transfer collision and Δω representing the frequency difference of their vibrational transitions [2, 7, 11, 79]. The interaction potential depends on (∂μ/∂Q), which is the change in charge distributions of the collision partners with respect to the change in their normal vibrational coordinates during the interaction [7]. The V→V energy transfer probability increases with ∂μ/∂Q. This process is similar to the quantum mechanical treatment for the absorption of an IR photon.

The time-dependence of the interaction potential of the collision partners affects $P_{v\text{-}v}$. Rapid changes in the potential at short times result in Fourier components with large Δω values while the slower changes in the potential at the attractive part lead to Fourier components with small Δω values [2, 7, 11, 79]. $P_{v\text{-}v}$ is enhanced at lower Δω values, which implies long-range attractive forces are contributing to V→V energy transfer. In contrast, short-range repulsive forces contribute to V→RT energy transfer probability since the energy transfer is enhanced at large Δω values. The

results for V→V relaxation of pyrazine-h_4 (E_{vib}) with thermal HCl will shed light on the type of interactions that are important for the collisional energy transfer of high energy molecules.

Wodtke and co-workers demonstrated the dependence of $P_{v\text{-}v}$ on the vibrational energy content of the energy donor through collisional relaxation of highly excited O_2 (v = 15-26) with bath CO_2, N_2O and O_3 gases [9]. They showed that for 1 vibrational quantum change in both the energy donor and acceptor $\Delta E_{v\text{-}v}$ decreases with increasing vibrational excitation of O_2. The rate constant for V→V energy transfer was largest when O_2 was excited to the vibrational level that leads to the smallest $\Delta E_{v\text{-}v}$ value. Large $\Delta E_{v\text{-}v}$ values at low levels of vibrational excitation of O_2 are due to larger energy spacing between the vibrational states of O_2 compared to those of CO_2 and N_2O. The wider energy gaps for O_2 are a result of its lower moment of inertia. The energy gaps for O_2 become smaller at higher levels of vibrational excitation due to increasing anharmonicity of its vibration.

The reduced mass of the collision partners affects $P_{v\text{-}v}$. Isotopic data from collisional quenching of excited $^{12}C^{16}O_2$ molecules with 300 K bath molecules such as $^{14}N_2{}^{16}O$ and $^{15}N_2{}^{16}O$ show that V→V energy transfer probability is less for the heavier isotope [8]. The heavier isotope has smaller energy gaps between its vibrational states, which result in larger $\Delta E_{v\text{-}v}$ for their interactions with excited CO_2.

The V→V energy transfer channel was observed in collisions of pyrazine-h_4 (E_{vib}) with DCl [5]. The closest vibrational frequencies for DCl and pyrazine are ν_{DCl} = 2088 cm^{-1} [48] and ν_{8a} = 1578 cm^{-1} [49] respectively. It is likely that V→V energy

transfer to HCl (ν_{HCl} = 2886 cm^{-1}) [48] will also occur and might be enhanced relative to that of DCl, due to $\Delta\omega$ smaller values.

4.2 Experimental Methods

The experimental set-up is described in Chapter 2. The summary of the set-up is given here along with the details specific to this study. Vibrationally hot pyrazine-h_4 molecule (E_{vib} = 37900 cm^{-1}) was prepared in the gas-phase by excitation with a single photon of the 4th harmonic output of a pulsed Nd:YAG laser (λ = 266 nm). A 1:1 ratio of excited pyrazine-h_4 and 300 K gas-phase HCl were flowed through a 3-m collision cell at a total pressure of $\leq$ 40 mTorr. The gas-kinetic collision time was t_{col} ~ 2 μs. The outcome of single collisions between excited pyrazine-h_4 and HCl was measured at t = 1 μs by monitoring individual *J* states of scattered HCl (v = 1) molecules. The probe transitions were the R-branch lines for HCl (v = 1) molecules. These are listed in Table 4.1. The probe light was the idler output of a CW mid-IR OPO ($\lambda \approx$ 3.2 to 3.9 μm).

Transient IR signals were collected after modulating and stabilizing the OPO output through the active feedback control described in Chapter 2. The OPO output was locked to line center frequency ν_0 of a HCl ro-vibrational transition for measurements of population changes at ν_0. Measurements of nascent Doppler-broadened line profiles were made by locking the OPO output to a single fringe of a Fabry-Perot etalon. A pulse generator with a variable delay was used to synchronize the timing of the 266 nm pulse with the IR modulation.

TABLE 4.1: The R-branch lines for HCl (v = 1)[a]

$H^{35}Cl$ (v = 1, J) + hν ($\lambda \sim 3.4\ \mu$m) $\rightarrow$ $H^{35}Cl$ (v = 2, J + 1)			
J	ν_0 (cm^{-1})[b]	E_{rot} (cm^{-1})[c]	S_J (cm $molecule^{-1}$)[d]
0	2801.6721	0.0000	3.601×10^{-25}
1	2820.7238	20.2702	6.393×10^{-25}
2	2839.1481	60.7979	7.709×10^{-25}
3	2856.9330	121.5583	7.486×10^{-25}
4	2874.0669	202.5138	6.174×10^{-25}
5	2890.5385	303.6145	4.429×10^{-25}
6	2906.3366	424.7981	2.801×10^{-25}
7	2921.4502	565.9899	1.573×10^{-25}
8	2935.8689	727.1031	7.888×10^{-26}
9	2949.5822	908.0384	3.546×10^{-26}
10	2962.5801	1108.6848	1.433×10^{-26}

[a] Listed quantities are from the HITRAN database [73]. [b] IR frequency at the center of an absorption line for HCl. [c] *J*-specific rotational energy for HCl. [d] The absorption line strength for individual rotational states of HCl.

4.3 Results and Discussion

The V$\rightarrow$V energy transfer channel has been measured at t = 1 μs for inelastic collisions of pyrazine-h_4 (E_{vib}) and thermal HCl. *J*-specific rate constants for the energy transfer are presented along with the corresponding nascent Doppler-broadened line profiles that result from the energy transfer. The rotational distribution of HCl (v = 1) molecules at t = 1 μs are also included in the results. The scattered HCl (v = 1) data are compared to scattered HCl (v = 0) data in order to see if the collision dynamics differ between the two relaxation pathways. Comparing the data for the two

relaxation channels will offer insight into the possible role of vibrational resonance of the energy donor and acceptor in causing the isotope effects discussed in Chapter 3 for the collisional quenching of pyrazine-h_4 (E_{vib}) with HCl and DCl.

4.3.1 Transient IR Measurements for Scattered HCl (v = 1) Molecules

Transient IR absorption signals for HCl molecules that are vibrationally excited after single collisions with pyrazine-h_4 (E_{vib}) have been collected for the J = 1-7 states of scattered HCl. Scattered HCl (v = 1, J = 0) molecules are not observed and the amount of population scattered into $J \geq 8$ state is below the detection sensitivity of the transient IR spectrometer. The absence of pure vibrationally excited HCl molecules reveals that at least some rotational energy in HCl accompanies the V→V energy transfer. Rotational energy changes of the bath gas help meet the energy difference $\Delta E_{v\text{-}v}$ that is needed for V→V energy transfer.

Figure 4.1 shows the transient IR measurement collected at line center ν_0 for R6 transition of the HCl (v = 1) state. The transient signal shows nascent appearance of HCl (v = 1, J = 6) population after single collisions with excited pyrazine-h_4. The HCl (v = 1) collision products are in v = 0 state prior to the inelastic collisions with pyrazine-h_4 (E_{vib}). HCl (v = 1, J = 6) collision products show HCl gains vibrational

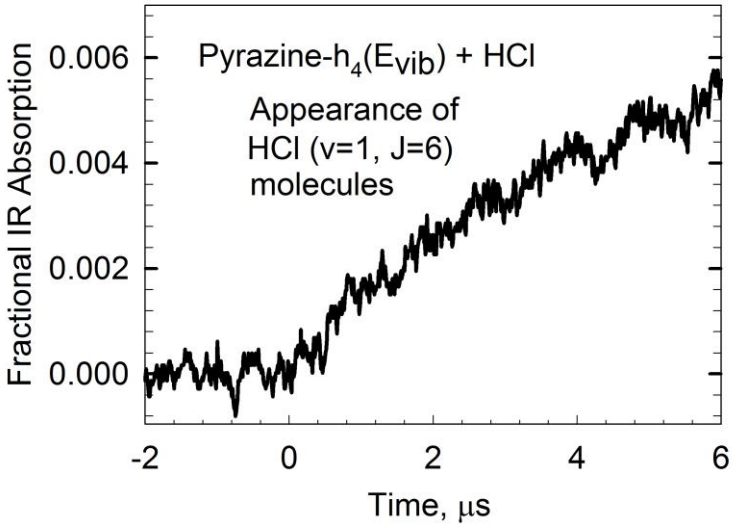

Figure 4.1. Transient IR signal showing nascent appearance of HCl (v = 1, *J* = 6) molecules.

and rotational energy from collisional relaxation of pyrazine-h_4 (E_{vib}). The vibrationally excited bath molecules also gain translational energy from the inelastic collisions as shown by the nascent Doppler-broadened line profiles in Figure 4.2. The data in Figure 4.2 are collected at *J* = 2, 3, 6 and 7 states. The line profiles show nascent appearance of HCl (v = 1, *J*) populations after collisions of thermal HCl with pyrazine-h_4 (E_{vib}). Only appearance population is seen across the v = 1 line profiles since nearly 100 % of HCl molecules are in the v = 0 state at 300 K. The line profiles are each fit with a single Gaussian function:

$$F(\nu) = F_0 + I_{app} \exp\left(-4\ln 2\left(\frac{\nu - \nu_0}{\Delta\nu_{app}}\right)^2\right) \qquad \text{(Eq. 4.2)}$$

where F_0 is a small offset of the line profile, I_{app} is the line center IR intensity for appearance population, ν is the IR frequency, $\Delta\nu_{app}$ is the full width at half maximum

(FWHM) of the appearance line profile. The translational temperature T_{app} of the scattered bath molecules is determined for individual *J* states from Δv_{app}. Figure 4.2

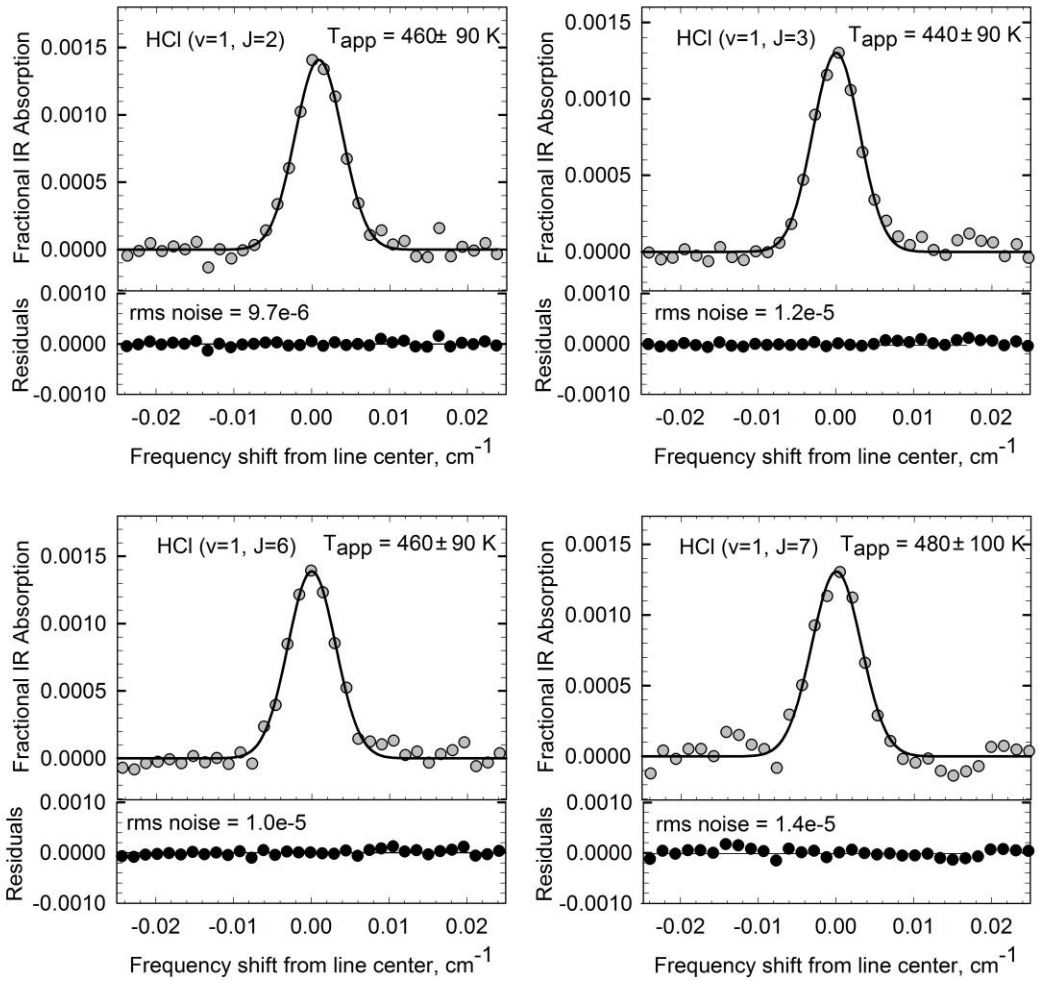

Figure 4.2. The nascent Doppler-broadened line profiles for a number of *J* states for scattered HCl (v = 1) species. HCl becomes vibrationally excited in the inelastic collisions with an increase in average translational energy.

shows that the vibrationally excited bath molecules are scattered in individual *J* states with T_{app} slightly greater than 300 K. The post-collision bath molecules gain modest amounts of translational energy along with the vibrational excitation.

4.3.2 Nascent Translational Temperatures for HCl (v = 1) Collision Products

Listed in Table 4.2 are the *J*-specific translational temperatures for HCl molecules excited vibrationally in nascent collisions with pyrazine-h_4 (E_{vib}). The average translational temperatures in lab-frame T_{app} values and center-of-mass (COM) frame T_{rel} values show that HCl (v = 1, *J*) species that result from the inelastic collisions gain some translational energy on average with the vibrational excitation. The amount of translational energy gain by HCl (v = 1) collision products is relatively constant with *J* and is much lower than the translational energy gains by scattered HCl (v = 0) molecules in low-*J* states as shown in Figure 4.3.

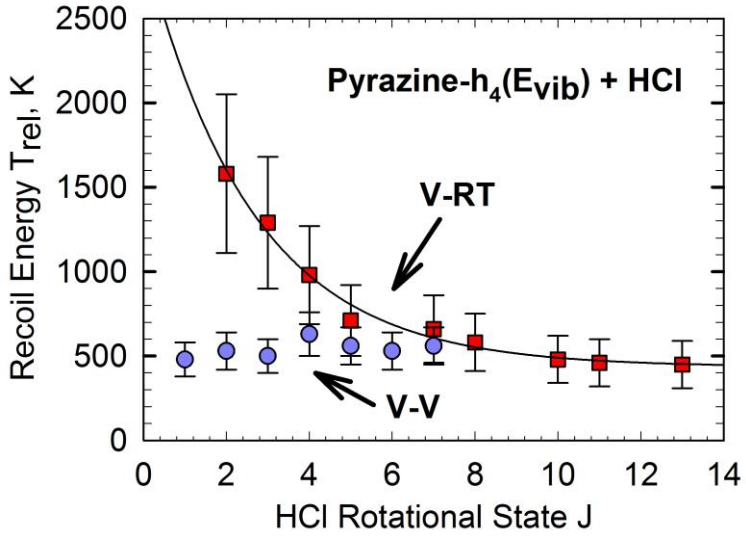

Figure 4.3. A comparison of the Trel for V→V and V→RT energy transfer shows scattered HCl (v = 0) molecules undergo larger translational temperature changes in collisions with pyrazine-h_4 (E_{vib}) than scattered HCl (v = 1) species.

TABLE 4.2: Nascent Doppler-broadened FWHM and translational temperatures for appearance of scattered HCl molecules in v = 1 state.

J state	$\Delta\nu_{app}$ (cm^{-1})[a]	T_{app} (K)[b]	T_{rel} (K)[c]
1	0.0069	430 ± 90	480 ± 100
2	0.0072	460 ± 90	530 ± 110
3	0.0071	440 ± 90	500 ± 100
4	0.0078	520 ± 100	630 ± 130
5	0.0075	480 ± 100	560 ± 110
6	0.0069	460 ± 90	530 ± 100
7	0.0076	480 ± 100	560 ± 110

[a] The full width at half maximum (FWHM) for appearance line profile of HCl. [b] The appearance lab-frame translational temperature for scattered HCl molecules. [c] The COM frame translational temperature for recoiling HCl. The calculations for T_{app} and T_{rel} are included in the Appendix.

Translational energy gain by HCl (v = 0) collision products is dependent on *J* with scattered molecules in high-*J* states having lower translational energy gains than those in low-*J* states (Figure 4.3). In contrast, the translational energy gain by scattered HCl (v = 1) molecules is relatively the same for all *J* states. The *J*-independent low translational energy gains by scattered HCl (v = 1) molecules are characteristic of V→V energy transfer collisions [10, 14, 15, 81].

4.3.3 Angular Momentum and Recoil Velocity Changes of HCl (v = 1)

The average changes in rotational angular momentum for HCl $\langle\Delta\mathbf{J}_{bath}\rangle$ and COM recoil velocity $\langle\Delta\mathbf{v}_{rel}\rangle$ that accompany vibrational excitation of HCl in single collisions with excited pyrazine-h_4 are listed in Table 4.3. Angular momentum is conserved in the inelastic collisions if $\Delta\mathbf{L} + \Delta\mathbf{J}_{bath} + \Delta\mathbf{J}_{donor} = 0$, where $\Delta\mathbf{L}$ is the

change in orbital angular momentum, $\Delta\mathbf{J}_{bath}$ is the change in rotational angular momentum of HCl and $\Delta\mathbf{J}_{donor}$ is the change in rotational angular momentum of

TABLE 4.3: *J*-specific changes in rotational angular momentum and recoil velocities for scattered HCl (v = 1) molecules

final *J* state	$\langle\Delta\mathbf{J}_{bath}\rangle^a$	$\Delta\nu_{app}{}^b$	$\langle\mathbf{v}_{lab}\rangle^c$ (m/s)	$\langle\mathbf{v}_{rel}\rangle^d$ (m/s)	$\langle\Delta\mathbf{v}_{rel}\rangle^e$ (m/s)
1	3.3	0.0069	542	699	156
2	2.8	0.0072	561	730	187
3	1.7	0.0071	549	709	167
4	2.1	0.0078	596	787	244
5	3.6	0.0075	573	749	206
6	4.9	0.0069	561	730	187
7	6.1	0.0076	573	749	206

[a] The average change in rotational angular momentum for scattered HCl (v = 1) molecules. [b] The *J*-dependent FWHM for appearance of HCl population. [c] The average lab-frame recoil velocity of HCl: $\langle\mathbf{v}_{lab}\rangle = (3k_BT_{app}/2m_{HCl})^{1/2}$ where k_B is the Boltzmann constant, T_{app} and m_{HCl} are as defined in Table 4.2. [d] The average COM recoil velocity of scattered HCl and pyrazine-h_4 (E_{vib}) determined from $\langle\mathbf{v}_{rel}\rangle = (M/m_{pyz}) \cdot [\langle\mathbf{v}_{lab}\rangle^2 - (3k_BT/M)]^{1/2}$, where M is the sum of the masses of HCl and pyrazine-h_4. Other quantities are defined in Table 4.2. [e] The average change in $\mathbf{v}_{rel}$ is $\langle\Delta\mathbf{v}_{rel}\rangle = \langle\mathbf{v}_{rel}\rangle - (3k_BT/\mu)^{1/2}$ with μ being the reduced mass of HCl and pyrazine-h_4.

excited pyrazine-h_4. A reasonable assumption is made that $\Delta\mathbf{J}_{bath}$ and $\Delta\mathbf{J}_{donor}$ values have the same sign based on inelastic collision studies by Waclawik and Lawrance [75]. Therefore, $\Delta\mathbf{J}_{bath} + \Delta\mathbf{J}_{donor} = -\Delta\mathbf{L} = -\mathbf{b}\mu\Delta\mathbf{v}_{rel}$. Here, **b** is the impact parameter and μ is the reduced mass of HCl and pyrazine-h_4 (E_{vib}). The average change in rotational angular momentum of HCl is determined from $\langle\Delta\mathbf{J}_{bath}\rangle = |(\mathbf{J'}_{bath})^2 - \langle\mathbf{J}_{bath}\rangle^2|$ where $\mathbf{J'}_{bath}$ is the post-collision rotational angular momentum of HCl and $\langle\mathbf{J}_{bath}\rangle$ is the

average rotational angular momentum of HCl before the inelastic collisions and is equal to 3.4.

Table 4.3 shows HCl molecules are scattered from pyrazine-h_4 (E_{vib}) with $\langle \Delta \mathbf{J}_{bath} \rangle$ = 1.7-6.1 and $\langle \Delta \mathbf{v}_{rel} \rangle$ = 156-206 m/s. The small rotational angular momenta changes for scattered HCl (v = 1) species are accompanied by small changes in COM recoil velocities, which are evidences of angular momentum conservation in the inelastic collisions. Recoiling HCl molecules in v = 1 state undergo smaller changes in $\langle \Delta \mathbf{J}_{bath} \rangle$ and $\langle \Delta \mathbf{v}_{rel} \rangle$ compared to the recoiling molecules in v = 0 state whose $\langle \Delta \mathbf{J}_{bath} \rangle$ = 1.7-12.5 and $\langle \Delta \mathbf{v}_{rel} \rangle$ = 125-712 m/s as shown in Figure 4.4. The smaller $\langle \Delta \mathbf{J}_{bath} \rangle$ and $\langle \Delta \mathbf{v}_{rel} \rangle$ values for vibrationally excited HCl result from collisions that occur at the attractive wall of the interaction potential while the larger values for scattered HCl (v = 0) molecules are due to collisions that occur at the repulsive wall of the potential.

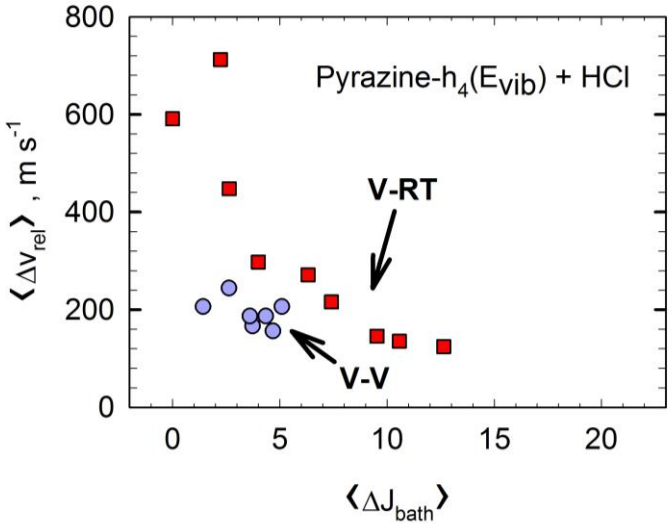

Figure 4.4. A comparison of the changes in HCl rotational angular momentum and COM recoil velocity that accompany V→V and V→RT energy transfers. The $\langle \Delta \mathbf{J}_{bath} \rangle$ and $\langle \Delta \mathbf{v}_{rel} \rangle$ values for V→RT energy transfer are much larger than those for V→V energy transfer.

4.3.4 Nascent Rotational Distribution of HCl (v = 1) Collision Products

The nascent rotational distribution of scattered HCl molecules in the v = 1 state is shown in Figure 4.5. The distribution is obtained by measuring transient population at line center of R-branch transitions for HCl (v = 1). Measurements of

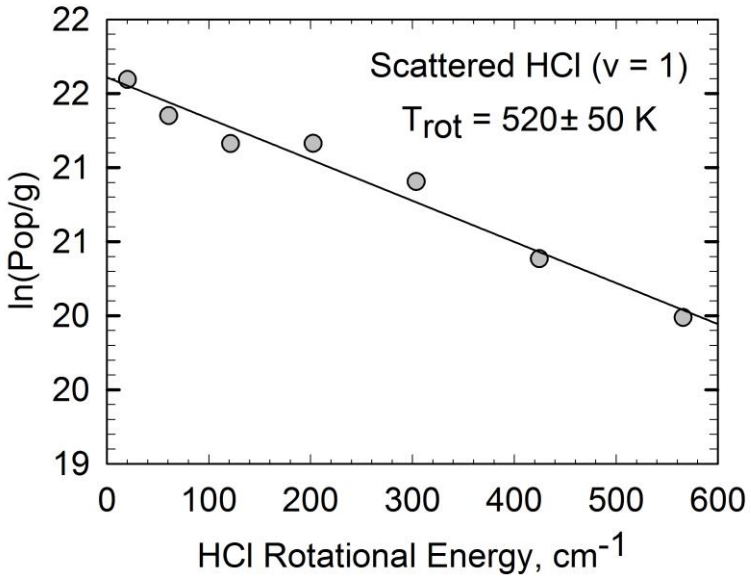

Figure 4.5. Rotational distribution of nascent HCl (v = 1) products after collisions with pyrazine-h_4 (E_{vib}). The rotational temperature shows HCl (v = 1) molecules gain rotational energy from the inelastic collisions.

UV absorption by pyrazine-h_4 are taken with each population measurement to correct for experimental fluctuations. Using the Boltzmann rotational distribution, the *J*-specific nascent population, pop (*J*) is related to the rotational temperature T_{rot} as shown in Eq. 4.3.

$$\ln \frac{\text{pop}(J)}{g(J)} \propto \frac{-E_{rot}}{k_B T_{rot}} \qquad \text{Eq. 4.3}$$

Here, g (*J*) is the $2J + 1$ rotational degeneracy, E_{rot} is the rotational energy of the *J* state and k_B is the Boltzmann constant. The resulting $T_{rot} = 520 \pm 50$ K shows that HCl molecules that become vibrationally excited in single collisions with pyrazine-h_4 (E_{vib}) also gain some rotational energy on average from the collisions. The average rotational energy gain by scattered HCl (v = 1) molecules is less than that for scattered HCl (v = 0) molecules ($T_{rot} = 890 \pm 90$ K). The lower rotational temperature for scattered HCl (v = 1) molecules highlights the long-range nature of the collisions since such collisions result in low gains in rotational energy. On the other hand, the higher T_{rot} value for scattered HCl (v = 0) molecules supports the short-range nature of such collisions since they lead to high gains in rotational energy.

4.3.5 Absolute Rate Constant Measurements for HCl (v = 1, *J*) Production

The absolute rate constants k^J_{app} for scattering of HCl molecules into individual *J* states in v = 1 state are presented here. The equation for the inelastic collisions is shown in Eq. 4.4

$$\text{pyz}\,(E_{vib}) + \text{HCl}\,(300\,\text{K}) \xrightarrow{k^J_{app}} \text{pyz}\,(E'_{vib}) + \text{HCl}\,(v = 1, J, \text{Vel}) \qquad \text{(Eq. 4.4)}$$

where Vel is the recoil velocity of the scattered bath molecules. The rate of appearance of HCl (v = 1) molecules is determined from Eq. 4.5.

$$\frac{d[\text{HCl}(v = 1, J)]}{dt} = k^J_{app}\,[\text{pyz}\,(E_{vib})][\text{HCl}\,(300\,\text{K})] \qquad \text{(Eq. 4.5)}$$

Eq. 4.5 is integrated in the short-time limit to obtain Eq. 4.6 by assuming small changes in the initial concentrations of HCl and excited pyrazine-h_4 in the duration of the nascent measurements.

$$k_{app}^{J} = \frac{\Delta[\mathrm{HCl}(v=1, J)]}{\Delta t} \frac{1}{[\mathrm{pyz}(E_{vib})]_0 [\mathrm{HCl}(300\,\mathrm{K})]_0} \qquad \text{(Eq. 4.6)}$$

Here, $[\mathrm{pyz}\ (E_{vib})]_0$ and $[\mathrm{HCl}\ (300\ \mathrm{K})]_0$ are the pre-collision concentrations of pyrazine-h_4 (E_{vib}) and HCl respectively. The rate constant for appearance of vibrationally excited HCl in J = 2 state is measured directly and the measurement is used together with the nascent rotational temperature to obtain k^J_{app} values for other J states of scattered HCl (v = 1) molecules in Eq. 4.7.

$$k_{app}^{J} = k_{app}^{J=2} \frac{f_J(T_{rot})}{f_{J=8}(T_{rot})} \qquad \text{(Eq. 4.7)}$$

Here, f_J is the J-specific fractional population of recoiling HCl in v = 1 state. Table 4.4 shows that HCl collision products in the v = 1 state are scattered in individual J states with comparable rates. The sum of the k^J_{app} values in Eq. 4.8 yields the total rate constant k_{app} (v = 1) for vibrational excitation of HCl in v = 1 state.

$$k_{app}(v=1) = \sum_J k_{app}^{J} = (2.9 \pm 0.3) \times 10^{-12}\ \mathrm{cm^3 molecule^{-1} s^{-1}} \qquad \text{(Eq. 4.8)}$$

TABLE 4.4: State-Resolved Rate Constants for Nascent Appearance of HCl (v = 1) after Collisions with Pyrazine-h_4 (E_{vib} = 37900 cm^{-1})

J	E_{rot} (cm^{-1})	k^J_{app} (10^{-13} cm^3 $molecule^{-1}$ s^{-1})
1	20.2702	2.2 ± 0.2
2	60.7979	3.3 ± 0.3
3	121.5583	4.0 ± 0.4
4	202.5138	4.1 ± 0.4
5	303.6145	3.8 ± 0.4
6	424.7981	3.2 ± 0.3
7	565.9899	2.5 ± 0.2
k_{app} (v = 1) = $\sum k^J_{app}$		(2.9 ± 0.3) × 10^{-12} cm^3 $molecule^{-1}$ s^{-1}[a]
k_{app} (v = 0)		(6.4 ± 1.9) × 10^{-10} cm^3 $molecule^{-1}$ s^{-1}[b]
k^{tot}_{app} = k_{app} (v = 1) + k_{app} (v = 0)		(6.4 ± 1.9) × 10^{-10} cm^3 $molecule^{-1}$ s^{-1}[c]

The *J*-specific absolute rate constant for the appearance of HCl (v = 1) species due to collisional quenching of excited pyrazine-h_4. [a] The total appearance rate constant for *J* states of HCl (v = 1) molecules. [b] The total appearance rate constant for all *J* states of HCl (v = 0) molecules. [c] The total rate constant for collisional quenching of excited pyrazine-h_4 by HCl. The collision rate for vibrational excitation of HCl shows that such excitation occurs in 1 out of 200 single collisions of HCl and excited pyrazine-h_4.

The V→V energy transfer rate constant k_{app} (v = 1) is less than 1% of the total rate constant k^{tot}_{app} for collisional relaxation of excited pyrazine-h_4 reported in Table 4.4. The k_{app} (v = 1) value is much less than the V→RT energy transfer rate constant k_{app} (v = 0), also reported in Table 4.4. The small rate constant for V→V energy transfer reveals that less than 1% of pyrazine-h_4 (E_{vib}) + HCl collisions lead to vibrational excitation of HCl. The large rate constant for V→RT energy transfer shows it is the dominant pathway for collisional relaxation of excited pyrazine-h_4.

4.4 Conclusion

The V→V energy transfer channel is a minor pathway for the collisional quenching of excited pyrazine-h_4 by thermal HCl, compared to the V→RT energy transfer channel. Nascent HCl (v = 1) collision products gain less rotational energy compared to the scattered HCl molecules in the v = 0 state. The vibrational excitation of HCl is also accompanied by lower translational energy gains compared to those for scattered v = 0 molecules. The lower rotational and translational energy gains for scattered HCl (v = 1) species are characteristic of collisions mediated by long-range attractive forces. The higher rotational and translational energy gains for scattered HCl (v = 0) species are representative of collisions facilitated by short-range repulsive forces.

Chapter 5: Donor Deuteration Effects in Collisional Energy Transfer: Pyrazine-d_4 (E_{vib} = 37900 cm^{-1}) + HCl Collisions

5.1 Introduction

Unexpected isotope effects were seen in the dynamics of collisional relaxation of pyrazine-h_4 (E_{vib}) with HCl and DCl showed as discussed in Chapter 3. The translational temperatures for scattered HCl and DCl molecules in collisional relaxation of pyrazine-h_4 (E_{vib}) have opposite dependence on *J* states of the isotopes. One possible reason for the observed dynamics is that near-resonant energy transfer occurs between HCl (ν_{HCl} = 2886 cm^{-1}) [48] and excited pyrazine-h_4 (ν_{7b} = 3041 cm^{-1}) [49]. The near-resonant pathway is removed when DCl is the collision partner since ν_{DCl} = 2088 cm^{-1} [48]. Deuteration of the pyrazine will shift the C-D frequency to 2274 cm^{-1} and remove the near-resonance [48]. In the work reported in this Chapter, inelastic collisions of highly excited pyrazine-d_4 (E_{vib} = 37900 cm^{-1}) and thermal HCl are studied to investigate the contributions of near-resonant vibrational energy transfer in pyrazine-h_4 (E_{vib}) + HCl collisions.

Collisional energy transfer calculations of Higgins and Chapman for collisional quenching of pyrazine-h_4 (E_{vib} = 40323 cm^{-1}) and pyrazine-d_4 (E_{vib} = 40323 cm^{-1}) with CO showed isotope effects in the amount of energy transferred to CO in the collisions [82]. Their theoretical studies showed more energy is transferred to CO on average when the collision partner is pyrazine-d_4 (E_{vib}). The isotope effects were attributed to the presence of more low frequency vibrational modes in excited pyrazine-d_4. Collisional relaxation of highly excited polyatomics usually involve

these modes [1, 27, 41, 83-89]. The extent to which the energy transfer dynamics is affected by the availability of low frequency vibrational modes is revealed by studying pyrazine-d_4 (E_{vib}) + HCl collisions.

The presence of a larger number of low-frequency vibrational modes in pyrazine-d_4 (E_{vib}) is due to its larger moment of inertia compared pyrazine-h_4 (E_{vib}). Larger moment of inertia results in smaller energy spacing between its vibrational states and the spacing decreases further with high excitation of its vibrational motion due to vibrational anharmonicity. The energy transfer efficiency of pyrazine-d_4 (E_{vib}) in collisions with HCl should therefore, be increased relative to that for pyrazine-h_4 (E_{vib}) if low-frequency vibrational modes of the energy donor are major players in the collisional energy transfer.

Substantial differences were observed by Stephens and Cool in the V→V energy transfer rates for quenching collisions of vibrationally excited DF and HF with CO_2 [90]. The rate for the excitation of the asymmetric stretch of CO_2 in collisions with DF (v = 1) is nearly 5 times greater than that when the energy donor is HF (v = 1). Stephens and Cool pointed to the greater effectiveness of the coupling of rotational and vibrational (V-R) motions of DF (v = 1) in inelastic collisions as the reason for the rate enhancement. The rates for energy transfer between HCl and pyrazine-d_4 (E_{vib}) should be increased relative to that for HCl and pyrazine-h_4 (E_{vib}) collisions if the dynamics is influenced by V-R coupling.

Collisional relaxation of pyrazine-d_4 (E_{vib}) with HCl by V→RT and V→V pathways have been measured and the results are presented in this Chapter. In the V→RT energy transfer studies, HCl molecules that are scattered in v = 0 state after

inelastic collisions with pyrazine-d_4 (E_{vib}) are probed. In the V→V energy transfer studies, HCl molecules that become vibrationally excited after inelastic collisions with pyrazine-d_4 (E_{vib}) are probed. The V→RT and V→V data for pyrazine-d_4 (E_{vib}) + HCl collisions are compared to those for pyrazine-h_4 (E_{vib}) + HCl collisions in order to see if near-resonance effects are contributing factors to the mechanistic differences observed in collisional relaxation of pyrazine-h_4 (E_{vib}) with HCl and DCl. Comparison of the collisional relaxation data for pyrazine-d_4 (E_{vib}) and pyrazine-h_4 (E_{vib}) will also reveal the contributions of low frequency vibrational modes to the collision dynamics.

5.2 Experimental Methods

The experimental details of the collisional energy transfer are described in Chapter 2 and the specifics pertaining to this study are described here. Excited gas-phase pyrazine-d_4 molecules were prepared by excitation with the quadrupled output of a pulsed Nd:YAG laser (λ = 266 nm). A 1:1 mixture of pyrazine-d_4 and HCl gases was flowed through a 3-m collision cell at a total pressure of ~20 mTorr (or less) for the V→RT energy transfer studies. The total pressure for the V→V energy transfer studies was ≤ 40 mTorr. Energy transfer between excited pyrazine and HCl was probed by collecting transient IR signals for individual *J* states of scattered HCl (v = 0) molecules. The probe transitions are mainly the R-branch lines for $H^{35}Cl$. The R5 transition of $H^{37}Cl$ is measured instead of that for $H^{35}Cl$ because the quality of the OPO mode was better at the former transition. Energy transfer measurements made using transitions for $H^{35}Cl$ and $H^{37}Cl$ yield comparable results. The R-branch transitions used for the V→RT energy transfer studies are listed in Table 5.1.

TABLE 5.1: IR Probe Transitions for Rotational States of HCl[a]

$H^{35}Cl$ (v = 0, J) + hν ($\lambda \sim 3.3\ \mu$m) → $H^{35}Cl$ (v = 1, J + 1)			
J	ν_0 (cm^{-1})[b]	E_{rot} (cm^{-1})[c]	S_J (cm $molecule^{-1}$)[d]
0	2906.2468	0.0000	2.367×10^{-19}
1	2925.8967	20.8782	4.194×10^{-19}
2	2944.9138	62.6219	5.034×10^{-19}
3	2963.2861	125.2057	4.852×10^{-19}
4	2981.0017	208.5917	3.960×10^{-19}
5[e]	2995.7848	312.2602	8.962×10^{-20}
6	3014.4166	437.5556	1.745×10^{-19}
7	3030.0934	582.9947	9.616×10^{-20}
8	3045.0686	748.9588	4.719×10^{-20}
9	3059.3314	935.3474	2.070×10^{-20}
10	3072.8716	1142.0480	8.140×10^{-21}
11	3085.6791	1368.9358	2.876×10^{-21}
12	3097.7442	1615.8741	9.146×10^{-22}
13	3109.0575	1882.7142	2.623×10^{-22}

[abcd] Listed quantities are from the HITRAN database [73] and are as defined in Table 3.1. [e] The R5 line of $H^{37}Cl$ was measured instead of that for $H^{35}Cl$ because the OPO-mode quality at the former transition was better.

Transient IR signals were collected as described in Chapter 2. The OPO was modulated and stabilized using active feedback control. The OPO output was locked to line center frequency ν_0 of a HCl ro-vibrational transition for measurements of population changes at ν_0. Measurements of nascent Doppler-broadened line profiles were done by locking the OPO output to a single fringe of a Fabry-Perot etalon. A

pulse generator adjusted the timing of the 266 nm pulse to occur at the same time as IR frequency being measured.

5.3 Results and Discussion: HCl (v = 0) collision products

The state-resolved data for pyrazine-d_4 (E_{vib}) + HCl single collisions that produce scattered HCl (v = 0) molecules are reported in this section. The nascent Doppler-broadened line profiles for individual *J* states of scattered HCl are presented and translational energy changes of the scattered collision products are discussed in light of these line profiles. The nascent rotational distribution for the scattered bath molecules is presented, along with the accompanying changes in angular momenta and recoil velocities. The *J*-specific rate constants for population changes of HCl due to energy transfer are also reported. The data for pyrazine-d_4 (E_{vib}) + HCl collisions are compared to those for pyrazine-h_4 (E_{vib}) + HCl collisions (Chapter 3) to illustrate how deuteration of the energy donor affects the dynamics for vibration-to-rotation and translation (V→RT) energy transfer.

5.3.1 Transient IR Measurements for HCl (v = 0) Collision Products

Single collisions between excited pyrazine-d_4 and thermal HCl molecules lead to population changes of individual *J* states of HCl. The low-*J* states of HCl ($J \leq 5$) have significant population at 300 K and inelastic collisions between HCl and pyrazine-d_4 (E_{vib}) lead to net depletion of molecules for these *J* states. On the other hand, high-*J* states of HCl ($J \geq 6$) do not have substantial population at 300 K and collisions with excited pyrazine-d_4 lead to net appearance of molecules for these *J*

states. The initial population of states with $J \geq 6$ is small enough that population depletion is not observed.

Examples of transient IR absorption signals collected for low-J states of HCl after single collisions with pyrazine-d_4 (E_{vib}) are shown in Figure 5.1. The decreasing IR absorption signal at IR line center ν_0 in Figure 5.1a represents net depletion of HCl ($J = 5$) population. The increasing IR absorption signal in Figure 5.1b shows net appearance of HCl ($J = 5$) population with the IR light tuned 0.003 cm^{-1} away from ν_0. Transient IR signals for HCl ($v = 0$, $J = 5$) show depletion at ν_0 and appearance at $\nu_0 \pm 0.003$ cm^{-1}.

Figure 5.2 shows the nascent Doppler-broadened line profile for scattered HCl in $J = 5$ state after collisions with highly vibrationally excited pyrazine-d_4. The line profile shows net depletion at line center and net appearance in the wings of the line profile. The double Gaussian function described by Eq. 3.1 is fit to the line profile data. The double Gaussian function consists of two separate Gaussian functions with one function describing the appearance component of the line profile and the other describing the depletion component. The full width at half maximum for appearance from the fit is used to determine the translational temperature of the recoiling bath molecules as discussed in Chapter 3.

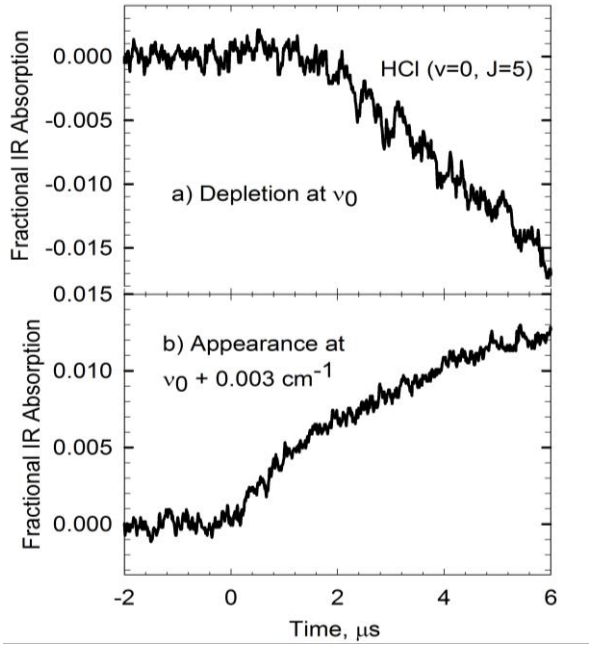

Figure 5.1. Transient IR absorption signals for HCl in (v = 0, J = 5) state after collisions with pyrazine-d_4 (E_{vib} = 37900 cm^{-1}) showing a) depletion of population at line center ν_0 and b) appearance of population 0.003 cm^{-1} away from line center.

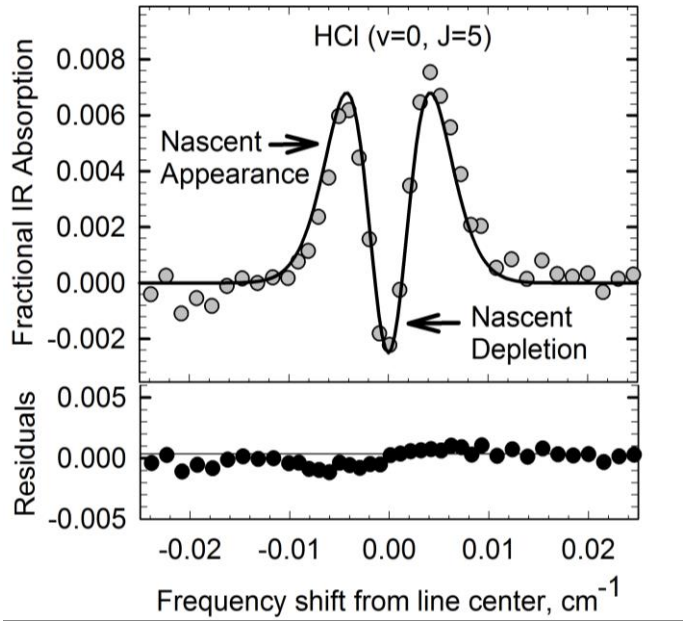

Figure 5.2. Nascent Doppler-broadened line profile (circular data points) for scattered HCl (v = 0, J = 5) population. The line shape shows net depletion of molecules around ν_0 and net appearance away from ν_0. The solid is a double Gaussian fit. Below the line profile are the residuals of the fit.

The two components of the double Gaussian fit to the line profile for HCl (J = 5) are shown in Figure 5.3. The lab-frame translational temperature for appearance

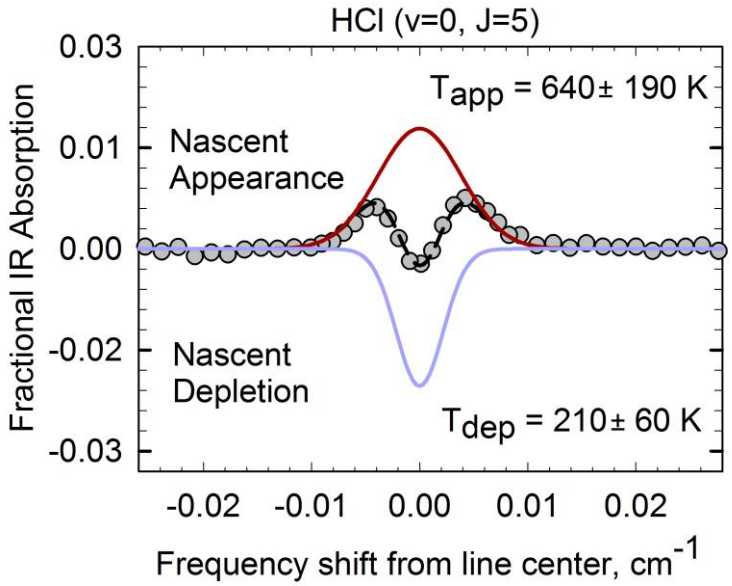

Figure 5.3. The appearance (top curve) and depletion (bottom curve) components of the Doppler-broadened HCl (v = 0, J = 5) line profile. Tapp shows the average translational energy for the appearance population is increased after the inelastic collisions. T_{dep} shows the average translational energy of HCl molecules prior to the inelastic collisions is lower than T = 300 K. Integration of the area under each curve gives the population for each process.

T_{app} is 640 ± 190 K, which is higher than 300 K, and represents an increase in the average translational energy of scattered HCl species in J = 5 state. In contrast, the lab-frame depletion temperature T_{dep} is 210 ± 60 K, which is lower than T = 300 K. This shows that the pre-collision HCl (J = 5) molecules are a colder subset of the initial 300 K distribution. This result suggests that attractive interactions are involved in the energy transfer dynamics.

The Doppler-broadened line profiles measured for the J = 2-5 states of HCl are presented in Figure 5.4. The low-J nascent line shapes show net removal of

population around line center and net appearance of molecules away from line center. Overall, the appearance population increases with *J* while the depletion population

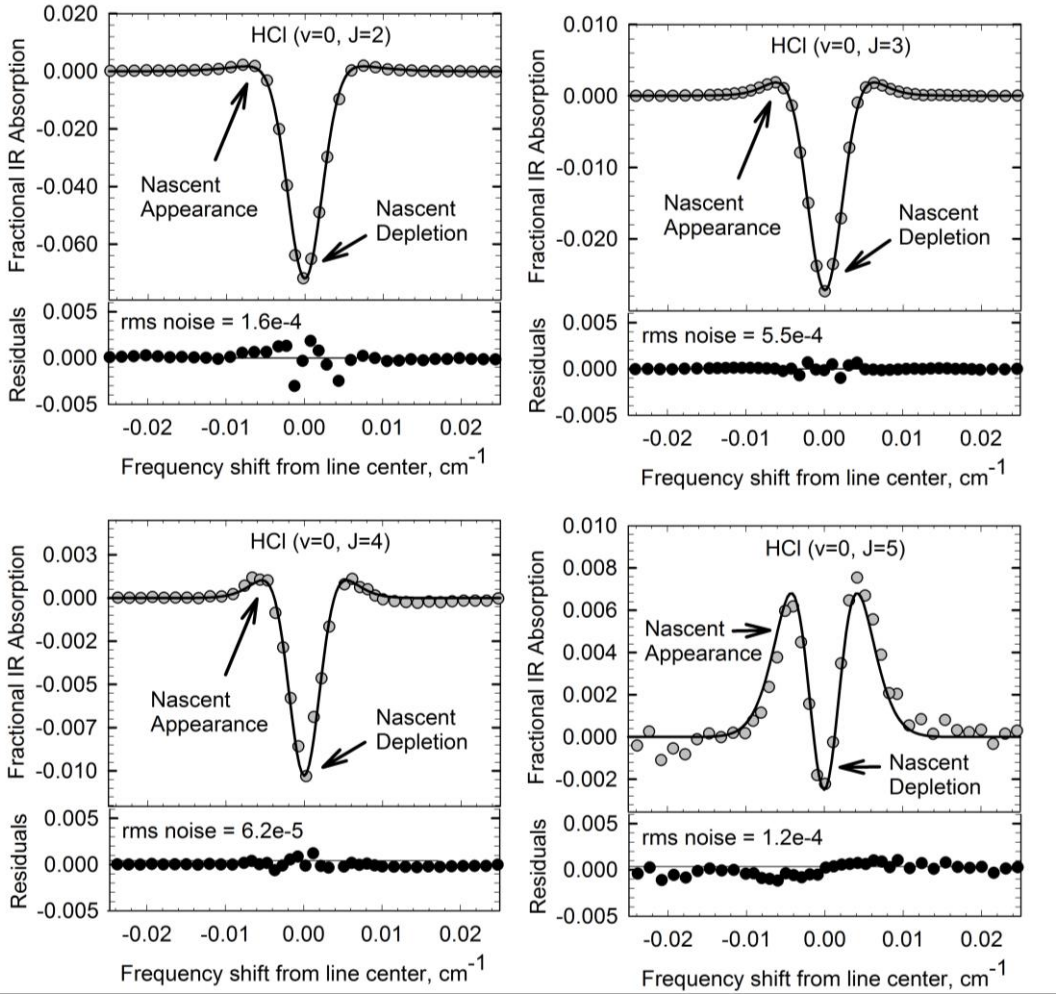

Figure 5.4. Nascent Doppler-broadened line profiles (circular data points) for low-*J* states of scattered HCl. The depletion population decreases with *J* state while the appearance population increases with *J* state. The residuals are plotted below each line profile. Data were collected at t = 1 μs following UV excitation of pyrazine-d_4.

decreases with *J*. The trend seen in the population changes for low-*J* states is due to the Boltzmann rotational distribution of HCl, where the more populated *J* states at T

= 300 K experience a higher decrease in initial population and lower increase in appearance population.

The data in Figure 5.4 reveal that the widths of the appearance line profiles are larger than the widths of the depletion line profiles. The broader widths for the appearance line shapes represent a wider spread in the translational energy distribution of the appearance populations compared to those of the depletion populations. The low root-mean-square (rms) noise of the residuals for each line profile shows the double Gaussian fit is an adequate description of low-*J* line profiles of scattered HCl despite the slight asymmetry seen in $J = 5$ line profile. The source of the asymmetry of the line profiles is not known although attempts were made to minimize it by collecting data at stable IR modes of the OPO and ensuring quality active feedback control of the IR frequency.

The transient line profiles for the HCl collision products in the $J = 7$, 8, 10 and 11 states are shown in Figure 5.5. A single Gaussian function (Eq. 4.2) is fit to the high-*J* line profiles in order to obtain T_{app} of the scattered HCl. The rms noise of the residuals for the line profiles show the single Gaussian fits are good descriptions of the high-*J* line profiles for recoiling HCl molecules and increases the reliability of the T_{app} determined.

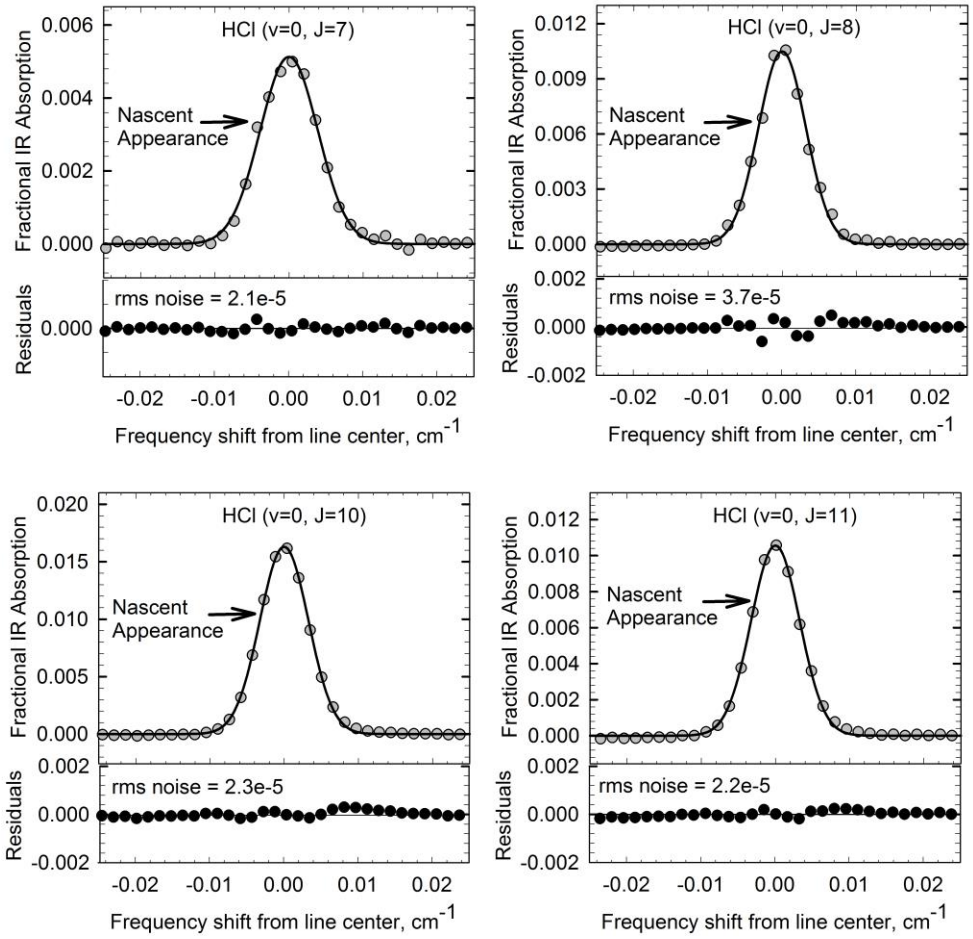

Figure 5.5. Doppler-broadened line profiles for high-*J* states of HCl collision products. The data show net appearance of molecules across the line profiles since these J states have very low population at thermal conditions.

5.3.2 Nascent Translational Temperatures of Recoiling Molecules

The average change in translational energy of the scattered bath molecules is determined from the full width at half maximum (FWHM) of the measured line profiles. For recoiling HCl in low-*J* states, the FWHM of the appearance line profile $\Delta\nu_{app}$ is used to obtain the T_{app}. The initial translational energies are determined from $\Delta\nu_{dep}$ measurements. Listed in Table 5.2 are the FWHM for appearance and depletion

components of the *J*-specific line shapes of HCl collision products. Also listed are the corresponding translational temperatures. The T_{app} values show that HCl molecules are scattered from excited pyrazine-d_4 with gains in translational energy. The translational energy gain of the appearance population decreases with *J* state of HCl. The T_{dep} values are similar for the *J* = 2-5 states, with values that are less than 300 K. The relatively low T_{dep} values show that colder HCl molecules preferentially undergo collisions with pyrazine-d_4 (E_{vib}).

TABLE 5.2: *J*-resolved Doppler-broadened FWHM and translational temperatures of nascent population of HCl scattered in collisions with pyrazine-d4 (E_{vib})

	appearance of scattered HCl		depletion of 300 K HCl	
J state	$\Delta\nu_{app}$ (cm^{-1})[a]	T_{app} (K)[b]	$\Delta\nu_{dep}$ (cm^{-1})[a]	T_{dep} (K)[b]
2	0.014	1610 ± 480	0.0051	210 ± 60
3	0.012	1170 ± 350	0.0052	220 ± 60
4	0.010	800 ± 240	0.0058	270 ± 70
5	0.0090	640 ± 190	0.0052	210 ± 60
7	0.0089	610 ± 180	-	-
8	0.0084	540 ± 160	-	-
10	0.0078	460 ± 140	-	-
11	0.0077	440 ± 130	-	-
13	0.0077	440 ± 130	-	-

[a] The full width at half maximum (FWHM) for depletion $\Delta\nu_{dep}$ and appearance $\Delta\nu_{app}$ components of a line profile of scattered HCl. [b] The lab-frame translational temperature for depletion T_{dep} and appearance T_{app} of HCl collision products. The calculations for T_{app} are in the Appendix.

The center-of-mass (COM) frame translational temperatures T_{rel} of the scattered molecules are the translational energy of both HCl and excited pyrazine-d_4 after collisional energy transfer. Figure 5.6 shows the *J*-dependence of T_{rel}. The plot

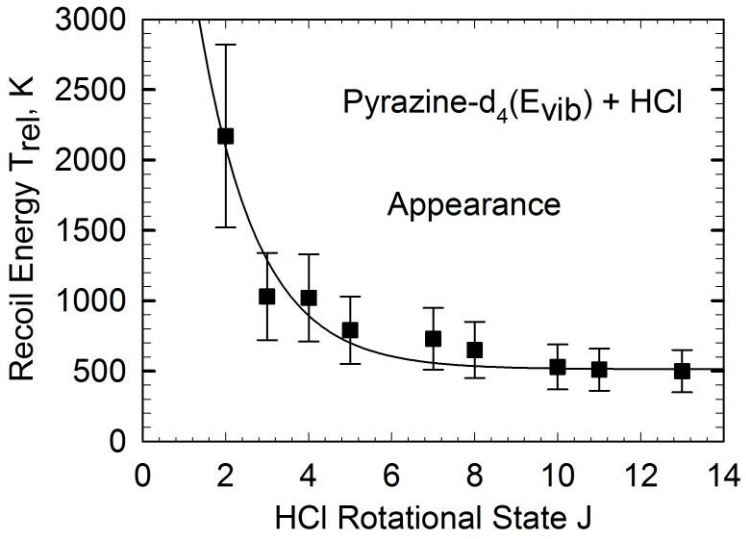

Figure 5.6. Center-of-mass frame translational temperatures T_{rel} (square data points) for appearance of scattered HCl population in individual *J* states. The solid line is an exponential fit to the data. An inverse correlation is seen between T_{rel} and *J* states of HCl. The COM translational temperatures are obtained by $T_{rel} = T_{lab} + (m_{HCl}/ m_{pyz})(T_{lab} - T)$, where m_{pyz} is the mass of pyrazine and T is ambient temperature (300 K). Other quantities are as defined in Table 5.2.

shows T_{rel} is higher than T = 300 K for all *J* states and that T_{rel} decreases exponentially with *J* state. A similar trend between T_{rel} and *J* is seen in V→RT energy transfer collisions of HCl + pyrazine-h_4 (E_{vib}) as shown in Figure 3.7. The T_{rel} values for HCl + pyrazine-d_4 (E_{vib}) collisions are slightly higher than those measured for collisions of HCl + pyrazine-h_4 (E_{vib}). Figure 5.7 compares V→RT scattering data for both energy donors with HCl and for pyrazine-h_4 (E_{vib}) with DCl. The small

increase in T_{rel} values for HCl/pyrazine-d_4 is a result of more low-frequency vibrational modes with excited pyrazine-d_4. Collisional energy transfer in a number of studies has been found to involve low-frequency vibrational modes of the energy donor. The similarity in the *J*-dependence for HCl scattering with pyrazine-d_4 (E_{vib}) and pyrazine-h_4 (E_{vib}) shows that similar energy transfer mechanisms are operative for

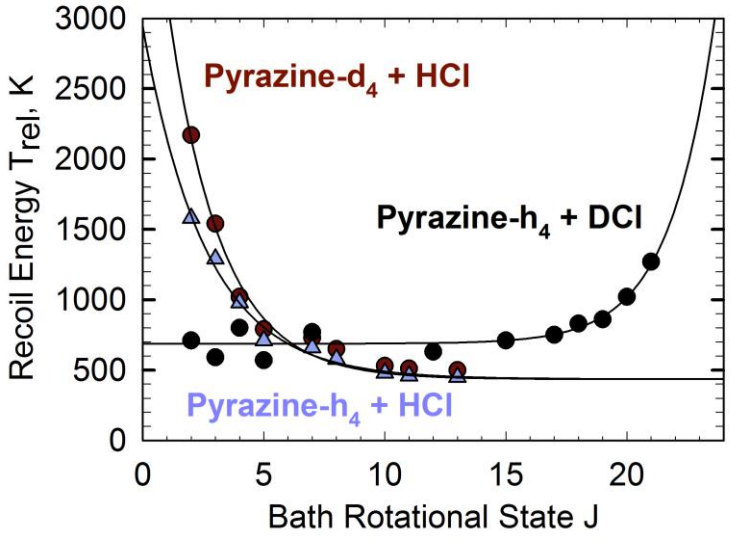

Figure 5.7. T_{rel} (values) show similar bath *J*-dependence for collisions of HCl with pyrazine-d_4 (E_{vib}) and pyrazine-h_4 (E_{vib}). The *J*-dependence of T_{rel} for DCl with pyrazine-h_4 (E_{vib}) shows very different behavior.

both collision systems. The opposite trend seen for DCl + pyrazine-h_4 (E_{vib}) collisions indicates the energy transfer mechanism is strongly affected by deuteration of the energy acceptor than the energy donor.

Figure 5.7 suggests an energy transfer mechanism for HCl that is mediated by anisotropic attractive interactions, where the energy donor collides preferentially with either the H-end or Cl-end of HCl as discussed in Chapter 3. Since the center-of-mass

of HCl molecules lies closer to Cl, collisions between the energy donors and the H-end of HCl leads to large changes in rotational motion of HCl and small changes in translational motion. Collisions with the Cl-end result in large changes in the translational motion of HCl and small changes in its rotational motion. In contrast, the data for DCl + pyrazine-h_4 (E_{vib}) collisions show no evidence of oriented collisions since large changes in rotational motion of scattered DCl are accompanied by large changes in its translational motion.

The T_{rel} values for collisional quenching of pyrazine-d_4 (E_{vib}) and pyrazine-h_4 (E_{vib}) with HCl are similar, which suggests involvement of similar vibrational frequencies of the isotopic energy donors in the inelastic collisions. Excitation of the energy donors to high vibrational levels accesses more anharmonic vibrational states, especially for low frequency modes. The vibrational frequencies of a number of vibrational modes of pyrazine-h_4 and pyrazine-d_4 are compared in Table 5.3. Several low frequency modes of pyrazine-h_4 and pyrazine-d_4 are close enough that anharmonic effects might lead to similar vibrational transitions in pyrazine-d_4 (E_{vib}) and pyrazine-h_4 (E_{vib}) and result in similar T_{rel} values for inelastic collisions with HCl. Figure 3.14 shows that a large portion of the vibrational energy content of pyrazine-h_4 (E_{vib}) is in the low frequency modes, which makes it likely that energy is transferred from these modes.

TABLE 5.3: Vibrational frequencies of pyrazine-h_4 and pyrazine-d_4 at 300 K[a]

mode	Pyrazine-h_4[b]	Pyrazine-d_4[b]
ν_{16b}	416	399
ν_{6a}	596.1	586
ν_4	703	678
ν_{10a}	757	580
ν_{11}	804	612
ν_5	918.6	721.1
ν_1	1015	882.5
ν_{15}	1022	867
ν_{14}	1067	1028
ν_{12}	1110	840
ν_{18a}	1144	1110
ν_{9a}	1230	1005.6
ν_{19b}	1418	1175
ν_{19a}	1484	1370
ν_{8b}	1524	1505
ν_{8a}	1578	1536
ν_{7b}	3041	2274
ν_2	3054	2274
ν_{13}	3066	2290
ν_{20b}	3066	2290

[a] Data is from IR and Raman spectra of pyrazine-h_4 and pyrazine-d_4 [49]. [b] Frequency values are in cm^{-1}. Vibrational modes not included in the list are either too weak to be measured or could not be accurately assigned.

5.3.3 Angular Momentum Changes and Recoil Velocities of scattered HCl

Molecular collisions are accompanied by changes in angular momentum $\Delta\mathbf{J}$ and recoil velocity. Conservation of angular momentum in collisions requires $\Delta\mathbf{J}_{donor} + \Delta\mathbf{J}_{bath} + \Delta\mathbf{L} = 0$**,** where $\Delta\mathbf{J}_{donor}$ is the change in rotational angular momentum of excited pyrazine-d_4, $\Delta\mathbf{J}_{bath}$ is the change in rotational angular momentum of HCl and $\Delta\mathbf{L}$ is the change in orbital angular momentum of the scattered collision partners. The

expression $\Delta\mathbf{J}_{bath} + \Delta\mathbf{J}_{donor} = -\Delta\mathbf{L} = -\mathbf{b}\mu\Delta\mathbf{v}_{rel}$ is obtained by assuming the same direction for $\Delta\mathbf{J}_{bath}$ and $\Delta\mathbf{J}_{donor}$ as described by Waclawik and Lawrance for the collisional relaxation of excited benzene [75]. Here, **b** is the impact parameter, μ is the reduced mass of HCl and pyrazine-d_4 (E_{vib}) and $\Delta\mathbf{v}_{rel}$ is the change in COM recoil velocity of scattered HCl and pyrazine-d_4 (E_{vib}).

Table 5.4 shows the average change in rotational angular momentum $\langle\Delta\mathbf{J}_{bath}\rangle$ of scattered HCl in final *J* states and the corresponding average change in COM recoil velocity $\langle\Delta\mathbf{v}_{rel}\rangle$ for a number of HCl studies. The changes in rotational angular momentum of recoiling HCl are determined from the difference in magnitudes of the average rotational angular momentum of HCl at T = 300 K and the final rotational angular momentum of the scattered HCl. HCl molecules are scattered in final *J* states with as much as $\langle\Delta\mathbf{J}_{bath}\rangle = 12.5$ and $\langle\Delta\mathbf{v}_{rel}\rangle = 923$ m/s. The large $\langle\Delta\mathbf{J}_{bath}\rangle$ and $\langle\Delta\mathbf{v}_{rel}\rangle$ values are indicative of the impulsive nature of the energy transfer between

TABLE 5.4: Changes in rotational angular momentum and recoil velocities for individual *J* states of scattered HCl (v = 0) molecules

final *J* state	$\langle \Delta \mathbf{J}_{bath} \rangle^a$	$\Delta \nu_{app}{}^b$	$\langle \mathbf{v}_{lab} \rangle^c$ (m/s)	$\langle \mathbf{v}_{rel} \rangle^d$ (m/s)	$\langle \Delta \mathbf{v}_{rel} \rangle^e$ (m/s)
2	2.8	0.014	1049	1462	923
3	1.7	0.012	895	1232	694
4	2.1	0.010	740	999	461
5	3.6	0.0090	662	880	341
7	6.1	0.0089	646	855	317
8	7.2	0.0084	608	796	257
10	9.4	0.0078	561	722	183
11	10.5	0.0077	549	702	163
13	12.5	0.0077	549	702	163

[a] The average change in rotational angular momentum for scattered HCl (v = 1) molecules. [b] The *J*-dependent FWHM for appearance of HCl population. [c] The average lab-frame recoil velocity of HCl. [d] The average COM recoil velocity of scattered HCl and pyrazine-d_4 (E_{vib}). [e] The average change in $\mathbf{v}_{rel}$. The calculations for determining $\langle \mathbf{v}_{lab} \rangle$, $\langle \mathbf{v}_{lab} \rangle$ and $\langle \Delta \mathbf{v}_{rel} \rangle$ are presented in the Appendix.

pyrazine-d_4 (E_{vib}) and HCl. The bath collision products with small $\langle \Delta \mathbf{J}_{bath} \rangle$ experience large $\langle \Delta \mathbf{v}_{rel} \rangle$ while those with large $\langle \Delta \mathbf{J}_{bath} \rangle$ have small changes in $\langle \Delta \mathbf{v}_{rel} \rangle$. The inverse correlation between $\langle \Delta \mathbf{J}_{bath} \rangle$ and $\langle \Delta \mathbf{v}_{rel} \rangle$ for HCl + pyrazine-d_4 (E_{vib}) collisions supports an oriented interaction of the collision partners during the energy transfer. An inverse correlation between $\langle \Delta \mathbf{J}_{bath} \rangle$ and $\langle \Delta \mathbf{v}_{rel} \rangle$ is also seen for HCl + pyrazine-h_4 collisions (Figure 3.10), which further shows the collision dynamics is not as strongly affected with deuteration of the energy donor as it is with deuteration of the energy acceptor.

5.3.4 Nascent Rotational Distribution of Scattered HCl (v = 0) Molecules

The rotational distribution of HCl (v = 0) molecules after single collisions with excited pyrazine-d_4 has been measured. A Boltzmann analysis of the distribution is shown as a semi-log plot in Figure 5.8. The data is obtained by collecting transient IR signals at line center of final *J* states of scattered HCl and combining the IR signals

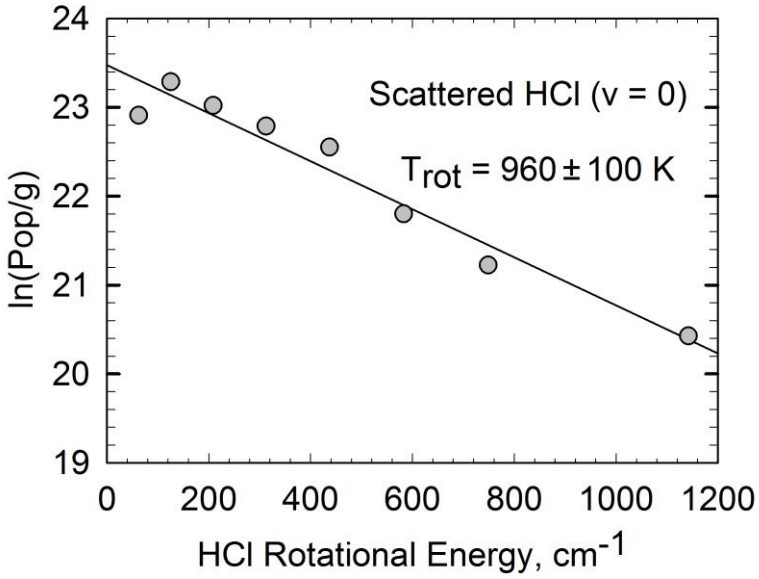

Figure 5.8. Rotational distribution of scattered HCl (v = 0) molecules after nascent collisions with pyrazine-d_4 (E_{vib}). The rotational temperature T_{rot} shows scattered HCl species gain rotational energy on average from the inelastic collisions.

with the nascent Doppler-broadened line profile measurements for the final *J* states. Transient IR signals for each *J* state are measured in pair with a reference state (*J* = 8) in order to account for any experimental fluctuations. The rotational temperature of the recoiling bath molecules T_{rot} is related to the population in individual *J* states pop (*J*) as shown in Eq. 3.2. The rotational temperature of T_{rot} = 960 ± 100 K is higher

than T = 300 K and shows that HCl molecules gain rotational energy from single collisions with pyrazine-d_4 (E_{vib}). The T_{rot} value for HCl + pyrazine-d_4 (E_{vib}) collisions is a little higher than for HCl + pyrazine-h_4 (E_{vib}) collisions (T_{rot} = 890 ± 90 K, Figure 3.11), which demonstrates that pyrazine-d_4 (E_{vib}) imparts slightly larger amounts of energy than does pyrazine-h_4 (E_{vib}).

5.3.5 *J*-specific Rate Constants for V→RT Energy Transfer Channel

The rate constants for the production of scattered HCl (v = 0) molecules in individual *J* states are measured for collisions of pyrazine-d_4 (E_{vib}) and HCl (300 K). The chemical equation for the energy transfer is given in Eq. 5.1.

$$\text{pyz-d}_4(E_{vib}) + \text{HCl}(300\,\text{K}) \xrightarrow{k^J_{app}} \text{pyz-d}_4(E') + \text{HCl}(v = 0, J, \text{Vel}) \quad \text{(Eq. 5.1)}$$

Here, pyz-d_4 (E_{vib}) is excited pyrazine-d_4 prior to collisions with HCl, k^J_{app} is the *J*-specific rate constant for appearance of HCl population, pyz-d_4 (E') is excited pyrazine-d_4 after energy transfer and Vel is the recoil velocity of scattered HCl. The rate equation for appearance of scattered HCl species in individual *J* states is given in Eq. 5.2.

$$\frac{d[\text{HCl}(J)]}{dt} = k^J_{app}\,[\text{pyz-d}_4(E_{vib})][\text{HCl}(300\,\text{K})] \quad \text{(Eq. 5.2)}$$

Integration of Eq. 5.2 is done using the method of initial rates, where the changes in concentrations of the collision partners are negligible at short times. The integrated rate equation is rearranged in Eq. 5.3 to give the appearance rate constant.

$$k^J_{app} = \frac{\Delta[\text{HCl}(J)]}{\Delta t}\,\frac{1}{[\text{pyz-d}_4(E_{vib})]_0[\text{HCl}(300\,\text{K})]_0} \quad \text{(Eq. 5.3)}$$

Here, [pyz-d_4 (E_{vib})]$_0$ and [HCl (300 K)]$_0$ are the initial concentrations of excited pyrazine-d_4 and HCl respectively. The concentration of pyrazine-d_4 (E_{vib}) is determined from UV absorption measurements and the interaction volume of the collision partners. The details of the calculation are presented in the Appendix.

The k^J_{app} values for appearance of HCl (J = 8) population is measured directly and the measurement is combined with the measured T_{rot} as shown in Eq. 3.6 to obtain the k^J_{app} values listed in Table 5.5 for other J states of scattered HCl. The total appearance rate constant k_{app} for V→RT energy transfer of HCl and pyrazine-d_4 (E_{vib})

TABLE 5.5: Rate Constants for Nascent Appearance of HCl (v = 0, J) after Collisions with Pyrazine-d_4 (E_{vib} = 37900 cm^{-1})

J	E_{rot} (cm^{-1})	k^J_{app} (10^{-12} cm^3 molecule^{-1} s^{-1})
2	62.6219	56 ± 20
3	125.2057	71 ± 25
4	208.5917	81 ± 28
5	312.7294	84 ± 30
7	582.9947	77 ± 27
8	748.9588	68 ± 24
10	1142.0480	46 ± 16
11	1368.9358	36 ± 13
13	1882.7142	20 ± 7
$k_{app} = \sum k^J_{app}$		(7.9 ± 2.8) × 10^{-10} cm^3 molecule^{-1} s^{-1} *a*
k_{app} (with pyz-h_4 (E_{vib}))		(6.4 ± 1.9) × 10^{-10} cm^3 molecule^{-1} s^{-1} *b*

The J-specific absolute rate constants for appearance of HCl molecules in V→RT relaxation of pyrazine-d_4 (E_{vib}). *a* The total appearance rate constant for scattered HCl in V→RT relaxation of pyrazine-d_4 (E_{vib}) *b* The total appearance rate constant for scattered HCl in V→RT relaxation of pyrazine-h_4 (E_{vib}). The lower k_{app} for relaxation of pyrazine-h_4 (E_{vib}) highlights the effectiveness of pyrazine-d_4 (E_{vib}) in transferring energy in inelastic collisions.

is a little larger than for HCl and pyrazine-h_4 (E_{vib}) collisions (k_{app} = (6.4 ± 1.9) × 10^{-10} cm^3 $molecule^{-1}$ s^{-1}), which shows enhancement in the rate of energy transfer with deuteration of the energy donor.

The rate constants for depletion of initial HCl population in inelastic collisions of pyrazine-d_4 (E_{vib}) and 300 K HCl are determined from integration of the depletion line profiles for low-*J* states of scattered HCl. The measurements are used to confirm the V→RT energy transfer rates determined with appearance rate constants. The chemical expression for removal of 300 K HCl population in individual *J* states is given in Eq. 5.4.

$$\text{pyz-d}_4(E_{vib}) + \text{HCl}(J, 300\,\text{K}) \xrightarrow{k_{dep}} \text{pyz-d}_4(E') + \text{HCl}(v = 0, J', \text{Vel}) \quad \text{(Eq. 5.4)}$$

Here, *J* is the rotational state of pre-collision HCl molecules, k_{dep} is the depletion rate constant and *J′* is the final rotational state of the bath molecules after the inelastic collisions. The rate for depletion of *J*-specific HCl population is shown in Eq. 5.5.

$$-\frac{d[\text{HCl}(J)]}{dt} = k_{dep}\,[\text{HCl}(J, 300\,\text{K})][\text{pyz-d}_4(E_{vib})] \quad \text{(Eq. 5.5)}$$

Here, [HCl(*J*)] is the concentration of the population removed from state *J* and [HCl(*J*, 300 K)] is the concentration of the initial HCl population for that *J* state. The depletion rate constant k_{dep} is listed in Table 5.6 for low *J* states of HCl. The

TABLE 5.6: Rate constants for depletion of HCl (v = 0, J) population in collisions with Pyrazine-d_4 (E = 37900 cm^{-1})

J	E_{rot} (cm^{-1})	k^J_{dep} (10^{-10} cm^3 $molecule^{-1}$ s^{-1})
2	62.6219	10.0
3	125.2057	6.9
4	208.5917	7.3
5	312.2602	9.1
$\langle k_{dep} \rangle$ =		$(8.3 \pm 3.3) \times 10^{-10}$ cm^3 $molecule^{-1}$ s^{-1} [a]
k_{app}		$(7.9 \pm 2.8) \times 10^{-10}$ cm^3 $molecule^{-1}$ s^{-1}

The rate constant for depletion of initial HCl population in low J states due to collisions with vibrationally hot pyrazine-d_4. [a] The weighted average depletion rate constant. The weighted depletion rate constant is very similar to k_{app}, which confirms the V→RT rate determined with the appearance rate constants.

population-weighted average depletion rate constant $\langle k_{dep} \rangle$ is $(8.3 \pm 3.3) \times 10^{-10}$ cm^3 $molecule^{-1}$ s^{-1}, which is very comparable to the k_{app} for HCl + pyrazine-d_4 (E_{vib}) collisions. The similarity in the values of $\langle k_{dep} \rangle$ and k_{app} confirms the V→RT energy transfer rate determined with the appearance rate constants. The slightly larger uncertainty for $\langle k_{dep} \rangle$ compared to that for k_{app} is a result of a wider spread in the uncertainty in the parameters from the double Gaussian fitting. The $\langle k_{dep} \rangle$ value for HCl + pyrazine-d_4 (E_{vib}) collisions is close to that for HCl + pyrazine-h_4 (E_{vib}) collisions ($\langle k_{dep} \rangle$ is $(8.4 \pm 3.4) \times 10^{-10}$ cm^3 $molecule^{-1}$ s^{-1}), which provides additional support for the similarity of mechanisms for pyrazine-d_4 (E_{vib}) and pyrazine-h_4 (E_{vib}).

5.3.6 Energy Transfer Probability Distribution Function $P(\Delta E)$

The dependence of the energy transfer data on J states of scattered HCl has been converted to dependence on the amount of energy transferred ΔE from excited pyrazine-d_4. The J-specific energy transfer probability distribution function $P_J(\Delta E)$

gives the translational energy distribution for individual *J* states of HCl collision products. The quantities utilized in obtaining the distribution are described in section 3.3.6. The $P_J(\Delta E)$ are summed in Eq. 3.14 to give the total energy transfer probability distribution $P(\Delta E)$.

The $P(\Delta E)$ function accounts for all V→RT energy transfer events and is plotted for HCl and pyrazine-d_4 (E_{vib}) collisions in Figure 5.9. The probability with positive ΔE values is much greater than that with negative ΔE values, which confirms

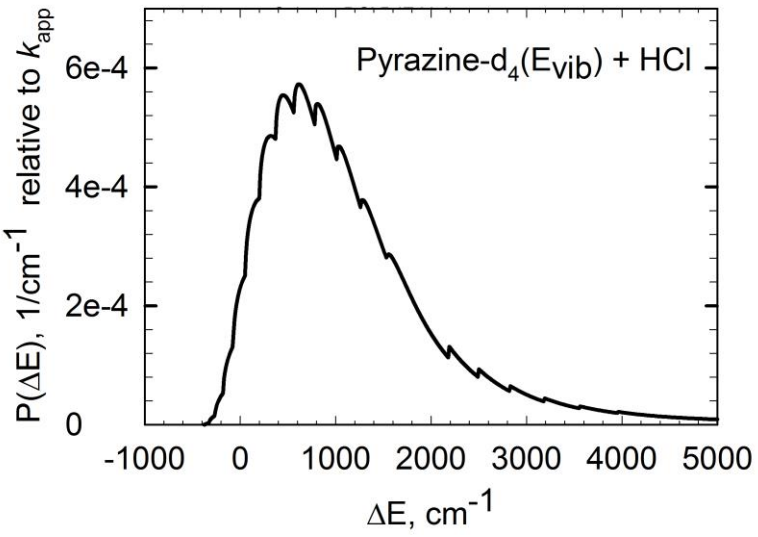

Figure 5.9. The energy transfer probability distribution for V→RT energy transfer collisions of HCl and pyrazine-d_4 (E_{vib}). The distribution shows that HCl is more likely to gain than loose energy from the inelastic collisions.

the scattered bath molecules are more likely to gain energy in collisions with excited pyrazine-d_4 (E_{vib}). Approximately 93% of the energy transfer has $\Delta E \leq 3000$ cm^{-1}, which is roughly equal to a single quantum change in C-H stretch for pyrazine-h_4 (Table 5.3). The $P(\Delta E)$ curve for HCl + pyrazine-d_4 (E_{vib}) collisions is compared to

that for HCl + pyrazine-h_4 (E_{vib}) in Figure 5.10. Overall, the two distributions have comparable probabilities for several ΔE values, which shows similar mechanism for collisional energy transfer. The average energy transferred in HCl + pyrazine-d_4 (E_{vib}) collisions is $\langle \Delta E \rangle$ = 1300 cm^{-1}, which is higher than for HCl + pyrazine-h_4 (E_{vib}) collisions ($\langle \Delta E \rangle$ = 1140 cm^{-1}). The larger $\langle \Delta E \rangle$ for pyrazine-d_4 (E_{vib}) results from larger $P(\Delta E)$ values at $\Delta E \geq 2190$ cm^{-1}. The similarity in the $P(\Delta E)$ curves for

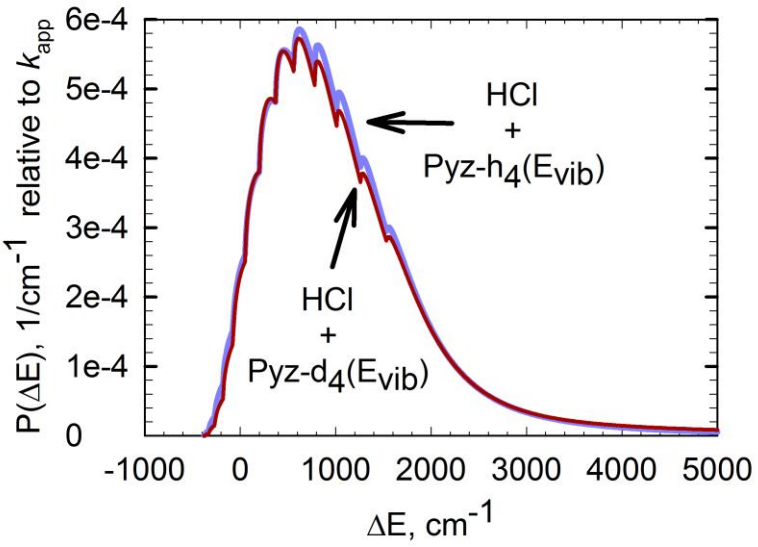

Figure 5.10. The $P(\Delta E)$ curves for collisional relaxation of pyrazine-d_4 (E_{vib}) and pyrazine-h_4 (E_{vib}) with HCl. The similarity in the curves shows a similar mechanism.

pyrazine-d_4 (E_{vib}) and pyrazine-h_4 (E_{vib}) suggests near-resonance effects are not key factors in the isotope effects observed for collisions of pyrazine-h_4 (E_{vib}) with HCl and DCl.

5.4 Results and Discussion: Scattered HCl (v = 1) molecules

Collisional energy transfer between 300 K HCl and pyrazine-d_4 (E_{vib}) that lead to vibrational excitation in HCl has been studied and the state-resolve data are reported in this section. The data include nascent Doppler-broadened line profiles measured for scattered HCl (v = 1, *J*) molecules, the rotational distribution of the vibrationally excited bath molecules and *J*-specific energy transfer rate constants. The vibration-to-vibration (V→V) energy transfer data for HCl + pyrazine-d_4 (E_{vib}) collisions are compared to the V→RT energy transfer data to identify any differences in the collision dynamics.

5.4.1 Transient IR Absorption of Scattered HCl (v = 1) Molecules

Transient IR signals have been collected for HCl molecules in the v = 1 state following single collisions with pyrazine-d_4 (E_{vib}). The transient IR signal for *J* = 2 is shown in Figure 5.11. The signal is collected at line center of the R2 transition using

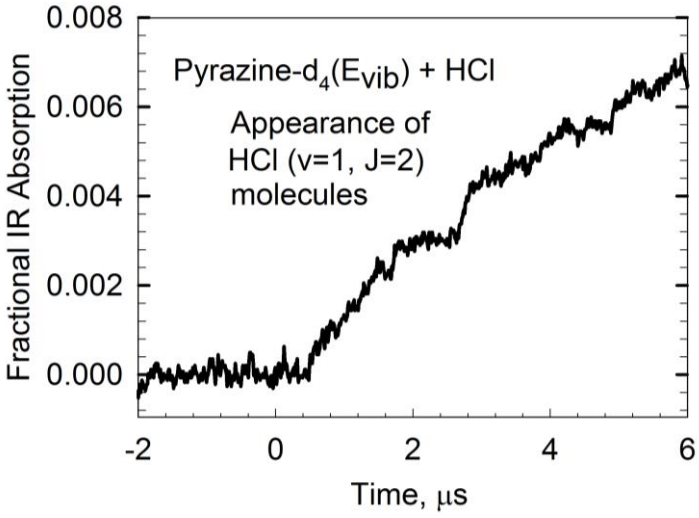

Figure 5.11. Transient IR signal collected for scattered HCl (v = 1, *J* = 2) molecules in collisional relaxation of pyrazine-d_4 (E_{vib}).

the v = 1→v = 2 band. The transient signal shows appearance of scattered HCl (v = 1, J = 2) species after collisions with highly vibrationally excited pyrazine-d_4. The line center ν_0 measurement in Figure 5.1 is an appearance signal since HCl population are essentially in v = 0 state prior to the inelastic collisions. The nascent population of molecules in $J \geq 8$ state is too small to be detected, which shows the V→V energy transfer collisions lead to smaller changes in rotational quanta of the bath molecules than the V→RT pathway.

Figure 5.12 shows nascent Doppler-broadened line profiles measured for several J states of scattered HCl (v = 1) molecules. The positive-going line profiles represent appearance of HCl (v = 1) from inelastic collisions. Each line profile is fit with a single Gaussian function described by Eq. 4.2. The residuals of the fits have low rms noise, showing that the Gaussian fit describes the line profiles well. The full width at half maximum (FWHM) parameter of the fit $\Delta\nu_{app}$ is used to determine the lab-frame translational temperature T_{app} for the scattered HCl (v = 1) molecules. The T_{app} values in Figure 5.12 are slightly larger than 300 K, which shows the vibrationally excited HCl products are scattered in v = 1, with a small increase in their average translational energy.

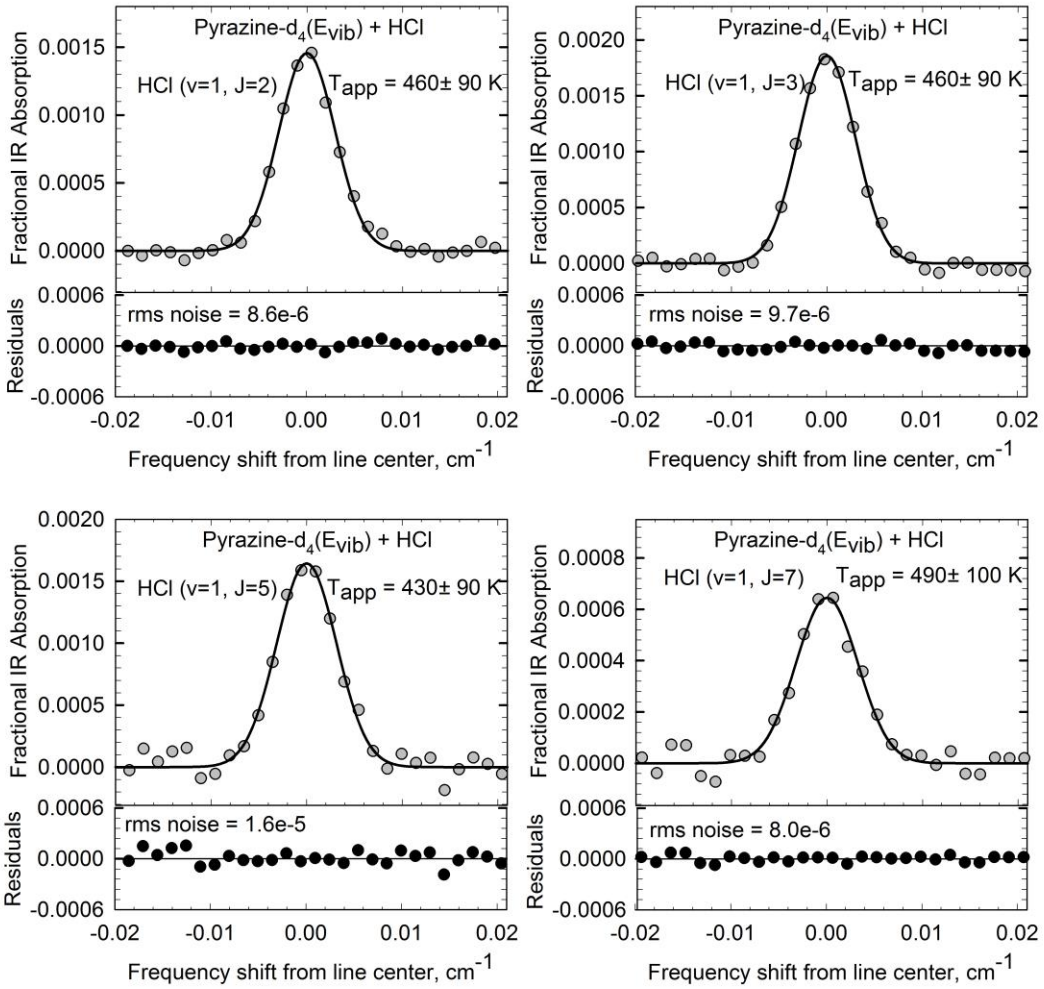

Figure 5.12. The nascent Doppler-broadened line profiles measured for several *J* states of scattered HCl (v = 1) species.

5.4.2 Measurements of Nascent Translational Temperatures for Scattered HCl

The translational temperatures for V→V energy transfer collisions of HCl and pyrazine-d_4 (E_{vib}) have been determined from line profile measurements and are presented in Table 5.7. The translational temperatures in the lab-frame T_{app} and COM

TABLE 5.7: Doppler-broadened FWHM and translational temperatures for V→V relaxation of pyrazine-d_4 (E_{vib}) by HCl.

J state	$\Delta\nu_{app}$ (cm^{-1})[a]	T_{app} (K)[b]	T_{rel} (K)[c]
1	0.0073	480 ± 100	550 ± 110
2	0.0072	460 ± 90	530 ± 110
3	0.0073	460 ± 90	540 ± 110
4	0.0075	480 ± 100	560 ± 110
5	0.0071	430 ± 90	480 ± 100
6	0.0074	460 ± 90	530 ± 110
7	0.0077	490 ± 100	580 ± 120

[a] The full width at half maximum (FWHM) for appearance of HCl (v = 1, *J*) molecules. [b] The appearance lab-frame translational temperature for scattered HCl molecules. [c] The COM translational temperature for the scattered collision partners.

frame T_{rel} reveal HCl molecules gain small amounts of translational energy when they are vibrationally excited in single collisions with the deuterated energy donor. The translational energy gain is relatively constant with *J* state for the HCl (v = 1) collision products. The recoiling bath molecules in v = 1 have $\langle T_{app} \rangle$ = 430-490 K, which is much lower than that for scattered HCl (v = 0) species. The lower $\langle T_{app} \rangle$ for vibrationally excited HCl results from most of the energy transferred in the collision being utilized in the vibrational motion of HCl. The V→V energy transfer is mediated by long-range interactions of the collision partners and such interactions usually lead to small changes in the translational motions of the collision partners after the inelastic collisions.

5.4.3 Changes in Angular Momenta of Recoiling HCl (v = 1)

The changes in rotational angular momenta of HCl $\langle \Delta \mathbf{J}_{bath} \rangle$ and COM recoil velocity $\langle \Delta \mathbf{v}_{rel} \rangle$ that accompany vibrational excitation of HCl in collisions with pyrazine-d_4 (E_{vib}) are recorded in Table 5.8. The $\langle \Delta \mathbf{J}_{bath} \rangle$ values are determined with *J* states of scattered HCl (v = 1) molecules and the average rotational angular momentum of the bath molecule before the inelastic collisions. The $\langle \Delta \mathbf{v}_{rel} \rangle$ are obtained with the initial and final T_{rel} values of the scattered molecules. HCl species emerge from V→V energy transfer collisions with excited pyrazine-d_4 with $\langle \Delta \mathbf{J}_{bath} \rangle$ = 1.7-6.1 and $\langle \Delta \mathbf{v}_{rel} \rangle$ = 153-212 m/s. The small changes in $\langle \Delta \mathbf{J}_{bath} \rangle$ and $\langle \Delta \mathbf{v}_{rel} \rangle$ for V→V energy transfer reflects the long-range nature of the collisions.

TABLE 5.8: *J*-specific changes in rotational angular momentum and recoil velocities for scattered HCl (v = 1) molecules

final *J* state	$\langle \Delta \mathbf{J}_{bath} \rangle^a$	$\Delta \nu_{app}{}^b$	$\langle \mathbf{v}_{lab} \rangle^c$ (m/s)	$\langle \mathbf{v}_{rel} \rangle^d$ (m/s)	$\langle \Delta \mathbf{v}_{rel} \rangle^e$ (m/s)
1	3.3	0.0073	573	741	202
2	2.8	0.0072	561	722	183
3	1.7	0.0073	561	722	183
4	2.1	0.0075	573	741	202
5	3.6	0.0071	542	692	153
6	4.9	0.0074	561	722	183
7	6.1	0.0077	579	750	212

[a] The average change in rotational angular momentum for scattered HCl (v = 1) species. [b] The *J*-specific FWHM for appearance of vibrationally excited HCl. [c] The average lab-frame recoil velocity of HCl. [d] The average COM recoil velocity of scattered HCl and pyrazine-d_4 (E_{vib}). [e] The average change in $\mathbf{v}_{rel}$.

5.4.4 Nascent Rotational Distribution of Scattered HCl (v = 1) Population

The nascent rotational distribution of HCl molecules excited to v = 1 state through collisions with excited pyrazine-d_4 is measured and the data are presented in Figure 5.13 after being analyzed with the Boltzmann rotational distribution function.

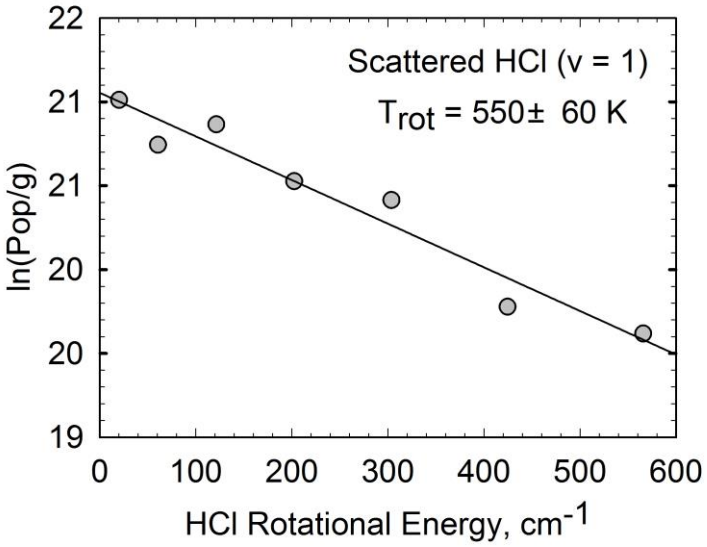

Figure 5.13. Rotational distribution of nascent HCl (v = 1) products after collisions with pyrazine-d_4 (E_{vib}). The T_{rot} shows HCl (v = 1) molecules gain rotational energy from the inelastic collisions.

The rotational temperature T_{rot} for the distribution is determined with the *J*-specific HCl (v = 1) populations as explained by Eq. 3.2. The data reveal that the HCl molecules are scattered with T_{rot} greater than 300 K. This shows that HCl molecules on average gain rotational energy along with vibrational excitation in inelastic collisions. The T_{rot} value for the distribution corresponding to V→V collisional relaxation of pyrazine-d_4 (E_{vib}) is smaller than that for the V→RT channel and the lower value highlights the long-range nature of the collisions leading to V→V energy transfer.

5.4.5 State-Resolved V→V Energy Transfer Rate Constants

The rate constants for collisional quenching of the deuterated energy donor by thermal HCl via V→V energy transfer have been determined for individual *J* states of the scattered energy acceptor. The chemical equation for the inelastic collisions with excited pyrazine-d_4 that lead to scattered HCl (v = 1) population is shown in Eq. 5.6.

$$\text{pyz - d}_4(\text{E}_{\text{vib}}) + \text{HCl}\,(300\,\text{K}) \xrightarrow{k^J_{\text{app}}} \text{pyz - d}_4(\text{E}') + \text{HCl}\,(\text{v} = 1, J, \text{Vel}) \qquad \text{(Eq. 5.6)}$$

The quantities in Eq. 5.6 are as defined by Eq. 5.1. The rate expression for appearance of scattered HCl (v = 1, *J*) molecules is given in Eq. 5.7

$$\frac{\text{d[HCl(v} = 1, J)]}{\text{d}t} = k^J_{\text{app}}\,[\text{pyz - d}_4\,(\text{E}_{\text{vib}})][\text{HCl}\,(300\,\text{K})] \qquad \text{(Eq. 5.7)}$$

where all the terms are as described by Eq. 5.2. The *J*-specific nascent appearance rate constant k^J_{app} for scattered HCl (v = 1) population is obtained by assuming negligible changes in the initial amounts of HCl and excited pyrazine after the inelastic collisions. The V→V energy transfer rate constant is defined in Eq. 5.8.

$$k^J_{\text{app}} = \frac{\Delta[\text{HCl(v} = 1, J)]}{\Delta t}\,\frac{1}{[\text{pyz - d}_4(\text{E}_{\text{vib}})]_0[\text{HCl(300 K)}]_0} \qquad \text{(Eq. 5.8)}$$

The terms in Eq. 5.8 are as defined by Eq. 5.3. The k^J_{app} values for vibrational excitation of HCl are listed in Table 5.8 for *J* = 1-7 states. The rate constants show that most of the scattered population is in *J* = 3-5 states. The presence of a large portion of the population in low-*J* states confirms the propensity of V→V energy transfer events to induce small changes in the rotational quanta of the energy acceptor. The total rate for vibrational excitation of HCl k_{app} (v = 1) is determined by

summing the *J*-specific rate constants. As shown in Table 5.9, k_{app} (v = 1) is only 0.4% of the total rate for collisional relaxation of pyrazine-d_4 (E_{vib}) via V→V and

TABLE 5.9: State-Resolved Rate Constants for Nascent Appearance of HCl (v = 1) after Collisions with Pyrazine (E_{vib} = 37900 cm^{-1})

J	E_{rot} (cm^{-1})	k^J_{app} (10^{-13} cm^3 $molecule^{-1}$ s^{-1})
1	20.2702	2.3 ± 0.2
2	60.7979	3.5 ± 0.3
3	121.5583	4.2 ± 0.4
4	202.5138	4.3 ± 0.4
5	303.6145	4.1 ± 0.4
6	424.7981	3.5 ± 0.3
7	565.9899	2.8 ± 0.3
k_{app} (v = 1) = $\sum k^J_{app}$		(3.1 ± 0.3) × 10^{-12} cm^3 $molecule^{-1}$ s^{-1} [a]
k_{app} (v = 0)		(7.9 ± 2.8) × 10^{-10} cm^3 $molecule^{-1}$ s^{-1} [b]
k^{tot}_{app} = k_{app} (v = 1) + k_{app} (v = 1)		7.9 × 10^{-10} cm^3 $molecule^{-1}$ s^{-1} [c]

The *J*-specific absolute rate constant for the appearance of HCl (v = 1) species due to collisional quenching of excited pyrazine-d_4. [a] The total appearance rate constant for *J* states of HCl (v = 1) molecules. [b] The total appearance rate constant for all *J* states of HCl (v = 0) molecules. [c] The total rate constant for collisional quenching of excited pyrazine-d_4 by HCl. The collision rate for vibrational excitation of HCl shows that such excitation occurs in less than 1 out of 100 single collisions of HCl and excited pyrazine.

V→RT pathways, which shows that V→RT energy transfer is the dominant channel for the collisional energy transfer. The V→RT energy transfer channel also dominates strongly in the energy transfer collisions of HCl and pyrazine-h_4 (E_{vib}), which shows the collisional energy transfer mechanism is not affected significantly by the differences in the frequencies of C-H and C-D vibrational motions of the isotopic energy donors.

5.5 Conclusion

Single collisions of excited pyrazine-d_4 and HCl (at 300 K) lead to energy transfer to the vibrational, rotational and translational degrees of freedom of HCl. Inelastic collisions that result in vibrational excitation to HCl (v = 1) are accompanied by low gains in rotational and translational energy. In contrast, the HCl (v = 0) state is produced with large amounts of rotational and translational energy. The smaller rotational and translational energy changes that accompany V→V energy transfer highlight the long-range nature of the collisions compared to those that occur via V→RT pathway. The data shows V→RT energy transfer dominates in the collisional relaxation since it occurs in over 99 % of HCl + pyrazine-d_4 (E_{vib}) collisions.

The similarities in the dynamics of collisional quenching of pyrazine-d_4 (E_{vib}) and pyrazine-h_4 (E_{vib}) with HCl shows the energy transfer mechanism is not strongly affected by deuteration of energy donor as it is by deuteration of the energy acceptor. Although the collision dynamics of pyrazine-d_4 (E_{vib}) and pyrazine-h_4 (E_{vib}) are similar, the data shows the collisional energy transfer efficiency of pyrazine-d_4 (E_{vib}) is slightly greater and the increase is a result of more low frequency vibrational modes in pyrazine-d_4 (E_{vib}) from which energy can be transferred in the inelastic collisions. Comparison of the data for pyrazine-d_4 (E_{vib}) and pyrazine-h_4 (E_{vib}) also shows near-resonance effects are not contributing significantly to the isotope effects observed in collisional quenching of pyrazine-h_4 (E_{vib}) with HCl and DCl.

Chapter 6: Conclusions and Future Work

6.1 Conclusion

High-resolution transient mid-IR absorption spectroscopy was used in the collisional energy transfer studies presented in the preceding Chapters. A frequency-stabilized CW mid-IR OPO was used to probe the individual *J* states of HCl bath molecules scattered in the inelastic collisions with highly vibrationally excited molecules. Earlier attempts at using a lead-salt diode laser as probe light were unsuccessful since its performance is not optimum at the wavelengths where HCl ro-vibrational lines are located (λ = 3.2-3.4 μm). Moreover, the data collected with OPO have higher signal-to-noise ratios (SNRs) compared to those collected with the diode laser.

In Chapter 3, isotope effects are seen in the dynamics of collisional relaxation of excited pyrazine-h_4 (E_{vib} = 37900 cm^{-1}) with HCl and DCl that proceed via V$\rightarrow$RT energy transfer. HCl and DCl both gain rotational and translational energies from collisions and are scattered with similar rates. However, the *J*-dependence of the translational energy gain of scattered HCl is opposite that of DCl. The HCl collision products in low-*J* states have large translational energy gains while those in high-*J* states have low translational energy gains. In contrast, scattered low-*J* DCl molecules have low translational energy gains while those in high-*J* have high translational energy gains.

The inverse *J*-dependence of the translational energy gain in scattered HCl and DCl shows the V→RT energy transfer with pyrazine-h_4 (E_{vib}) occurs by different mechanisms. The data obtained for HCl + pyrazine-h_4 (E_{vib}) collisions show signs of energy transfer in the presence of strong attractive interactions between the collision partners. In addition, the average energy transfer $\langle \Delta E \rangle$ to HCl is higher than that to DCl due to the larger translational energy gains of its low-*J* state HCl where a sizeable portion of the scattered HCl population is found.

The V→V energy transfer studies presented in Chapter 4 show that the V→V pathway is a minor channel for quenching highly excited pyrazine with HCl and that the relaxation is dominated by V→RT energy transfer. HCl molecules that are vibrationally excited in inelastic collisions with pyrazine-h_4 (E_{vib}) gain modest amounts of rotational and translational energies. The RT energy gains in the V→V pathway are less than for the V→RT pathway. The low rotational and translation energy gains for HCl (v = 1) collision products indicate that this energy transfer is due to long-range interactions of the collision partners. The larger RT energy gain values for scattered HCl (v = 0) indicates that the V→RT energy transfer pathway involves short range impulsive interactions.

As discussed in Chapter 5, the isotope effects due to deuteration of the energy donor are minimal compared to those seen with deuteration of the energy acceptor. HCl molecules are scattered on average with slightly higher rotational and translational energies in collisions with pyrazine-d_4 (E_{vib}) than in collisions with pyrazine-h_4 (E_{vib}). The increased energy transfer efficiency seen with pyrazine-d_4 (E_{vib}) is likely due to the greater number of low frequency vibrational modes in

pyrazine-d_4 (E_{vib}). V→RT energy transfer is the main pathway for collisional relaxation of both pyrazine-d_4 (E_{vib}) and pyrazine-h_4 (E_{vib}) with HCl.

6.2 Future Work

The inverse correlation between T_{rel} and *J* state of scattered HCl seen in V→RT energy transfer collisions of pyrazine-h_4 (E_{vib}) and 300 K HCl indicates the energy transfer is influenced by strong, orienting interactions between the collision partners. The influence of a σ-type interaction on the collision dynamics can be tested by studying collisional energy transfer with a system where such interaction is absent such as HCl + benzene (E_{vib}) system. The excited benzene (E_{vib}) molecules will be prepared by excitation with λ = 248 nm instead of with λ = 266 nm used to excite pyrazine molecules. Alternatively, the collisional relaxation of pyrazine-h_4 (E_{vib}) with CH_4 and CD_4 can be studied to determine the effects of a σ-type interaction on collision dynamics since pyrazine and the methane isotopes do not have such interactions.

One can also test the effect of having two N-sites on pyrazine on collision dynamics by studying collisional relaxation of highly vibrationally excited pyridine-h_5 (C_5H_5N) or pyridine-d_5 (C_5D_5N) with HCl. The influence of the N-containing sites on the donor molecule on the collision dynamics for relaxation of pyrazine-h_4 (E_{vib}) and pyrazine-d_4 (E_{vib}) with HCl may show up as changes in scattering dynamics and/or probabilities for energy transfer of pyridine-h_5 or pyridine-d_5. The effects of quadrupole-dipole interactions of pyrazine with HCl (and DCl) on the energy transfer dynamics can be tested by studying collisional relaxation of highly excited benzene with H_2 (or D_2) using state-resolved methods. For this type of study, the scattered H_2

and D_2 molecules could be probed with high-resolution Raman spectroscopy since their vibrational modes are IR inactive.

Appendix A: Obtaining HCl Number Density from Transient IR Signals

J-specific HCl populations are determined from fractional IR absorption $\Delta I/I_0$ by HCl in individual *J* states using Beer-Lambert's law as shown in Eq. A.1.

$$\frac{I_t}{I_0} = 1 - \frac{\Delta I}{I_0} = \exp(-\alpha_J P l) \qquad \text{(Eq. A.1)}$$

Here, I_t/I_0 is the fractional transmitted IR intensity, α_J is the *J*-specific absorption coefficient, *P* is the HCl bulk pressure and *l* is the path length, which is the 3-m collision cell used for experiments. The quantity α_J is obtained as given in Eq. A.2.

$$\alpha_J = \mathrm{S}_J f(0) N \qquad \text{(Eq. A.2)}$$

Here, S_J is the *J*-dependent absorption line strength for HCl, $f(0)$ is a factor that describes the *J*-specific HCl line profile at 300 K and *N* is the number density of HCl molecules at 300 K. The S_J values for HCl are obtained from the HITRAN database [73]. As shown in Eq. A.3, the line shape factor $f(0)$ is determined from the full width at half maximum (FWHM) of the thermal HCl line profile $\Delta\nu_{300\mathrm{K}}$.

$$f(0) = \frac{2}{\Delta\nu_{300\mathrm{K}}}\sqrt{\frac{\ln 2}{\pi}} \qquad \text{(Eq. A.3)}$$

The concentration or number density *n*/*V* of bulk HCl is obtained from the ideal gas law and is described by Eq. A.4.

$$[\mathrm{HCl}(300\mathrm{K})] = \frac{n}{V} = \frac{P}{\mathrm{RT}} = \frac{-\ln\left(\frac{I_t}{I_0}\right)}{S_J f(0) l}\left(\frac{\Delta\nu_{\mathrm{obs}}}{\Delta\nu_{300\mathrm{K}}}\right) \qquad \text{(Eq. A.4)}$$

Here, R is the ideal gas constant and T is 300 K. The quantity $\Delta\nu_{\mathrm{obs}}$ refers to the full width at half maximum of a *J*-specific line profile for HCl with $\Delta\nu_{\mathrm{obs}} = \Delta\nu_{\mathrm{app}}$ for an

appearance line profile and $\Delta\nu_{obs} = \Delta\nu_{dep}$ for a depletion line profile. The I_t/I_0 measurement that is used to determine [HCl (300 K)] is made before the firing of the UV pulse that excites the energy donor.

The number density of HCl population in a specific rotational state J and vibrational state v [HCl (v, J)] is determined by multiplying Eq. A.4 by the fractional population for that J state f_J and v state f_v.

$$[\mathrm{HCl}\ (v, J)] = \frac{n_J}{V} = \frac{P_J}{RT} = \frac{-\ln\left(\frac{I_t}{I_0}\right) f_J f_v}{S_J f(0) l}\left(\frac{\Delta\nu_{obs}}{\Delta\nu_{300K}}\right) \qquad \text{(Eq. A.5)}$$

To determine the number density of scattered [HCl (v, J)] population in nascent collisions with pyrazine-h_4 (E_{vib}) and pyrazine-d_4 (E_{vib}), I_t/I_0 is measured at t = 1 μs following UV excitation of the energy donor. The f_J term is described by the Boltzmann rotational distribution in Eq. A.6.

$$f_J = \frac{g_J \exp\left(\frac{E_{rot}}{k_B T_{rot}}\right)}{\sum_J g_J \exp\left(\frac{E_{rot}}{k_B T_{rot}}\right)} \qquad \text{(Eq. A.6)}$$

Here, g_J is the $2J + 1$ degeneracy of the J state of HCl, E_{rot} is the rotational energy, k_B is the Boltzmann constant and T_{rot} is the rotational temperature. The E_{rot} values used for HCl are taken from the HITRAN database [73]. The f_v term is described by the Boltzmann vibrational distribution shown in Eq. A.7.

$$f_v = \frac{g_v \exp\left(\frac{E_v}{k_B T_v}\right)}{Q_v} \qquad \text{(Eq. A.7)}$$

In Eq. A.7, g_v is the degeneracy of the vibrational state of HCl (which is equal to 1), E_v is the vibrational energy, T_v is vibrational temperature and Q_v is the vibrational partition function. The exact form of Q_v is given in Eq. A.8.

$$Q_v = \frac{1}{1 - \exp\left(-\frac{E_v}{k_B T}\right)} \qquad \text{(Eq. A.8)}$$

The concentration of the energy donor [donor (E_{vib})] is determined from UV absorption measurements as described by Eq. A.9

$$[\text{donor } (E_{vib})] = \frac{UV_{abs}}{E_{266}\pi r^2 l} \qquad \text{(Eq. A.9)}$$

where UV_{abs} is the amount of UV light absorbed by the energy donors pyrazine-h_4 and pyrazine-d_4, E_{266} is the photon energy at 266 nm, r is the radius of UV beam and l is the length of the collision cell.

Appendix B: Calculating Translational Temperature and Recoil Velocity of Scattered molecules

The lab-frame translational temperature T_{lab} for HCl in inelastic collisions with pyrazine-h_4 (E_{vib}) and pyrazine-d_4 (E_{vib}) is determined as described by Eq. B.1.

$$T_{lab} = \frac{m_{HCl} c^2}{8Rln2}\left(\frac{\Delta\nu_{obs}}{\nu_0}\right) \qquad \text{(Eq. B.1)}$$

Here, m_{HCl} is the mass of HCl, c is the speed of light, R is the gas constant, $\Delta\nu_{obs}$ is the full width at half maximum of a HCl line profile and ν_0 is the IR frequency at line center of a HCl transition. The $\Delta\nu_{obs}$ is $\Delta\nu_{app}$ for the appearance line profile, and $\Delta\nu_{dep}$ for the depletion line profile. The T_{lab} determined with $\Delta\nu_{app}$ is the lab-frame translational temperature for appearance of scattered HCl molecules T_{app}. The T_{lab} determined with $\Delta\nu_{dep}$ is the lab-frame translational temperature for depletion of initial HCl population T_{dep}.

The COM translational temperature T_{rel} of the collision partners is determined as given in Eq. B.2.

$$T_{rel} = T_{lab} + \frac{m_{HCl}}{m_{donor}}\left(T_{lab} - T\right) \qquad \text{(Eq. B.2)}$$

Here m_{donor} is the mass of the energy donor and T is ambient temperature (300 K). The m_{donor} is the mass of pyrazine-h_4 (for T_{rel} values obtained by using pyrazine-h_4 (E_{vib}) as the energy donor) or the mass of pyrazine-d_4 (for T_{rel} values obtained by using pyrazine-d_4 (E_{vib}) as the energy donor).

The average lab-frame recoil velocity $\langle \mathbf{v}_{lab} \rangle$ of scattered HCl in inelastic collisions with pyrazine-h_4 (E_{vib}) and pyrazine-d_4 (E_{vib}) is obtained as shown in Eq. B.3

$$\left\langle \mathbf{v}_{lab} \right\rangle = \left(\frac{3k_B T_{app}}{2m_{HCl}} \right)^{1/2} \qquad \text{(Eq. B.3)}$$

where k_B is the Boltzmann constant. The average COM recoil velocity $\langle \mathbf{v}_{rel} \rangle$ of the scattered collision partners is determined as described by Eq. B.4.

$$\left\langle \mathbf{v}_{rel} \right\rangle = \left(\frac{M}{m_{donor}} \right) \left(\left\langle \mathbf{v}_{lab} \right\rangle^2 - \left(\frac{3k_B T}{M} \right) \right)^{1/2} \qquad \text{(Eq. B.4)}$$

where M is the sum of the masses of HCl and the energy donor (pyrazine-h_4 (E_{vib}) or pyrazine-d_4 (E_{vib})). The average change in COM recoil velocity of scattered molecules $\langle \Delta \mathbf{v}_{rel} \rangle$ is obtained with Eq. B.5.

$$\left\langle \Delta \mathbf{v}_{rel} \right\rangle = \left\langle \mathbf{v}_{rel} \right\rangle - \left(\frac{3k_B T}{\mu} \right)^{1/2} \qquad \text{(Eq. B.5)}$$

$= \langle \mathbf{v}_{rel} \rangle - (3k_B T/\mu)^{1/2}$ with μ being the reduced mass of HCl and the energy donor (pyrazine-h_4 (E_{vib}) or pyrazine-d_4 (E_{vib})).

Appendix C: Calculating Lennard-Jones Rate Constant

The Lennard-Jones rate constant k_{LJ} for collisions of HCl and excited pyrazine-h_4 was calculated using Eq. C.1 [91].

$$k_{LJ} = \left(\frac{8k_B T}{\pi\mu}\right)^{1/2} \Omega^{(2,2)^*} \pi\sigma^2 \qquad \text{(Eq. C.1)}$$

Here, μ is the reduced mass of HCl and pyrazine-h_4, $\Omega^{(2,2)^*}$ is the collision integral, σ is the impact parameter. The collision integral $\Omega^{(2,2)^*}$ is dependent on the reduced temperature T* of the collision partners as shown in Eq. C.2.

$$\Omega^{(2,2)^*} = 1.16145(T^*)^{-0.14874} + 0.52487\exp(-0.7732T^*) + 2.16178\exp(-2.43787T^*) \qquad \text{(Eq. C.2)}$$

The reduced temperature T* is given by Eq. C.3.

$$T^* = \frac{k_B T}{\varepsilon} \qquad \text{(Eq. C.3)}$$

Here, k_B is the Boltzmann constant. The Lennard-Jones parameters σ and ε/k_B for HCl (bath) and excited pyrazine-h_4 (donor) collisions were determined as described in Eqs. C.4 and C.5 [91].

$$\sigma = \frac{1}{2}\left(\sigma_{bath} + \sigma_{donor}\right) \qquad \text{(Eq. C.4)}$$

$$\left(\varepsilon/k_B\right) = \left(\left(\varepsilon/k_B\right)_{bath}\left(\varepsilon/k_B\right)_{donor}\right)^{1/2} \qquad \text{(Eq. C.5)}$$

The following Lennard-Jones parameters were used to calculate σ and (ε/k_B) for HCl and pyrazine-h_4 (E_{vib}) collisions: $\sigma_{pyz} = 5.35 \times 10^{-10}$ m [59], $(\varepsilon/k_B)_{pyz} = 435.5$ K [59], $\sigma_{HCl} = 3.36 \times 10^{-10}$ m [93] and $(\varepsilon/k_B)_{HCl} = 218$ K [92].

Bibliography

1. G. W. Flynn, C. S. Parmenter, and A. M. Wodtke, "Vibrational energy transfer," J. Phys. Chem. **100**, 12817-12838 (1996).

2. R. E. Weston, Jr., and G. W. Flynn, "Relaxation of molecules with chemically significant amounts of vibrational energy: the dawn of the quantum state resolved era," Annu. Rev. Phys. Chem. **43**, 559-589 (1992).

3. D. C. Tardy, and B. S. Rabinovitch, "Intermolecular vibrational energy-transfer in thermal unimolecular systems," Chem. Rev. **77**, 369-408 (1977).

4. I. Oref, and D. C. Tardy, "Energy transfer in highly excited large polyatomic molecules," Chemical Reviews **90**, 1407-1445 (1990).

5. J. Du, L. W. Yuan, S. Hsieh, F. Lin, and A. S. Mullin, "Dynamics of weak and strong collisions: highly vibrationally excited pyrazine (E = 37900 cm^{-1}) with DCl," J. Phys. Chem. A **112**, 9396-9404 (2008).

6. D. K. Havey, J. Du, Q. Liu, and A. S. Mullin, "Full State-Resolved Energy Gain Profiles of CO2 (J = 2-80) from Collisions of Highly Vibrationally Excited Molecules. 1: Relaxation of Pyrazine (E = 37900 cm-1)," J. Phys. Chem. A **114**, 1569-1580 (2010).

7. J. T. Yardley, *Introduction to Molecular Energy Transfer* (Academic Press Inc., 1980).

8. J. C. Stephenson, R. E. Wood, and C. B. Moore, "Near-resonant energy transfer between infrared-active vibrations," J. Chem. Phys. **48**, 4790-& (1968).

9. J. A. Mack, K. Mikulecky, and A. M. Wodtke, "Resonant vibration-vibration energy transfer between highly vibrationally excited O_2(X (3)Sigma(g)(-),v=15-26) and CO2, N2O, N2, and O3," J. Chem. Phys. **105**, 4105-4116 (1996).

10. A. J. Sedlacek, R. E. Weston, and G. W. Flynn, "Interrogating the vibrational relaxation of highly excited polyatomics with time-resolved diode laser spectroscopy: C_6H_6, C_6D_6, and C_6F_6+CO_2," J. Chem. Phys. **94**, 6483-6490 (1991).

11. L. D. Zheng, J. Z. Chou, and G. W. Flynn, "Relaxation of molecules with chemically significant amounts of energy: vibrational, rotational, and translational energy recoil of an N_2O bath due to collisions with NO_2 (E = 63.5 kcal/mol)," J. Phys. Chem. **95**, 6759-6762 (1991).

12. L. A. Miller, C. D. Cook, and J. R. Barker, "Temperature effects in the collisional deactivation of highly vibrationally excited pyrazine by unexcited pyrazine," J. Chem. Phys. **105**, 3012-3018 (1996).

13. T. Lenzer, and K. Luther, "A quasiclassical trajectory study of energy transfer in benzene-benzene collisions," J. Chem. Phys. **104**, 3391-3394 (1996).

14. C. A. Michaels, A. S. Mullin, J. Park, J. Z. Chou, and G. W. Flynn, "The collisional deactivation of highly vibrationally excited pyrazine by a bath of carbon dioxide: excitation of the infrared inactive (10^00), (02^00), and (02^20) bath vibrational modes," J. Chem. Phys. **108**, 2744-2755 (1998).

15. C. A. Michaels, S. Mullin Amy, and G. W. Flynn, "Long- and short-range interactions in the temperature dependent collisional excitation of the antisymmetric stretching CO_2(00^01) level by highly vibrationally excited pyrazine," J. Chem. Phys. **102**, 6682-6695 (1995).

16. H. Hippler, J. Troe, and H. J. Wendelken, "Direct observation of collisional deactivation of highly excited toluene," Chem.Phys. Lett. **84**, 257-259 (1981).

17. H. Hippler, J. Troe, and H. J. Wendelken, "Collisional deactivation of vibrationally highly excited polyatomic molecules. II. Direct observations for excited toluene," J. Chem. Phys. **78**, 6709-6717 (1983).

18. M. J. Rossi, J. R. Pladziewicz, and J. R. Barker, "Energy-dependent energy transfer: deactivation of azulene (S_0, E_{vib}) by 17 collider gases," J. Chem. Phys. **78**, 6695-6708 (1983).

19. J. R. Barker, and R. E. Golden, "Temperature-dependent energy transfer: direct experiments using azulene," J. Phys. Chem. **88**, 1012-1017 (1984).

20. G. P. Smith, and J. R. Barker, "Energy transfer rates for vibrationally excited gas-phase azulene in the electronic ground state," Chem. Phys. Lett. **78**, 253-258 (1981).

21. U. Hold, T. Lenzer, K. Luther, K. Reihs, and A. C. Symonds, "Collisional energy transfer probabilities of highly excited molecules from kinetically controlled selective ionization (KCSI). I. The KCSI technique: experimental approach for the determination of P(E',E) in the quasicontinuous energy range," J. Chem. Phys. **112**, 4076-4089 (2000).

22. T. Lenzer, K. Luther, K. Reihs, and A. C. Symonds, "Collisional energy transfer probabilities of highly excited molecules from kinetically controlled selective ionization (KCSI). II. The collisional relaxation of toluene: P(E',E) and moments of energy transfer for energies up to 50 000 cm^{-1}," J. Chem. Phys. **112**, 4090-4110 (2000).

23. G. W. Flynn, and R. E. Weston, Jr., "Hot atoms revisited: laser photolysis and product detection," Annu. Rev. Phys. Chem. **37**, 551-585 (1986).

24. D. J. Nesbitt, "High-resolution infrared spectroscopy of weakly bound molecular complexes," Chem. Rev. **88**, 843-870 (1988).

25. P. F. Bernath, "High resolution infrared spectroscopy of transient molecules," Annu. Rev. Phys. Chem. **41**, 91-122 (1990).

26. P. B. Davies, "High resolution tunable infrared laser spectroscopy of transient molecules," Annu. Rep. Prog. Chem., Sect. C: Phys. Chem. **89**, 89-110 (1992).

27. M. S. Elioff, M. Fang, and A. S. Mullin, "Methylation effects in state resolved quenching of highly vibrationally excited azabenzenes (E_{vib}~38500 cm^{-1}). I. Collisions with water," J. Chem. Phys. **115**, 6990-7001 (2001).

28. E. M. Miller, L. Murat, N. Bennette, M. Hayes, and A. S. Mullin, "Relaxation dynamics of highly vibrationally excited picoline isomers (E_{vib} = 38300 cm^{-1}) with CO2: the role of state density in impulsive collisions," J. Phys. Chem. A **110**, 3266-3272 (2006).

29. D. K. Havey, Q. Liu, Z. Li, M. Elioff, M. Fang, J. Neudel, and A. S. Mullin, "Direct determination of collision rates beyond the Lennard-Jones model through state-resolved measurements of strong and weak collisions," J. Phys. Chem. A **111**, 2458-2460 (2007).

30. G. O. Echebiri, M. D. Smarte, W. W. Walters, and A. S. Mullin, "Performance of a high-resolution mid-IR optical-parametric-oscillator transient absorption spectrometer," Opt. Express (In press).

31. J. V. V. Kasper, C. R. Pollock, R. F. Curl, and F. K. Tittel, "Computer control of broadly tunable lasers: conversion of a color center laser into a high resolution laser spectrometer," Appl. Opt. **21**, 236-247 (1982).

32. H. K. Haugen, W. P. Hess, and S. R. Leone, "Application of semiconductor diode lasers to probe photodissociation dynamics," AIP Conf. Proc. **160**, 566-568 (1987).

33. A. Henderson, and R. Stafford, "Low threshold, singly-resonant CW OPO pumped by an all-fiber pump source," Opt. Express **14**, 767-772 (2006).

34. A. Henderson, R. Stafford, and P. Hoffman, "High-power CW OPOs span the spectrum," Laser Focus World **44**, 65-69 (2008).

35. L. E. Myers, and W. R. Bosenberg, "Periodically poled lithium niobate and quasi-phase-matched optical parametric oscillators," IEEE J. Quantum Electron. **33**, 1663-1672 (1997).

36. P. Gross, M. E. Klein, T. Walde, K. J. Boller, M. Auerbach, P. Wessels, and C. Fallnich, "Fiber-laser-pumped continuous-wave singly resonant optical parametric oscillator," Opt. Lett. **27**, 418-420 (2002).

37. A. Henderson, R. Stafford, and J. H. Miller, "Continuous wave optical parametric oscillators break new spectral ground," Spectroscopy **20**, 12-14, 16-18 (2005).

38. F. Adler, P. Maslowski, A. Foltynowicz, K. C. Cossel, T. C. Briles, I. Hartl, and J. Ye, "Mid-infrared Fourier transform spectroscopy with a broadband frequency comb," Opt. Express **18**, 21861-21872 (2010).

39. P. G. Mickelson, Y. N. M. de Escobar, P. Anzel, B. J. DeSalvo, S. B. Nagel, A. J. Traverso, M. Yan, and T. C. Killian, "Repumping and spectroscopy of laser-cooled Sr atoms using the $(5s5p)^3P_2$-$(5s4d)^3D_2$ transition," J. Phys. B: At. Mol. Opt. Phys. **42** (2009).

40. B. L. Yoder, R. Bisson, and R. D. Beck, "Steric effects in the chemisorption of vibrationally excited methane on Ni(100)," Science **329**, 553-556 (2010).

41. C. J. Higgins, and S. Chapman, "Collisional energy transfer between hot pyrazine and cold CO: a classical trajectory study," J. Phys. Chem. A **108**, 8009-8018 (2004).

42. J. H. Park, S. Y. Bae, and J. A. Lee, "Collisional quenching of vibrationally excited azabenzenes by unexcited azabenzenes," Chem. Phys. Lett. **303**, 505-512 (1999).

43. L. A. Miller, and J. R. Barker, "Collisional deactivation of highly vibrationally excited pyrazine," J. Chem. Phys. **105**, 1383-1391 (1996).

44. A. S. Mullin, C. A. Michaels, and G. W. Flynn, "Molecular supercollisions: evidence for large energy-transfer in the collisional relaxation of highly vibrationally excited pyrazine by CO_2," J. Chem. Phys. **102**, 6032-6045 (1995).

45. J. Du, L. Yuan, S. Hsieh, F. Lin, and A. S. Mullin, "Collisions of highly vibrationally excited pyrazine (E_{vib} = 37 900 cm^{-1}) with HOD: state-resolved probing of strong and weak collisions," J. Phys. Chem. A **112**, 9396-9404 (2008).

46. E. T. Sevy, M. A. Muyskens, S. M. Rubin, G. W. Flynn, and J. T. Muckerman, "Competition between photochemistry and energy transfer in ultraviolet-

excited diazabenzenes. I. Photofragmentation studies of pyrazine at 248 nm and 266 nm," J. Chem. Phys. **112**, 5829-5843 (2000).

47. I. Yamazaki, T. Murao, T. Yamanaka, and K. Yoshihara, "Intramolecular electronic relaxation and photoisomerization processes in the isolated azabenzene molecules pyridine, pyrazine, and pyrimidine," Faraday Discuss. Chem. Soc., 395-405 (1983).

48. D. C. Dayton, P. A. Block, and R. E. Miller, "Spectroscopic evidence for near-resonant intermolecular energy-transfer in the vibrational predissociation of C_2H2-HX AND C2H2-DX (X = Cl, Br, and I) complexes," J. Phys. Chem. **95**, 2881-2888 (1991).

49. J. D. Simmons, K. K. Innes, and G. M. Begun, "Infrared + raman spectra of pyrazine-H_4 + -D_4," J. Mol. Spectrosc. **14**, 190-197 (1964).

50. I. Yamazaki, T. Murao, T. Yamanaka, and K. Yoshihara, "Intramolecular electronic relaxation and photoisomerization processes in the isolated azabenzene molecules pyridine, pyrazine, and pyrimidine," Farad. Dis. Chem. Soc., 395-405 (1983).

51. L. Liu, X. B. Wang, X. Li, T. Liu, X. J. Xu, and Z. F. Jiang, "All fiber MOPA laser-pumped, continuous-wave, mid-infrared, singly-resonant optical parametric oscillator based on periodically poled MgO-Doped LiNbO(3)," Laser Physics **21**, 1704-1707 (2011).

52. A. Henderson, R. Stafford, and J. H. Miller, "Continuous wave optical parametric oscillators break new spectral ground," Spectroscopy (Duluth, MN, U. S.) **20**, 12-14, 16-18 (2005).

53. A. Henderson, and R. Stafford, "Low threshold, singly-resonant CW OPO pumped by an all-fiber pump source," Opt Express **14**, 767-772 (2006).

54. L. A. Pugh, and K. N. Rao, "Intensities from Infrared Spectra," in *Molecular Spectroscopy, Modern Research: Volume II*, K. N. Rao, ed. (Academic Press, New York, 1976), pp. 165-227.

55. P. Werle, and F. Slemr, "Signal-to-noise ratio analysis in laser absorption spectrometers using optical multipass cells," Appl. Opt. **30**, 430-434 (1991).

56. D. S. Bomse, A. C. Stanton, and J. A. Silver, "Frequency modulation and wavelength modulation spectroscopies: comparison of experimental methods using a lead-salt diode laser," Appl. Opt. **31**, 718-731 (1992).

57. D. J. Krajnovich, C. S. Parmenter, and D. L. Catlett, "State-to-state vibrational transfer in atom molecule collisions - beams vs bulbs," Chem. Rev. **87**, 237-288 (1987).

58. A. S. Mullin, G. C. Schatz, and Editors, *Highly Excited Molecules: Relaxation, Reaction, and Structure. (Proceedings of a Symposium at the 212th National Meeting of the American Chemical Society, 25-29 August 1996, in Orlando, Florida.) [In: ACS Symp. Ser., 1997; 678]* (1997).

59. T. J. Bevilacqua, and R. B. Weisman, "Collisional vibrational-relaxation of a triplet-state - energy-dependent energy-loss from T_1 pyrazine," J. Chem. Phys. **98**, 6316-6326 (1993).

60. C. A. Michaels, and G. W. Flynn, "Connecting quantum state resolved scattering data directly to chemical kinetics: energy transfer distribution functions for

the collisional relaxation of highly vibrationally excited molecules from state resolved probes of the bath," J. Chem. Phys. **106**, 3558-3566 (1997).

61. M. Fraelich, M. S. Elioff, and A. S. Mullin, "State-resolved studies of collisional quenching of highly vibrationally excited pyrazine by water: the case of the missing V -> RT supercollision channel," J. Phys. Chem. A **102**, 9761-9771 (1998).

62. D. R. McDowell, F. Wu, and R. B. Weisman, "Vibrational relaxation of T_1 pyrazine: results from the refined competitive radiationless decay method," J. Chem. Phys. **108**, 9404-9413 (1998).

63. U. Grigoleit, T. Lenzer, K. Luther, M. Mutzel, and A. Takahara, "Collisional energy transfer of highly vibrationally excited toluene and pyrazine: transition probabilities and relaxation pathways from KCSI experiments and trajectory calculations," Phys Chem. Chem. Phys. **3**, 2191-2202 (2001).

64. D. K. Havey, Q. Liu, Z. Li, M. Elioff, and A. S. Mullin, "Collisions of highly vibrationally excited pyrazine (E_{vib} = 37 900 cm^{-1}) with HOD: state-resolved probing of strong and weak collisions," J. Phys. Chem. A **111**, 13321-13329 (2007).

65. C. A. Michaels, Z. Lin, A. S. Mullin, H. C. Tapalian, and G. W. Flynn, "Translational and rotational excitation of the CO2(00(0)0) vibrationless state in the collisional quenching of highly vibrationally excited perfluorobenzene: evidence for impulsive collisions accompanied by large energy transfers," J. Chem. Phys. **106**, 7055-7071 (1997).

66. J. B. P. da Silva, M. R. S. Junior, M. N. Ramos, and S. E. Galembeck, "An ab initio study of the electronic and vibrational properties of pyrazine center dot center

dot center dot HX and XH center dot center dot center dot pyrazine center dot center dot center dot HX hydrogen-bonded complexes (X = F, NC, Cl, CN and CCH)," J. Mol. Struct. **744**, 217-220 (2005).

67. J. Wu, H. Yan, Y. Jin, G. Dai, and A. Zhong, "Characteristics and nature of the intermolecular interactions between pyridine and various hydrides: a theoretical study," J. Mol. Struc-Theochem **944**, 70-75 (2010).

68. C. M. Lovejoy, D. D. Nelson, and D. J. Nesbitt, "The infrared-spectrum of D_2HF," J. Chem. Phys. **89**, 7180-7188 (1988).

69. J. A. Syage, "Tunneling mechanism for excited-state proton transfer in phenol-ammonia clusters," J. Phys. Chem. **97**, 12523-12529 (1993).

70. E. J. Bohac, and R. E. Miller, "State-to-state vibrational predissociation of H_2-HF and D_2-HF - direct comparisons between theory and experiment," J. Chem. Phys. **98**, 2604-2613 (1993).

71. M. F. Hineman, G. A. Brucker, D. F. Kelley, and E. R. Bernstein, "Excited-state proton-transfer in 1-naphthol/ammonia clusters," J. Chem. Phys. **97**, 3341-3347 (1992).

72. B. M. Toselli, and J. R. Barker, "Isotope effects in the vibrational deactivation of large molecules," J. Chem. Phys. **97**, 1809-1817 (1992).

73. L. S. Rothman, D. Jacquemart, A. Barbe, D. C. Benner, M. Birk, L. R. Brown, M. R. Carleer, C. Chackerian, K. Chance, L. H. Coudert, V. Dana, V. M. Devi, J. M. Flaud, R. R. Gamache, A. Goldman, J. M. Hartmann, K. W. Jucks, A. G. Maki, J. Y. Mandin, S. T. Massie, J. Orphal, A. Perrin, C. P. Rinsland, M. A. H. Smith, J. Tennyson, R. N. Tolchenov, R. A. Toth, J. Vander Auwera, P. Varanasi, and G.

Wagner, "The HITRAN 2004 molecular spectroscopic database," J. Quant. Spectrosc. Ra. **96**, 139-204 (2005).

74. N. A. Besley, A. J. McCaffery, M. A. Osborne, and Z. Rawi, "Quantized momentum mechanics of inelastic and reactive collisions: the role of energy and angular momentum constraints," J. Phys. B: At. Mol. Opt. Phys. **31**, 4267-4282 (1998).

75. E. R. Waclawik, and W. D. Lawrance, "Angular momentum influences on vibrational relaxation pathways from 6^1 benzene," J. Chem. Phys. **109**, 5921-5930 (1998).

76. C. L. Perrin, and P. Karri, "Position-specific secondary deuterium isotope effects on basicity of pyridine," J. Am. Chem. Soc. **132**, 12145-12149 (2010).

77. D. Huyskens, and T. Zeegershuyskens, "Cooperative and isotope effects in complexes involving hydrogen chloride in solid argon," J. Mol. Struct. **321**, 11-19 (1994).

78. R. McConnell, W. Godwin, B. Stanley, and M. S. Green, "Acidity studies of deuterated acids and bases commonly used as buffers in NMR studies," J. Arkansas Acad. Sci. **51**, 135-140 (1997).

79. R. D. Sharma, and C. A. Brau, "Energy transfer in near-resonant molecular collisions due to long-range forces with application to transfer of vibrational energy from nu3 mode of CO_2 to N_2," J. Chem. Phys. **50**, 924-& (1969).

80. M. Drabbels, and A. M. Wodtke, "Rotational motion compensates the energy defect in near-resonant vibration-vibration energy transfer: a state-to-state study of NO(v)+N_2O," J. Chem. Phys. **109**, 355-358 (1998).

81. J. Z. Chou, and G. W. Flynn, "Energy dependence of the relaxation of highly excited NO_2 donors under single collision conditions: vibrational and rotational state dependence and translational recoil of CO_2 quencher molecules," J. Chem. Phys. **93**, 6099-6101 (1990).

82. C. J. Higgins, and S. Chapman, "Collisional energy transfer between hot pyrazine and cold CO: a classical trajectory study," Journal of Physical Chemistry A **108**, 8009-8018 (2004).

83. R. G. Gilbert, "Mechanism and models for collisional energy transfer in highly excited large polyatomic molecules," Aust. J. Chem. **48**, 1787-1817 (1995).

84. D. G. Mitchell, A. M. Johnson, J. A. Johnson, K. A. Judd, K. Kim, M. Mayhew, A. L. Powell, and E. T. Sevy, "Collisional relaxation of the three vibrationally excited difluorobenzene isomers by collisions with CO_2: Effect of donor vibrational mode," J. Phys. Chem. A **112**, 1157-1167 (2008).

85. H. C. Hsu, M. T. Tsai, Y. Dyakov, and C. K. Ni, "Energy transfer of highly vibrationally excited phenanthrene and diphenylacetylene," Phys. Chem. Chem. Phys. **13**, 8313-8321 (2011).

86. K. F. Lim, "Quasiclassical trajectory study of collisional energy transfer in toluene systems. I. Argon bath gas: energy dependence and isotope effects," Journal of Chemical Physics **100**, 7385-7399 (1994).

87. D. C. Clary, R. G. Gilbert, V. Bernshtein, and I. Oref, "Mechanisms for supercollisions," Faraday Discussions, 423-433 (1995).

88. V. Bernshtein, and I. Oref, "Collisional energy transfer between Ar and normal and vibrationally and rotationally frozen internally excited benzene-trajectory calculations," Journal of Chemical Physics **106**, 7080-7089 (1997).

89. V. Bernshtein, and I. Oref, "Gateway Modes for Collisional Energy Transfer between Benzene and Ar," Journal of Physical Chemistry A **105**, 10646-10650 (2001).

90. R. R. Stephens, and T. A. Cool, "Vibrational energy transfer and de-excitation in the HF, DF, HF-CO_2, and DF-CO_2 systems," J. Chem. Phys. **56**, 5863 (1972).

91. K. F. Lim, Quantum Chem. Program Exchange Bull. **14**, 3 (1994).

92. J. O. Hirschfelder, C. F. Curtiss, and R. B. Bird, *Molecular Theory of Gases and Liquids* (John Wiley and Sons, New York, 1964).

93. F. J. Zeleznik, and J. V. Dugan, Jr., "Rotational relaxation in polar gases. III. Molecular dynamics," Journal of Chemical Physics **54**, 4523-4527 (1971).